공학박사 학위논문

Development of 30Kc19α-based intracellular cargo delivery system and its therapeutic applications

30Kc19α 기반의 세포 내 카고 전달 시스템 개발 및 이의 치료적 응용

2023년 2월

서울대학교 대학원

공과대학 화학생물공학부

이 해 인

Development of 30Kc19α-based intracellular cargo delivery system and its therapeutic applications

지도 교수 박 태 현

이 논문을 공학박사 학위논문으로 제출함
2022년 12월

서울대학교 대학원
공과대학 화학생물공학부
이 해 인

이해인의 공학박사 학위논문을 인준함
2022년 12월

위 원 장 김 병 수 (인)

부위원장 박 태 현 (인)

위 원 황 석 연 (인)

위 원 김 정 아 (인)

위 원 박 희 호 (인)

Abstract

Development of 30Kc19α-based intracellular cargo delivery system and its therapeutic applications

Haein Lee

School of Chemical and Biological Engineering

The Graduate School

Seoul National University

Biological membranes are necessary for various functions of cells. However, their properties as selectively permeable barriers may hinder the delivery of therapeutic biomolecules into cells. Most biomolecules are cell-impermeable due to their polar, charged characteristics, or large size. When intracellular delivery of cell-impermeable biomolecules is available, new drugs can be developed for intracellular targets. Cell-penetrating peptides (CPPs) have been utilized as 'vehicles' for intracellular delivery of various therapeutic biomolecules, such as mRNA, DNA, and proteins. 30Kc19α is a cell-permeable protein originating from silkworm hemolymph, with cargo delivery properties.

Herein, 30Kc19α protein was utilized as a 'vehicle' for intracellular delivery of various cargo proteins such as enzyme, transcription factor, and growth factor.

Different from other CPPs, 30Kc19α has additional functions to cell-penetrating ability: solubility enhancer and protein stabilizer. With these characteristics, it was expected that the fusion of 30Kc19α and cargo proteins could improve the solubility and stability of cargo proteins. Fusion proteins were designed, and produced in *Escherichia coli* (*E. coli*). Then, their therapeutic efficacies were evaluated through various *in vitro* and *in vivo* experiments.

Firstly, arginine deiminase (ADI), a microbial-derived enzyme which catalyzes the conversion of L-arginine into L-citrulline, was selected as a cargo protein. ADI has been shown anti-tumor activity against melanoma which has an arginine-auxotrophic properties. However, when cancer cells are continuously exposed to extracellular ADI, ADI resistance develops because arginine is synthesized inside the cell, and thus intracellular delivery of ADI is required for conversion of arginine to citrulline. Moreover, recombinant ADI is mainly expressed as inclusion body forms in *E. coli* and unstable in human serum. 30Kc19α and recombinant ADI from *Mycoplasma hominis* were fused to solve these problems. Compared to ADI, ADI-LK-30Kc19α showed enhanced solubility, stability, and cell-penetration. The fusion protein demonstrated reduced ADI resistance in melanoma cells.

Secondly, runt-related transcription factor 2 (RUNX2), a master regulator of the osteogenic commitment of human mesenchymal stem cells (hMSCs), was selected as a cargo protein. However, recombinant RUNX2 was difficult to utilize due to low solubility and cell impermeability. 30Kc19α and recombinant RUNX2 were fused to solve these problems. Fusion of recombinant RUNX2 with 30Kc19α resulted in successful delivery of the protein into hMSCs, as well as enhanced soluble expression of the protein. Intracellular delivery of the 30Kc19α-RUNX2 fusion protein enhanced the osteogenic differentiation of hMSCs *in vitro*. 30Kc19α-

RUNX2 treatment resulted in increased alkaline phosphatase accumulation, and elevated calcium deposition. Implantation of hMSCs treated with 30Kc19α-RUNX2 showed osteogenesis *via* cell delivery into subcutaneous tissue and bone regeneration in cranial defect mice model.

Thirdly, basic fibroblast growth factor (bFGF), a growth factor which involves in tissue growth and regeneration, including wound healing, was selected as a cargo protein. 30Kc19α and recombinant bFGF were fused to enhance transdermal delivery of bFGF. 30Kc19α-bFGF retained the biological activity of bFGF as it facilitated the angiogenesis of endothelial cells. It was discovered that 30Kc19α could improve the transdermal delivery of a small molecular fluorophore through the skin of hairless mice. Importantly, it increased the accumulation of bFGF and further facilitated its translocation into the skin through follicular routes. Finally, when applied to a skin wound model *in vivo*, 30Kc19α-bFGF penetrated the dermis layer effectively, which promoted cell proliferation, tissue granulation, angiogenesis, and tissue remodeling.

Lastly, 30Kc19α-Linker-30Kc19α was developed by connecting two 30Kc19α with a flexible linker for efficient dimer formation and cell-penetration. Optimal flexible linker for dimerization was selected. Then, cargo delivery capacity of 30Kc19α and 30Kc19α-Linker-30Kc19α were compared. It was confirmed that 30Kc19α-Linker-30Kc19α delivered green fluorescent protein to HeLa cells with higher efficiency than 30Kc19α.

To summarize, 30Kc19α-based intracellular cargo protein delivery system was established. It enabled intracellular and transdermal delivery of various cargo proteins. Furthermore, the solubility and stability of the cargo proteins were improved by fusion with 30Kc19α. These factors worked together to result in higher

therapeutic efficacy of the cargo proteins both *in vitro* and *in vivo*. Therefore, this system would be applied to intracellular delivery of various therapeutic biomolecules facing challenges of cell-penetration.

Keywords: cell-penetrating protein, therapeutic biomolecules, fusion protein, intracellular delivery, solubility enhancer, protein solubilizer

Student Number: 2019-37199

Contents

List of Figures

List of Tables

List of Abbreviations

ADI: arginine deiminase
ADT: arginine deprivation therapy
ALP: alkaline phosphatase
ARS: Alizarin red S
α-SMA: α-smooth muscle actin
ASS1: argininosuccinate synthetase 1
bFGF: basic fibroblast growth factor
BMP-2: bone morphogenetic protein 2
BSA: bovine serum albumin
cDNA: complementary deoxyribonucleic acid
CLSM: confocal laser scanning microscopy
COL1: collagen type 1
CPP: cell-penetrating peptide
DAPI: 4',6-diamidino-2-phenylindole
DDW: deionized distilled water
DMEM: Dulbecco's modified eagle medium
ECM: extracellular matrix
EDC: 1-ethyl-3-(3-(dimethylamino) propyl) carbodimide
FACS: fluorescence-activated cell sorting
FBS: fetal bovine serum
FLARE: fluorescence-assisted resection and exploration
FPLC: fast protein liquid chromatography
GAPDH: glyceraldehyde 3-phosphate dehydrogenase
GFP: green fluorescent protein
H&E: hematoxylin and eosin
HDF: human dermal fibroblast
hMSC: human mesenchymal stem cell
HPF: high-power field
HRP: horseradish peroxidase
HUVEC: human umbilical vein endothelial cell
ICC: immunocytochemistry
IF: immunofluorescence
IHC: immunohistochemistry
IPTG: isopropyl β-D-1-thiogalactopyranoside
LB: Luria-Bertani
MFI: mean fluorescence intensity
MMP-2: matrix metalloproteinase-2

mRNA: messenger ribonucleic acid
MTC: Masson's trichrome
NHS: sulfo-hydroxysuccinimide
NIR: near-infrared
NLS: nuclear localization sequence
OCN: osteocalcin
OCT4: octamer-binding transcription factor 4
OM: osteogenic medium
OPN: osteopontin
PBS: phosphate buffered saline
PBST: Tween in phosphate buffered saline
PCR: polymerase chain reaction
PEG: polyethylene glycol
PFA: paraformaldehyde
PS: penicillin and streptomycin
PTD: peptide transduction domain
PTM: post-translational modification
qRT-PCR: quantitative reverse transcription polymerase chain reaction
RFI: relative fold induction
RUNX2: runt-related transcription factor 2
SBR: signal-to-background ratio
SC: stratum corneum
SDS-PAGE: sodium dodecyl sulfate polyacrylamide gel electrophoresis
SOX2: sex determining region Y-box 2
TAT: trans-activator of transcription
TE: trypsin-ethylenediaminetetraacetic acid
TME: tumor microenvironment

Chapter 1

Research background and objectives

Chapter 1. Research background and objectives

Recombinant protein is an engineered form of natural protein generated for a certain purpose [1]. Since recombinant human insulin was first produced in *Escherichia coli* (*E. coli*) in 1982, recombinant proteins have become a part of pharmaceutical products [2]. However, recombinant proteins have some limitations. Recombinant protein itself could be unstable or proteolytic degraded *in vivo*. Furthermore, it could not penetrate cells due to its characteristics, and this limits utilization of recombinant proteins in cytosolic application [3]. *E. coli* is one of the most used expression systems for the production of recombinant proteins [4]. It allows low-cost and rapid manufacturing of recombinant proteins. However, since post-translational modification does not occur in the *E. coli* system, it is suitable for protein expression of non-glycosylated proteins. Moreover, large sized proteins (> 30 kDa) tend to mis-fold and form inclusion bodies in *E. coli* expression system.

Since silkworm hemolymph exhibited anti-apoptotic effects in various cell systems, 30K protein family members, were isolated from silkworm hemolymph and studied intensively [5]. Among them, 30Kc19 received attention for its anti-apoptotic and protein stabilizing effects [6-8]. It was also discovered that 30Kc19 possessed cell- and tissue-penetrating properties by virtue of containing a type of cell-penetrating peptide (CPP) named Pep-c19 [9, 10]. Different from other CPPs, 30Kc19 has additional functions to cell-penetrating ability: protein stabilization, and soluble expression enhancement [8, 11]. For example, fusing 30Kc19 resulted in the soluble expression, and improved the stability of transcription factors [12, 13]. In the previous studies, it was confirmed that 30Kc19α, which is an α-helix domain of 30Kc19, retains important functions exhibited by 30Kc19 [14]. 30Kc19α enhanced

stability of cargo proteins and provided functional moieties for cell- and tissue-penetration when it was fused to green fluorescent protein (GFP). However, whether 30Kc19α can induce solubility in insoluble cargo protein products has not been examined.

In this study, it was investigated whether the fusion of 30Kc19α could enhance solubility of cargo proteins as well as cell-penetration and protein stability of them. Since most CPPs only provide cell-penetrating abilities to cargo proteins, additional protein solubility and stability enhancement properties of 30Kc19α could be put forward as an advantage of it. Then, it was confirmed that the improved characteristics of cargo proteins *via* fusion with 30Kc19α could induce therapeutic effects in various *in vitro* and *in vivo* models.

In summary, the objectives of this study are

1. Application of 30Kc19α on soluble expression, stability enhancement, and intracellular delivery of recombinant arginine deiminase (ADI) and solving ADI resistance in melanoma cells
2. Application of 30Kc19α on soluble expression and intracellular delivery of recombinant runt-related transcription factor 2 (RUNX2) and promoting osteogenic differentiation of human mesenchymal stem cells and bone regeneration
3. Application of 30Kc19α on cell-surface deposition and transdermal delivery of basic fibroblast growth factor (bFGF) and accelerating wound healing
4. Improving cell-penetrating efficiency of existing 30Kc19α through efficient dimer formation

If the cargo proteins could be delivered to cytosols or deeper tissues with

enhanced solubility and stability without cytotoxicity, this technology would be applicable in a variety of pharmaceutical fields.

Chapter 2

Literature review

Chapter 2. Literature review

2.1. Cell-penetrating peptide

2.1.1. Types of cell-penetrating peptides

Cell-penetrating peptides (CPPs) are short peptides that have been utilized as intracellular cargo delivery platform over the past 30 years [15]. As they could facilitate not only themselves but also cargos to translocate into cells, they have potentials to be applied as 'vehicles' in various pharmaceutical fields [16]. The first reported CPP was trans-activator of transcription (TAT; 48-60 aa of transcriptional protein of HIV-1) [17]. Since then, many CPPs with different charges, polarities and structures are used today *in vitro* and *in vivo* studies.

CPPs could be classified through a variety of criteria [18]. Firstly, CPPs could be divided into three groups according to their origins: peptide transduction domain (PTD), model peptide, and designed peptide [19]. CPPs such as Penetratin (43-58 aa of Antennapedia protein homeodomain) or Pep-c19 (45-57 aa of 30Kc19) derived from naturally occurring proteins are defined as PTDs [10, 20]. CPPs such as R9 (RRRRRRRRR) consisting of repeating amino acid sequences are defined as model peptides [21]. CPPs such as Pep-1 (KETWWETWWTEWSQPKKKRKV) produced by rational design (mutations or combinations between existing peptides) are defined as designed peptides [22].

Then, CPPs can be divided into three groups according to their physicochemical properties: cationic, amphipathic, and hydrophobic [23]. Cationic CPPs contain positively charged arginine and/or lysine amino acid residues (e.g., TAT peptide, penetratin, and polyarginine). Amphipathic CPPs contain positively and negatively charged amino acid residues (e.g., transportan). Hydrophobic CPPs contain non-

polar amino acid residues (e.g., Pep-7) [24]. Lastly, CPPs can be divided into two groups according to their conformations: linear and cyclic. Most of the CPPs are in a linear form, and several of them have been modified into cyclic forms to enhance the cell-penetrating ability. Some cyclic CPPs are synthesized or derived from natural proteins. Cyclic TAT (N_3-PEG_2-[K(rRrGrKkRr)E]) is one example of cyclic CPPs. It was found that cyclic TAT has a much higher efficiency of intracellular cargo protein delivery than its linear form [25].

2.1.2. Cell-penetrating mechanisms of CPPs

Although more than 30 years have passed since TAT was first discovered, the cell-penetrating mechanisms of CPP have not been fully elucidated. Although their uptakes in various cell types and cargo have been reported, the exact route of entry remains questionable. Direct translocation and endocytosis are the two main mechanisms by which CPPs enter cells. Their main difference is the energy dependence: direct translocation is energy-independent and endocytosis is energy-dependent [26].

Since direct translocation of CPPs is energy-independent mechanism, it could be tested in low temperature, energy depletion conditions and by the use of endocytosis inhibitors for the inhibition of micropinocytosis and receptor-mediated endocytosis (clathrin-mediated and caveolar-mediated) [27, 28]. There are several mechanisms suggested for direct translocation of CPPs: inverted micelle formation, pore formation, and carpet model [29]. All mechanisms involve the interaction of negatively charged cell membrane components with positively charged CPPs [30]. This results in transient or stable destabilization of the lipid bilayer membrane [31].

When CPPs are in low concentration or conjugated to cargos, they are prone to

enter cells by energy-dependent endocytosis [32]. Endocytosis is classified into phagocytosis and pinocytosis. Unlike pinocytosis which occurs in all cell types, phagocytosis only occurs in specific cell types including macrophages and monocytes [33]. In pinocytosis, there are macropinocytosis and receptor-mediated endocytosis (clathrin and caveolin proteins) [33]. It differs in that the former depends on lipid rafts and the latter on the receptor in endocytosis [34]. In micropinocytosis, actin-driven membrane protrusion occurs, which fuses with the cell membrane to form macropinosomes [35]. On the other hand, receptor-mediated endocytosis contains envelopment of ligand-coated particles [36].

2.2. *E. coli* expression system

2.2.1. Applications in therapeutic protein production

Humulin, a recombinant human insulin developed by Genentech in 1978, was the first approved drug produced in *E. coli* [37]. Nowadays, mammalian cell lines including Chinese hamster ovary (CHO) cells occupy a leading position in therapeutic protein expression systems, where glycosylation is required. However, *E. coli* has been adopted as an expression system for the large-scale production of therapeutic proteins, especially non-glycosylated proteins, in the biopharmaceutical industry. According to Biopharmaceutical benchmarks 2022, *E. coli* is dominant, as it is used in the production of 36 FDA-approved products [38]. Through many studies on *E. coli* expression systems, such as expression vectors, strains and culture methods, they have been developed to be suitable for industrial applications [39]. This could meet the needs of the current pharmaceutical industry.

Recently, there has been a movement towards the commercialization of antibody fragments, i.e. fragment antigen-binding (Fab), single-chain variable fragment (scFv) and single-domain antibody (sdAb) using *E. coli* expression system [40]. Unlike whole antibody, smaller antibody fragments have several advantages over antibodies such as better tissue-penetration and generally lower immunogenicity [41]. Many researches have produced antibody fragments in *E. coli*. and some of them have been approved from the FDA [40]. For example, CIMZIA® is a humanized Fab of anti-TNFα monoclonal antibody for the treatment of active psoriatic arthritis (FDA approval 2008) [42]. Beovu® is a humanized scFv for the treatment of neovascular age-related macular degeneration (FDA approval 2019) [41]. Cablivi® is a humanized sdAb for the treatment of acquired thrombotic

thrombocytopenia purpura (aTTP) (FDA approval 2019) [40].

2.2.2. Advantages and disadvantages of *E. coli* expression system

E. coli expression system is one of the most important industrial protein expression systems in that it offers various advantages such as well characterized strains, simple and cheap culture conditions, optimized culture procedures, fast growth and short production timescale and existing regulatory approvals (Table 2.1). However, when expressing mammalian-derived proteins in *E. coli* expression systems, there are several drawbacks compared to other expression systems. *E. coli* has a different codon usage with mammals. In addition, some large (> 30 kDa) proteins tend to be misfolded and expressed as inclusion bodies in *E. coli*. No post-translational modifications (PTMs), including glycosylation, occur in *E. coli*, and disulfide bond formation rarely occurs due to reducing environments [43].

Recent advances in biotechnology have improved the expression of mammalian proteins in *E. coli* [44]. Strains with tRNAs for the rare codons on plasmids (Rosetta2(DE3)pLysS and SixPack) and codon optimization tools have made it possible to overcome a codon bias [45, 46]. Soluble expression of large proteins could be achieved *via* utilization of weak promoters, molecular chaperons, fusion with solubility enhancers [47-49]. PTMs, such as glycosylation occur when enzymatic machinery required for glycosylation such as human polypeptide N-acetylgalactosaminyl transferase, β1,3-galactosyl transferase and UDP-Glc (NAc)-4-epimerase is co-expressed with heterologous proteins [43]. Furthermore, there has also been a report of disulfide-containing protein expression in SHuffle or Origami strains which provides an oxidizing cytoplasmic environment to facilitate the

formation of disulfide bonds or in conventional *E. coli* strains which express sulfhydryl oxidase and human protein DNA interactome [50].

Table 2.1. Advantages and disadvantages of *E. coli* expression system

	Advantages	Disadvantages
***E. coli* expression system**	- Suitable for genetic engineering - Well characterized strains - Simple and cheap culture conditions - Optimized culture procedures - Fast growth and short production timescale - Existing regulatory approval	- Different codon usage - Large (> 30kDa) protein mis-folding and inclusion body formation - No post-translational modifications including glycosylation - Challenges in disulfide bond formation due to reducing environment

Chapter 3

Experimental procedures

Chapter 3. Experimental procedures

3.1. Plasmid construction

30Kc19α gene, 1st-264th nucleotides of *30Kc19* gene, was obtained from *30Kc19* gene (GenBank accession number: X54736) [14]. Some template genes (*bFGF*, *RUNX2*) were obtained from Addgene. Others were synthesized, codon optimized for expression in *E. coli* (*arcA*; GenBank accession number: OP191658) (Bionics, Korea). *30Kc19α* and genes for cargo proteins were amplified by polymerase chain reaction (PCR) using primers containing specific restriction enzyme cut sites. Then, the PCR products were inserted into pET-23a(+) expression vector (Novagen, USA) for protein expression in *E. coli*. The plasmid contains a His-tag at the C-terminus and a T7-tag at the N-terminus, respectively, for recombinant protein purification and analysis.

3.2. Site-directed mutagenesis

Cysteine to alanine point mutation of 57th cysteine in *30Kc19α* gene was performed using site-directed mutagenesis. pET-23a/*30Kc19α* was amplified using primers with mismatching nucleotides. Phusion™ high-fidelity DNA polymerase (Thermo Fisher Scientific, USA) was used for proof-reading. After PCR reaction, PCR products were cleaned up. Then, purified PCR products were digested with DpnI (Enzynomics, Korea) to remove methylated DNA templates. T4 polynucleotide kinase (Enzynomics) was added to phosphorylate the 5' end of the PCR products. The mixture was incubated at 37°C for 30 minutes. T4 DNA ligase (Enzynomics) was added sequentially to the mixture and the ligation reaction was performed at room temperature for 1 hour. For transformation, 5 μl of the ligation reaction mixture was added to DH5α competent cell.

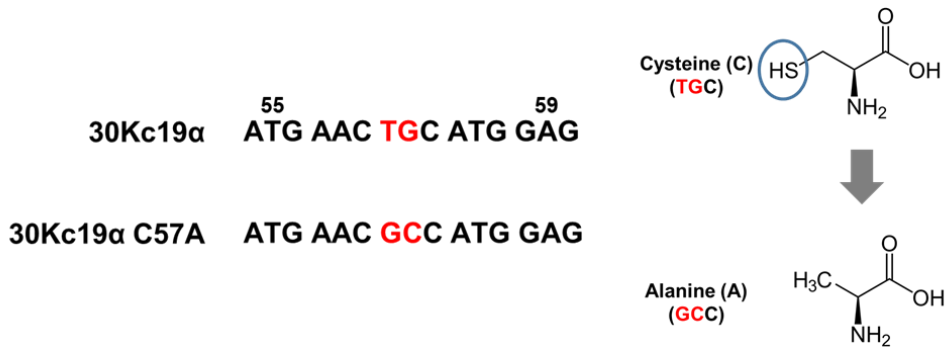

Figure 3.1. Cysteine to alanine point mutation of 57th cysteine in *30Kc19α* gene.

3.3. Recombinant protein production in *E. coli* and analysis

3.3.1. Recombinant protein expression in *E. coli*

Plasmids were transformed into BL21 competent cells (Novagen) for recombinant protein production. The transformed *E. coli* was cultured in Luria-Bertani (LB) medium (LPS solution, Korea) with 100 μg/ml ampicillin (Sigma-Aldrich, USA) at 37°C overnight with shaking. The LB medium was transferred to 1 L LB medium and cultured at 37°C. When OD_{600} reached between 0.4 and 0.6, isopropyl β-D-thiogalactopyranoside (IPTG; Calbiochem, USA) was added to induce protein expression, and *E. coli* was further incubated. IPTG concentration, induction temperature, and incubation time after induction depended on the recombinant proteins. The cells were harvested by centrifugation at 7,000 rpm for 10 minutes at 4°C.

3.3.2. Recombinant protein purification by FPLC

Recombinant proteins were purified using fast protein liquid chromatography (FPLC; Cytiva, Sweden). After discarding the supernatant, the pellets were resuspended in His-binding buffer (20 mM imidazole (Sigma-Aldrich), 20 mM Tris (LPS solution), 500 mM NaCl (Supelco, USA), pH 8.0). Resuspended cells were lysed by sonication. The cell lysates were centrifuged to separate the supernatant and pellet. The filtered supernatants were loaded into HisTrap HP 5 ml column (Cytiva) pre-filled with His-binding buffer. To washout unbound or weakly-bound proteins, His-washing buffer (50 mM imidazole, 20 mM Tris-HCl, and 0.5 M NaCl, pH 8.0) was flowed through the column. The remained proteins were eluted with His-elution buffer (350 mM imidazole, 20 mM Tris-HCl, 0.5 M NaCl, pH 8.0). Finally, the elution buffer was changed to 20 mM Tris-HCl buffer (pH 8.0) or 1x phosphate

buffered saline (PBS; WelGENE Inc., Korea) using a desalting column (Cytiva) for further use.

3.3.3. Coomassie blue staining and western blot analysis

Protein samples were analyzed by sodium dodecyl sulfate-polyacrylamide gel electrophoresis (SDS-PAGE). The proteins were mixed with 2x Laemmli sample buffer (Bio-Rad, USA) and loaded to 10-15% acrylamide gels depending on the size of the protein. For Coomassie brilliant blue staining, gels were stained with Coomassie brilliant blue R-250 (Sigma-Aldrich) for 1 hour. The gels were then destained sequentially with strong destaining solution (40% (v/v) methanol in water with 7% (v/v) acetic acid) for 1 hour and weak destaining solution (5% (v/v) methanol in water with 7% (v/v) acetic acid) overnight.

For western blot analysis, the proteins on the gels were transferred onto a nitrocellulose membrane (Cytiva). After blocking with 5% skim milk in 1x PBS, 0.1% Tween® 20 detergent (0.1% PBST) for 1 hour, the membrane was incubated with primary antibody diluted in 1% skim milk in 0.1% PBST, and secondary antibody diluted in 5% skim milk in 0.1% PBST sequentially. As T7 tag and His tag are in the N-terminus and C-terminus of the recombinant protein respectively, rabbit anti-T7 tag antibody (ab9115; Abcam, UK) and mouse anti-His tag antibody (sc-53073; Santa Cruz Biotechnology, Inc., USA) were used as primary antibodies for recombinant proteins. Goat anti-rabbit IgG-horseradish peroxidase (HRP) antibody or goat anti-mouse IgG-HRP antibody (AbFrontier, Korea) were used as secondary antibodies. To visualize the bands, TOPview™ ECL pico plus western substrate (Enzynomics) was used. The images were obtained by gel documentation system (G:BOX chemi XRQ; Genesys, USA).

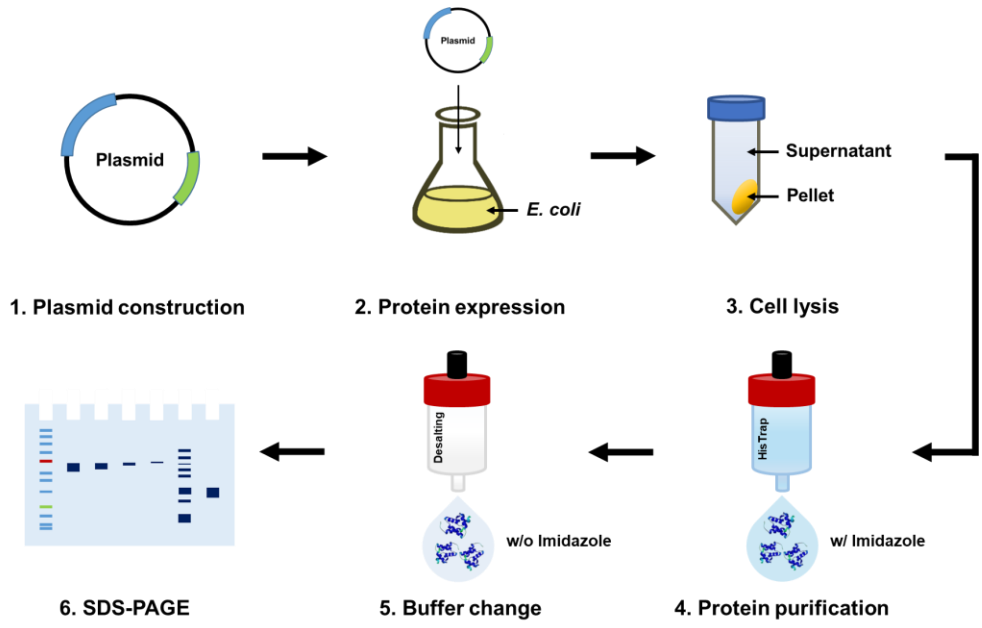

Figure 3.2. Main steps of recombinant protein production in *E. coli* and analysis.

3.4. Mammalian cell culture

3.4.1. Mammalian cell culture except hMSC

Various mammalian cells were cultured according to standard protocols. Most of cells were cultured in Dulbecco's modified Eagle's medium (DMEM; Biowest, France) containing 10% fetal bovine serum (FBS; Biowest) and 1% penicillin streptomycin (PS, Sigma-Aldrich). Especially, human umbilical vein endothelial cells (HUVECs; Lonza, USA) were cultured with endothelial cell basal medium-2 (Lonza).

3.4.2. hMSC culture and osteogenic differentiation

Bone marrow-derived hMSCs (Lonza) were cultured in 24-well plate (Eppendorf, Germany) with MSCGM (Lonza), until the cells reached 80% confluency. Then, cells were transferred to osteogenic medium. Two kinds of osteogenic medium were used: firstly, conventional osteogenic medium (briefly OM) (DMEM supplemented with 10% FBS, 1% PS, 50 μM ascorbic acid (Sigma-Aldrich), and 10 mM β-glycerophosphate (Sigma-Aldrich) and 100 nM dexamethasone (Sigma-Aldrich)), and secondly, osteogenic medium without dexamethasone (briefly OM without dexamethasone) (DMEM supplemented with 10% FBS, 1% PS, 50 μM ascorbic acid, 10 mM β-glycerophosphate). When OM was used, cells were treated once with equimolar proteins on day 0. When OM without dexamethasone was used, cells were treated twice with equimolar proteins on day 0 and day 2. The medium was replaced by fresh medium every 2 days.

3.5. Cell-penetration analysis

3.5.1. Confocal imaging system

5.0×10^3 cells were seeded into the confocal region of confocal dish (SPL Life Science, Korea). Next day, cells were treated with recombinant proteins. After recombinant protein treatment, immunocytochemistry (ICC) was conducted. The proteins were labeled with Alexa Fluor® 488 or Alexa Fluor® 594 (Invitrogen, USA), and the nucleus was counterstained with DAPI (Invitrogen). Confocal images were obtained by a LSM710 confocal laser scanning microscopy (CLSM) (Carl Zeiss, Germany).

3.5.2. HiBiT lytic detection system

To quantify cell-penetrated proteins, HiBiT lytic detection system was performed according to the manufacturer's instructions. HiBiT tag was inserted in N-terminus of recombinant proteins and HiBiT-tagged recombinant proteins were produced in *E. coli* as the same way. 5.0×10^3 cells were seeded in each well of 96-well microplates (Eppendorf). When cells are approximately 70% confluent, cells were treated with 100 nM or 1 μM of recombinant proteins. After 24-hour treatment, cells were washed with Dulbecco's phosphate buffered saline (DPBS; WelGENE Inc.) to eliminate membrane-bound proteins and treated with Nano-Glo® HiBiT detection reagent (Promega, USA) containing LgBiT. The samples were mixed by placing the plate in shaking incubator. After 10 minutes, luminescence was measured in a microplate reader (Tecan, Switzerland). By titrating purified HiBiT-tagged proteins, standard curve was obtained, and using this standard curve, cell-penetrated proteins were quantified from luminescence.

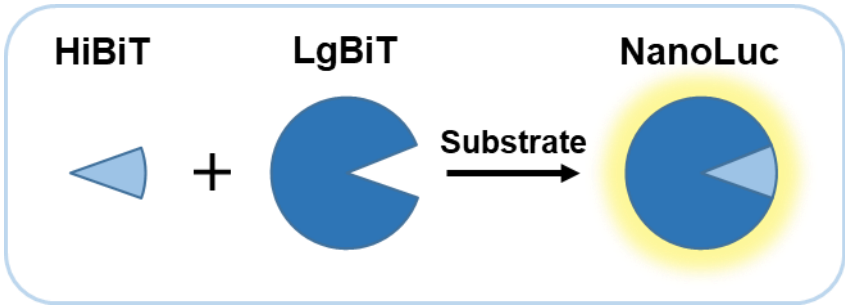

Figure 3.3. Description of NanoLuc binary technology. When two subunits of NanoLuc (HiBiT and LgBiT) meet, they bind together and form luminescent enzyme (NanoLuc).

3.6. Protein stability analysis

To evaluate *in vitro* serum stability of the recombinant proteins, 40 μl of 4 μM of recombinant proteins were added into 360 μl of diluted FBS. The mixture was incubated at 37℃ for 12, 24, 48, 72, 96, and 120 hours. To conduct *in vitro* proteolysis assay, 4 μM of recombinant proteins were exposed to 1 μg/ml of trypsin (Sigma-Aldrich) or 100 ng/ml of proteinase K (Bioneer, Korea) for up to 60 minutes. Concentration of trypsin and proteinase K were determined to be the concentrations at which the activity of ADI began to decrease. Proteolysis was stopped by adding 1 mM PMSF [51]. Before experiments, proteolysis prediction in recombinant ADI was analyzed by ExPASy-PeptideCutter tool [52].

3.7. Cytotoxicity analysis

3.7.1. CELLOMAX^{TM} cell viability assay

5.0×10^3 cells were seeded in each well of 96-well microplates containing 0.1 ml of DMEM medium supplemented with 2 or 10% FBS and 1% PS. The cells were preincubated at 37℃ with 5% CO_2 for 24 hours. Then, the cells were treated with various concentrations of proteins and further incubated for up to 72 hours. 10 μl of CELLOMAX^{TM} cell viability assay kit solution (Precaregene, Korea) was added into each well and the plates were incubated at 37℃ for 2 hours. The absorbance was measured at 450 nm in a microplate reader (Tecan).

3.7.2. Live/Dead viability assay

Staining was conducted for protein-treated cells or cells seeded on gelatin cryogels following the manufacturer's instruction. Cells were stained with LIVE/DEAD viability kit (Invitrogen) containing calcein-AM and ethidium

homodimer-1. The stained samples were observed *via* fluorescence microscopy (Olympus, Japan) or CLSM. The percentage of live cells were calculated based on microscopic images.

3.8. *In vitro* analysis

3.8.1. Real-time qRT-PCR

To quantify the mRNA levels of target genes in each group, and compare the obtained data among the three groups, real-time quantitative reverse transcription polymerase chain reaction (qRT-PCR) assay was conducted. Total RNA was isolated using TRIzol® (Invitrogen). Then, complementary deoxyribonucleic acids (cDNAs) were synthesized from the isolated RNAs by SuperiorScript III cDNA synthesis kit (Enzynomics). *GAPDH* was used as reference gene, and following target genes were analyzed: *Argininosuccinate synthetase 1 (ASS1), collagen type 1 (COL1), osteocalcin (OCN) and osteopontin (OPN)* [53, 54]. RNase free water, SYBR green master mix (Enzynomics), forward and reverse primer of each gene (Bionics), and cDNA were mixed; then, real-time qRT-PCR was carried out by StepOne™ real-time PCR systems (Applied Biosystems, USA). Gene expression level related to *GAPDH* was calculated by $\Delta\Delta C_T$ method.

Table 3.1. Primer sequences used in real-time qRT-PCR.

Gene	Primer sequence (5'→3')	
ASS1	**Forward**	AGGCACCATCCTTTACCATG
	Reverse	CTGCACTTTCCCTTCCACTC
COL1	**Forward**	CAAGAGCCTGAGCCAGCAGA
	Reverse	TTCTGGGCCACACTGGGCT
GAPDH	**Forward**	TTCACCACCATGGAGAAGGC
	Reverse	TCTTCTGGGTGGCAGTGATG
OCN	**Forward**	TATTGGCCCTGGCCGCACTT
	Reverse	CTCACACACCTCCCTCCTG
OPN	**Forward**	GCATCACCTGTGCCATACCAG
	Reverse	TCCTGGCTGTCCACATGGTC

3.8.2. Immunocytochemical analysis

To observe the expression of target protein in each group, and compare the extent of protein expression among the three groups, ICC was conducted. OPN, osteoblast-related protein expressed in osteogenic differentiation, was selected as a protein of interest. Three groups of hMSCs differentiated in OM for (14 and 21) days were fixed and permeabilized. After blocking with bovine serum albumin (BSA), anti-OPN antibody (ab8448; Abcam) was used as primary antibody, and Alexa Fluor® 488 was used as secondary antibody. The nuclei were counterstained with DAPI. Fluorescence microscopy (Olympus) was used to observe OPN labeled with fluorescent dye. Quantification of OPN specific fluorescence intensity was performed using ImageJ software. The values are expressed as mean fluorescence intensity (MFI).

3.8.3. ALP staining and ARS staining

Alkaline phosphatase (ALP) staining and Alizarin Red S (ARS) staining were conducted on hMSCs differentiated in OM or OM without dexamethasone, to visualize the ALP activity and mineral deposits. The medium was aspirated from the wells, and then each well was washed with PBS. In the case of ALP staining, fixative solution, a mixture of acetone (Sigma-Aldrich) and citrate solution (Sigma-Aldrich) (3:2, v/v), was used for fixation. After fixation, ALP staining solution (0.1% naphthol AS-MX phosphate (Sigma-Aldrich) and 0.1% fast blue BB salt (Sigma-Aldrich)) was added. In the case of ARS staining, 4% paraformaldehyde (PFA; Biosaesang, Korea) in PBS was used for fixation. After fixation, 2% w/v ARS (Sigma-Aldrich) in deionized distilled water (DDW) was added onto each well. Then, wells were washed with DDW. Finally, camera images and optical microscopy (Olympus)

images of staining results were obtained.

3.8.4. *In vitro* angiogenesis assay

The matrigel solution (Geltrex® Matrix Product, Thermo Fisher Scientific) was put into a 24-well plate and gelated at 37°C. HUVECs were seeded onto the matrigel at 5 x 10^4 cells per well and maintained with a serum-free medium that did not contain both bFGF and vascular endothelial growth factor of EGM™-2 kit. The cells were treated with 4 μM of recombinant proteins, respectively. After 12 hours, the number of tube formation and branching points were measured based on images using ImageJ (ImageJ Software). Detroit 551 and SK-MEL-2 were obtained from Korean Cell Line Bank (KCLB10110, KCLB 30068).

3.9. Gel preparation and characterization

3.9.1. Gelatin cryogel preparation and characterization

For fabrication of gelatin cryogel, 1% w/v type A gelatin (porcine skin, Sigma-Aldrich) was dissolved in DDW at 60 ℃. The gelatin solution was put in 4 ℃ fridge, until use. Cross-linking agents were prepared: 1-ethyl-3-(3-(dimethylamino) propyl) carbodimide (EDC) (Thermo Fisher Scientific) and sulfo-hydroxysuccinimide (NHS) (Thermo Fisher Scientific) were dissolved in DDW at 50 nM and 25 mM concentration, respectively. The gelatin solution and cross-linking reagent solutions were mixed and aliquoted into pre-chilled mold. Right after aliquoting, samples were put into -20 ℃ for gelation and ice crystal formation overnight. Ice crystal-formed samples were lyophilized next morning. During lyophilization, macropores formed where ice crystals were once located. Gels were re-hydrated in DDW and put in 35mm-dish under UV for two days for sterilization and to remove remaining EDC

and NHS. DDW was changed every 24 hours. Gels were cut into smaller sizes *via* 3.5mm-diameter size biopsy punch (Miltex, USA), to fit into the cranial defect site. The same sized gels were used for mouse subcutaneous tissue delivery as well.

Gelatin cryogel swelling ratio measurement was measured. The weights of gels in dried state after lyophilizing and in swollen state with DI water were measured. Then, Young's modulus of the swollen cryogels was measured *via* compression test. Swollen cryogels were compressed under 1 mm min^{-1} of pressure. The slope of linear region in the stress–strain curve was used to calculate the Young's modulus. The swelling ratio was calculated by the equation below:

$$q = \frac{w_2 - w_1}{w_1}$$

where, q = swelling ratio, w_1 = swollen weight, and w_2 = dried weight.

3.9.2. Protein-containing carbomer gel preparation

Carbomer (Carbopol 940, Polygel CA, Happycall Co., Ltd., Korea) was used to apply samples into wounds with increased retention. Carbomer was sterilized *via* UV irradiation overnight and dissolved in deionized water until the solution became homogenous. Triethanolamine was added to adjust pH and make the gel form. Protein stocks were mixed with the carbomer gel, and a final concentration of carbomer and proteins were 0.5% (w/v) and 5.47 μM, respectively.

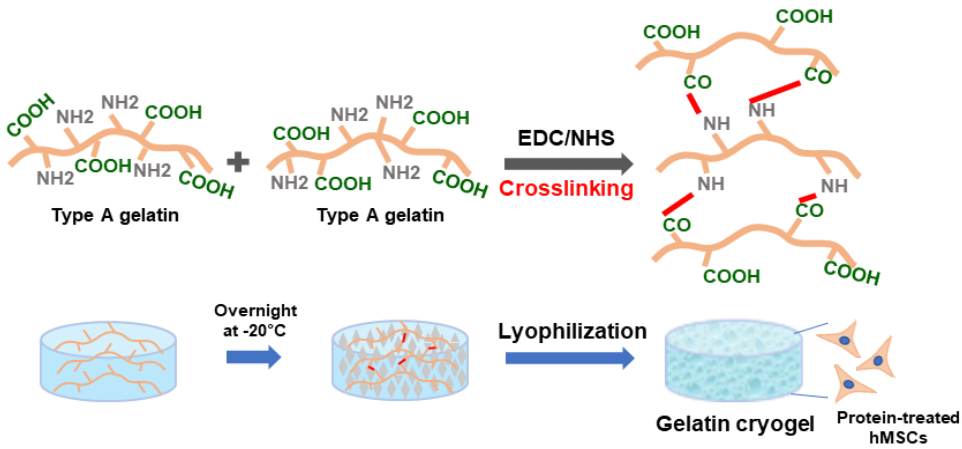

Figure 3.4. Simple schematics showing gelatin cryogel fabrication.

3.10. Animal experiments

3.10.1. Mouse subcutaneous model

All experiments were performed in accordance with the Seoul National University Guide for the Care and Use of Laboratory Animals (SNU-170728-1-5). Eight-week female Balb/c-nude mice were used for all animal model experiments, and were cared for in climate-controlled rooms at 22℃ with 50% humidity and 12 h:12 h light-dark cycles. Mice were supplied by Orient Bio Korea and were eight-week-old at the time of surgery. Mice were anesthetized *via* Zoletil 50 (Virbac, France) and Rompun® Inj (Bayer, Germany). After making a 1 cm longitudinal cut on the neck/back of mice, cell-seeded scaffolds were placed under subcutaneous tissue. Samples were collected 4 weeks after surgery.

3.10.2. Mouse cranial defect model

All experiments were performed in accordance with the Seoul National University Guide for the Care and Use of Laboratory Animals (SNU-170728-1-5). For cranial defect models, a longitudinal incision was made on the head of mice, and defects were made in the center of the sagittal crest with a 4 mm diameter dental drill. Cell-seeded gelatin cryogels, as well as aceullar cryogels, were placed on the defect area, and the incision was sutured with 6-0 Vicryl (Ethicon, Inc., USA). Crania samples were collected 8 weeks after surgery.

3.10.3. Mouse skin-penetration and wound healing model

All *in vivo* experimental procedures using 30Kc19α-bFGF were approved by the IACUC of the Seoul National University (SNU-190916-2-1), and the study was performed with eight-week male Balb/c-nude mice (OrientBio Co., Korea).

For the skin-penetration test of 30Kc19α, sterilized carbomer was mixed with

5 μM of ZW800-1C or 30Kc19α-ZW800-1C conjugates in DI water, and then triethanolamine was added to form gels. Press-to-Seal silicone isolators (S1810, 9-mm diameter, Sigma-Aldrich) were used to apply carbomer mixtures on the back of eight-week nude mice (NCRNU). After 4 hours, carbomer mixtures were washed off three times with a wet towel. Animals were then imaged using the fluorescence-assisted resection and exploration (FLARE) imaging system with 3.6 mW/cm^2 of 760 nm excitation light and white light (400-650 nm) at 5,500 lux. Through ImageJ software, the fluorescent signals were quantified by the signal-to-background ratio (SBR) and normalized to ZW800-1C values.

For the transdermal delivery and wound healing test of 30Kc19α-bFGF, the protein gels were applied to the dorsal regions of hairless mice and washed off after 4 hours. For the skin wound penetration test, full-thickness wounds were formed on dorsal skin by biopsy punch with a diameter of 6 mm, followed by applying the protein gels to the wounds. After 4 hours, the animals were sacrificed by excess CO_2 exposure, and the skin tissues were processed to perform immunofluorescence (IF). Mice were anesthetized with isoflurane during the surgery. Full-thickness wounds were formed on dorsal skin by biopsy punch with a diameter of 6 mm. Press-to-Seal silicone isolators were used for preventing contractile effects and as reference for measuring the wound size. 30 μl of carbomer gel without proteins (control) or 30 μl of protein gels was applied to the wounds every 2-3 days. All wounds were covered by Tegaderm™ film dressing (3M, USA). Wound size was measured using ImageJ software and quantified as the percentage of remaining size compared to the initial defect area.

3.10.4. *Ex vivo* porcine skin-penetration test

Micropig® Franz Cell Membranes with 400 μm thickness, including epidermal and dermal layers, were purchased from Apures Co., Ltd., (Korea). Using protein gels (Carbopol with both bFGF and 30Kc19α-bFGF), both transdermal delivery and wound penetration tests were performed. For transdermal delivery, 100 μL of the protein gels were applied on the 2 cm x 2 cm skin. The gels were covered with 1 cm x 1 cm gauze, and a 1.0 g mass was placed on the gauze. After 4 hours, gel residues were washed off with PBS, and the tissues were fixed with 4% PFA. For wound penetration, the skin tissue was punctured with a 3.5 mm diameter biopsy punch and then placed on a polyimide substrate. Protein gels were applied to the pores of the skin, and then the tissues were fixed with 4% PFA after 4 hours. The tissues for each experiment were paraffin-embedded and sliced into 5 μm thickness, followed by immunohistochemistry (IHC) staining with anti-T7 tag antibody.

3.11. *In vivo* analysis

3.11.1. Histological staining

Mice were sacrificed at each time point by excess CO_2 exposure, and crania or skin tissues were excised, followed by fixation in 4% PFA. The tissues were embedded in paraffin and sectioned. Deparaffinization, removal of xylene, and rehydration were performed on the sectioned tissues prior to any analysis [55]. Histological staining was made *via* Hematoxylin & Eosin (H&E), and Masson's trichrome (MTC) staining on paraffin-embedded samples. For IF and IHC staining, primary antibodies to Ki67 (ab15580, Abcam), OPN (ab8448, Abcam) and α-smooth muscle actin (α-SMA; ab5694, Abcam) were used, respectively.

3.11.2. Histological quantification

The proliferative cells on day 6 during the wound healing stage were quantified from the fluorescent intensity of both Ki67 and DAPI staining images. The percentage values were calculated by measuring the percentage of Ki67 fluorescence normalized to DAPI using ImageJ software.

Panniculus gap and granulation tissue thickness were manually measured from H&E images MTC images using ImageJ software. The margin of the panniculus gap was assigned as a length between the point where the adipocyte coverage area was terminated. Granulation tissue area was also calculated using ImageJ software.

Extracellular matrix (ECM) fiber alignment was quantified using the OrientationJ plugin available on ImageJ software, as described in previous research. Coherence values (dimensionless) were obtained from the region of interest in MTC images of each sample.

In vivo vessel formation was quantified based on the high-power field (HPF) 40X magnified images of α-SMA on day 14. Vessel numbers were counted on at least 15 images and averaged.

3.12. Statistical analysis

Statistical analysis was conducted by Student's t-test to estimate statistical significance. For all experiments, each group had n = 3-8, and all data are presented as mean ± standard error of the mean. p values less than 0.05 were recognized as statistically significant: $*p < 0.05$, $**p < 0.01$, $***p < 0.005$.

Chapter 4

Intracellular delivery of recombinant ADI facilitated by 30Kc19α for overcoming ADI resistance in melanoma treatment

Chapter 4. Intracellular delivery of recombinant ADI facilitated by 30Kc19α for overcoming ADI resistance in melanoma treatment

4.1. Introduction

Arginine is a non-essential amino acid for humans as it can be produced from citrulline *via* urea cycle through the expression of argininosuccinate synthetase 1 (ASS1) and argininosuccinate lyase in normal cells [56]. However, arginine-auxotrophic tumors, such as melanoma, hepatocellular carcinoma, and mesothelioma lose the ability to synthesize arginine due to silencing of ASS1 [57-59]. Thus, these tumors depend only on external supply of arginine for cell growth and survival. Arginine deprivation therapy (ADT) is emerging as a strategy for the treatment of arginine-auxotrophic tumors [60]. Arginine deiminase (ADI) pathway is widely developed among bacteria to generate anerobic energy and protect them from acidic conditions [61, 62]. ADI is an enzyme which catalyzes the hydrolysis of L-arginine to L-citrulline and ammonia, the first step of ADI pathway. Recombinant *Mycoplasma* ADI is an example of ADT [63, 64]. When applied to arginine-auxotrophic tumors, recombinant ADI converts extracellular arginine to citrulline, and consequently starves cancer cells [65]. Recombinant ADI induces atypical or excessive autophagy. This type of cell death mechanism is different from classic caspase-dependent apoptosis and combination with conventional chemotherapies can lead to synergistic tumor growth inhibition [66, 67].

However, the use of recombinant ADI as anti-tumor agent is limited by several drawbacks. First, recombinant ADI shows short circulatory half-life and high immunogenicity in human due to its microbial origin. It has a short serum half-life

which is less than 5 hours *in vivo*, thus should be administered to patients frequently. It is strongly antigenic to mammals and vulnerable to proteolysis. To solve the above-mentioned problems, PEGylated ADI has been used in clinical trials and studies. PEGylation is the chemical modification of proteins by linking polyethylene glycol (PEG) chains [68]. It allows for reduced kidney filtration and reduced access of proteolytic enzymes [69]. However, PEGylation has potential drawbacks such as immunogenicity, decreased protein activity, and reduced intracellular uptake [70].

Secondly, subsequent ASS1-mediated arginine regeneration reduces treatment efficacy of recombinant ADI. When cancer cells are exposed to recombinant ADI, they begin to express ASS1 to synthesize arginine by themselves [53, 71]. As recombinant ADI cannot be delivered to cancer cells, intracellular arginine is not degraded, resulting in ADI resistance [72, 73]. Lastly, recombinant ADI is prone to form inclusion bodies in *E. coli* and requires extra steps to turn back into biologically active form with proper folding [74]. Therefore, solubility of recombinant ADI needs to be increased. Fusion with solubility enhancers, such as ArsC, Tsf, Mdh, and EDA has been used as a tool for solubility enhancement [75-77].

30Kc19 is a cell-penetrating protein originating from silkworm hemolymph [78-84]. Unlike other CPPs, it is also known as solubility enhancer and enzyme stabilizer [8, 11-13]. 30Kc19α is the N-terminal α-helix domain of 30Kc19 and retains functions exhibited by 30Kc19. Due to its smaller size, it shows higher cell-penetrating efficiency than whole protein [14, 85-87]. In a previous study, Park connected ADI and 30Kc19α with cleavable linker which contains a site sensitive to specific protease, matrix metalloproteinase-2 (MMP-2) for tumor-targeting effect and recovery of enzymatic activity [88, 89].

Herein, I propose fusion of recombinant ADI and 30Kc19α as a versatile

strategy to overcome instability, intracellular resistance, and insoluble expression of recombinant ADI from *Mycoplasma hominis* [90]. In this study, melanoma cells were selected as targets for the fusion protein. I investigated whether the ADI-LK-30Kc19α fusion protein could enhance solubility, enzyme stability, and intracellular delivery of recombinant ADI. The data showed that the fusion protein was expressed in soluble form, was stable in the presence of serum or protease, and was delivered into melanoma cells. It exhibited higher and more selective cytotoxicity to melanoma cells than recombinant ADI, and overcame ADI resistance in melanoma cells. Consequently, the findings suggest that ADI-LK-30Kc19α would be a promising ADT strategy for melanoma as well as other arginine-auxotrophic tumors.

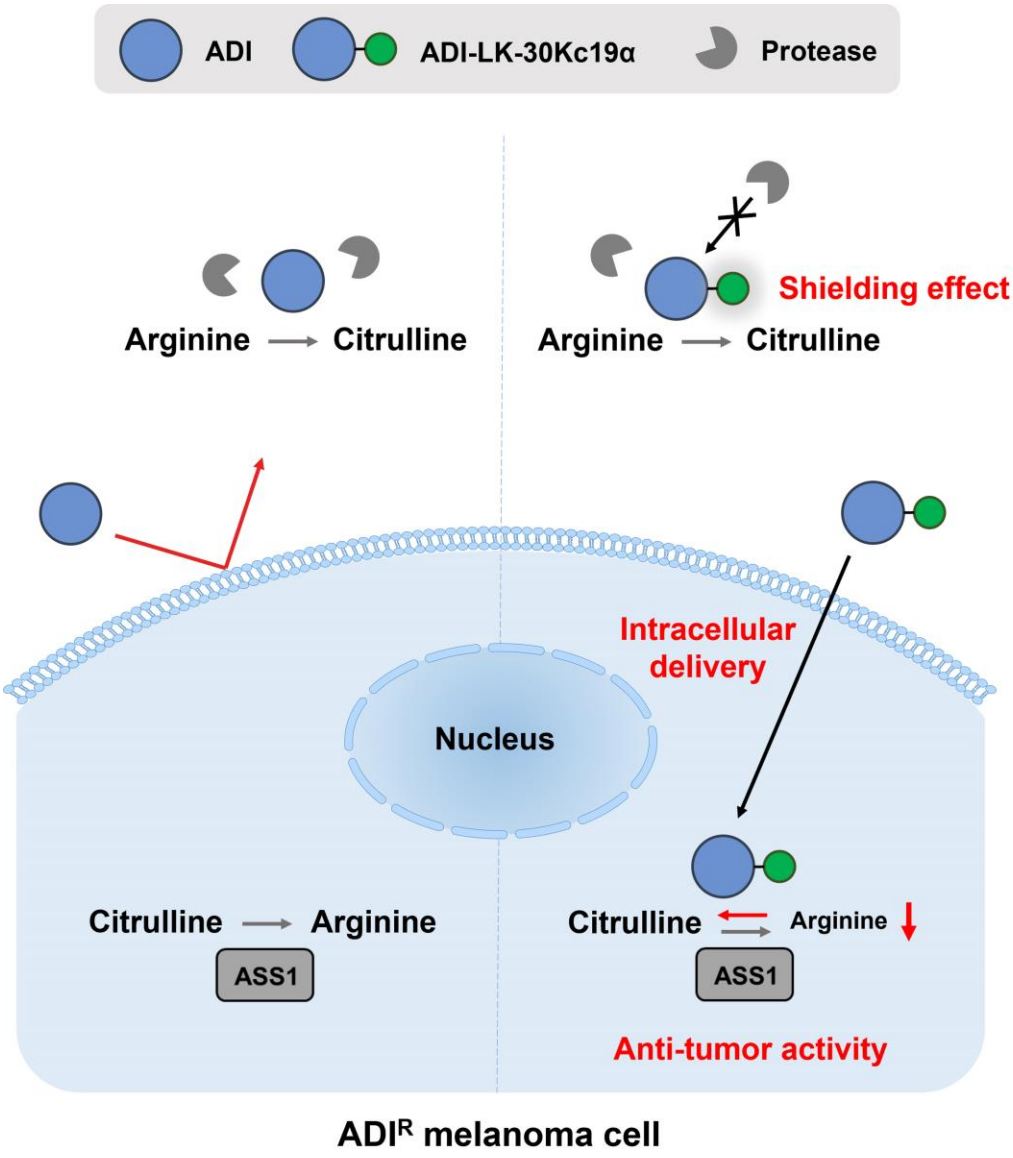

Figure 4.1. A schematic illustration of chapter 4.

4.2. Enhanced solubility and yield of recombinant ADI in *E. coli via* fusion with 30Kc19α

Recombinant ADI from *Mycoplasma hominis* is prone to be expressed as inclusion bodies in *E. coli*. In previous studies, 30Kc19 and its subunit, 30Kc19α have shown characteristics as solubility enhancers [12, 86]. To confirm this effect, pET-23a/*arcA* and pET-23a/*arcA-LK-30Kc19α* were constructed to produce recombinant ADI and ADI-LK-30Kc19α (Figure 4.2A). As shown in Figure 4.2B, when ADI and 30Kc19α were directly fused without a linker, the relative ADI activity (%) of ADI-30Kc19α was reduced by 7.69%. Therefore, MMP-2 cleavable sequence (LK) was inserted as a linker between ADI and 30Kc19α domains of ADI-LK-30Kc19α to reduce steric hindrance between two domains and to selectively act on melanoma cells. After expressing the recombinant proteins in *E. coli*, the supernatants and the pellets of *E. coli* lysates were analyzed by Coomassie blue staining and western blot to compare the solubility of ADI and ADI-LK-30Kc19α. Unlike ADI, ADI-LK-30Kc19α showed a distinct band in 60.4 kDa not only in pellet but also in supernatant (Figure 4.3A). Protein bands were analyzed using ImageJ software for quantification. The solubility of ADI-LK-30Kc19α was 29.18%, whereas that of ADI was only 3.70%. Following the expression of recombinant proteins in *E. coli*, the soluble fractions of proteins were purified using FPLC. The purified proteins were identified visually by Coomassie blue staining and western blot analysis (Figure 4.3A). The yield of purified ADI-LK-30Kc19α was 0.33 mg/L culture, which was 16.50 times higher than that of ADI 0.02 mg/L culture (Figure 4.3B). It was confirmed that fusion of recombinant ADI and 30Kc19α could increase the solubility and consequently, the yield of recombinant ADI.

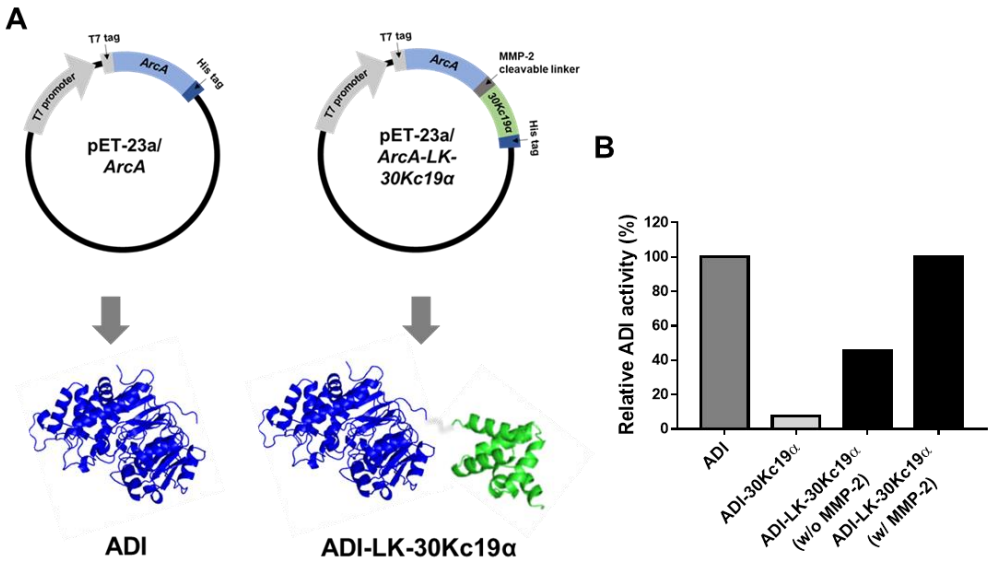

Figure 4.2. Fusion of 30Kc19α to ADI. (A) Plasmid construction of pET-23a/*ArcA* and pET-23a/*ArcA-LK-30Kc19α* and protein structures of ADI and ADI-LK-30Kc19α. Protein structure was visualized by Chimera software. C-terminus of ADI and N-terminus of 30Kc19α were connected by MMP-2 cleavable linker. (B) Relative ADI activity (%) of ADI-30Kc19α and ADI-LK-30Kc19α (before and after linker cleavage by MMP-2) compared to ADI.

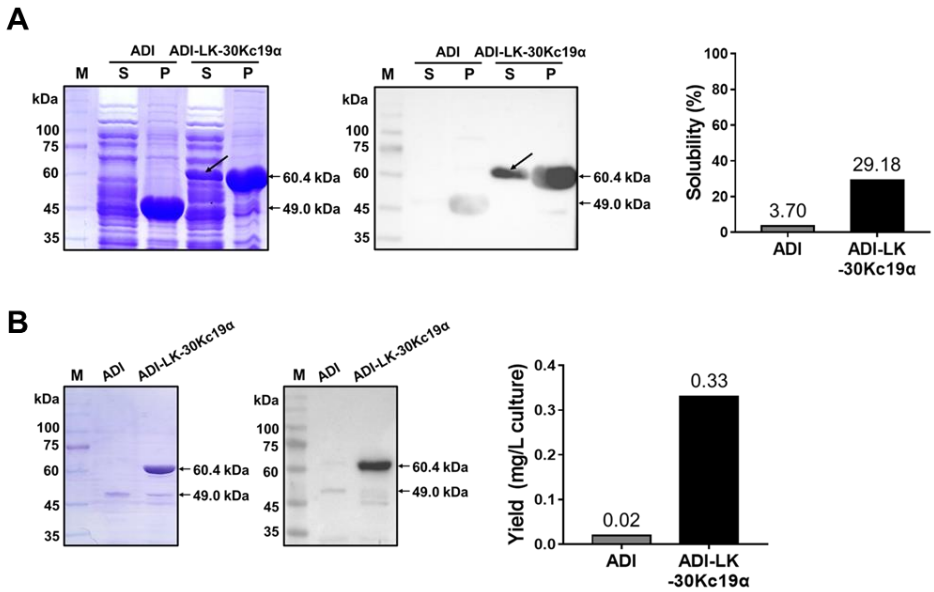

Figure 4.3. Fusion ADI and 30Kc19α and its effects on soluble expression and yield of recombinant ADI in *E. coli*. (A) Coomassie blue staining and western blot analysis of unpurified proteins showing fractions of soluble and insoluble expression in *E. coli*. Anti-T7 tag antibody was used as primary antibody for ADI and ADI-LK-30Kc19α. The black arrow indicates soluble-expressed ADI-LK-30Kc19α. M, marker; S, supernatant; P, pellet. Quantification of solubility (%) of ADI and ADI-LK-30Kc19α. (B) Coomassie blue staining and western blot analysis of purified ADI and ADI- ADI-LK-30Kc19α. Anti-T7 tag antibody was used as a primary antibody. M, Marker. Quantification of yield (mg/L culture) of purified ADI and ADI-LK-30Kc19α. Protein concentrations were calculated from BSA standards in SDS-PAGE gel using ImageJ software.

4.3. Improved stability and proteolytic resistance of ADI through fusion with 30Kc19α

Stability is an important pharmacological parameter and determines the efficacy of enzymatic drugs. *Mycoplasma* originating ADI also has stability issues [91]. As 30Kc19α acts as a protein stabilizer, the effect of 30Kc19α on the *in vitro* stability of ADI was investigated [14, 87]. Recombinant proteins were added to diluted FBS and incubated at 37℃. After at regular intervals, enzyme activity was analyzed. Compared to ADI, ADI-LK-30Kc19α showed enhanced stability. After 4 days, the remaining activity of ADI was about 33%, while the activity of the fusion protein was more than 50% (Figure 4.4A). Referring to El-Sayed, *in vitro* proteolysis assay was performed using two proteases: trypsin and proteinase K [51]. *In silico* prediction of potential proteolysis by trypsin and proteinase K in ADI was performed using ExPASy-PeptideCutter tool. As shown in Figure 4.4B, there are 43 and 226 cleavage sites by trypsin and proteinase K in ADI, respectively. The remaining ADI activities for both enzymes were determined after 15, 30, 60 min incubation with protease treatment. Fusion protein was more resistant to proteolysis compared to ADI alone (Figures 4.4C, D). This suggests that 30Kc19α could protect ADI from proteolysis by its shielding effect and could lead to enhancement of ADI stability.

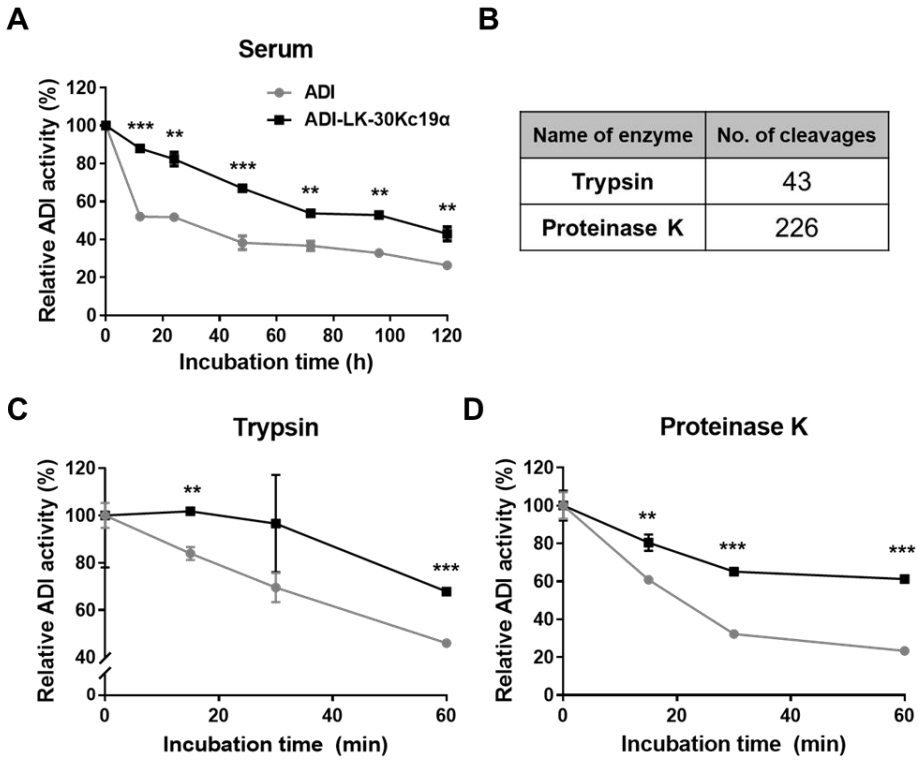

Name of enzyme	No. of cleavages
Trypsin	43
Proteinase K	226

Figure 4.4. Stabilization of ADI by fusion with 30Kc19α. (A) Serum stability assay. 4 μM of proteins were incubated with FBS at 37°C from 0 to 120 hours. The relative ADI activity (%) was obtained by normalizing ADI activity at each time point to ADI activity at t = 0. (B) Prediction of potential proteolysis by trypsin and proteinase K in ADI. ExPASy-PeptideCutter tool was used for analysis. (C, D) *In vitro* proteolysis assay using 1 μg/ml of trypsin (C) and 100 ng/ml of proteinase K (D). The relative ADI activity (%) was obtained by normalizing ADI activity at each time point to ADI activity at t = 0 (**$p < 0.01$, ***$p < 0.001$).

4.4. Intracellular delivery of ADI by 30Kc19α prior to linker cleavage

When melanoma cells are exposed to ADI, ASS1 expression increases within a short period of time, and arginine biosynthesis occurs therein [53]. It was confirmed through real-time RT-PCR that *ASS1* mRNA expression in SK-MEL-2 increased by 46.36 times when ADI was treated for 72 hours (Figure 4.5A). ADI only depletes extracellular arginine because it cannot penetrate cells. Therefore, if intracellular delivery of ADI is possible, intracellularly synthesized arginine can also be degraded. Since MMP-2 cleavable linker was used, the linker could be cleaved before and after cell-penetration, affecting cell-penetration efficiency.

To evaluate the cell-penetrating ability resulting from the fusion of ADI with 30Kc19α, ICC staining was performed. SK-MEL-2 cells were treated with 1 μM ADI or 1 μM ADI-LK-30Kc19α for 1 hour, and then cell-penetration was confirmed by CLSM. As T7 tag is located on the N-terminus of recombinant proteins, anti-T7 tag antibody was used. Strong green fluorescence was detected in ADI-LK-30Kc19α-treated SK-MEL-2 (Figure 4.5B). This indicates the fusion of ADI and 30Kc19α enabled cellular uptake of ADI despite the use of MMP-2 cleavable linker.

To quantify the cell-penetrated proteins, HiBiT lytic detection system was performed. HiBiT tag, a 11 aa peptide, was added to the N-terminus of ADI and ADI-LK-30Kc19α. When HiBiT meets LgBiT, then NanoLuc luciferase is formed, which produces a luminescent signal in the presence of substrate [92]. HiBiT-tagged recombinant proteins were produced and validated (Figure 4.5C). SK-MEL-2 cells were treated with 100 nM or 1 μM HiBiT-tagged recombinant proteins for 24 hours. Then, cells were lysed and treated with LgBiT containing reagent. Cell-penetrated

HiBiT-tagged proteins were quantified by measuring luminescence and using purified HiBiT-tagged protein standard curve (Figure 4.5D). A statistically significant difference was found between ADI and ADI-LK-30Kc19α-treated groups (Figure 4.5E). Luminescence in the ADI-LK-30Kc19α group was 2.32 and 12.35 times higher than that of the ADI group at 100 nM and 1 μM.

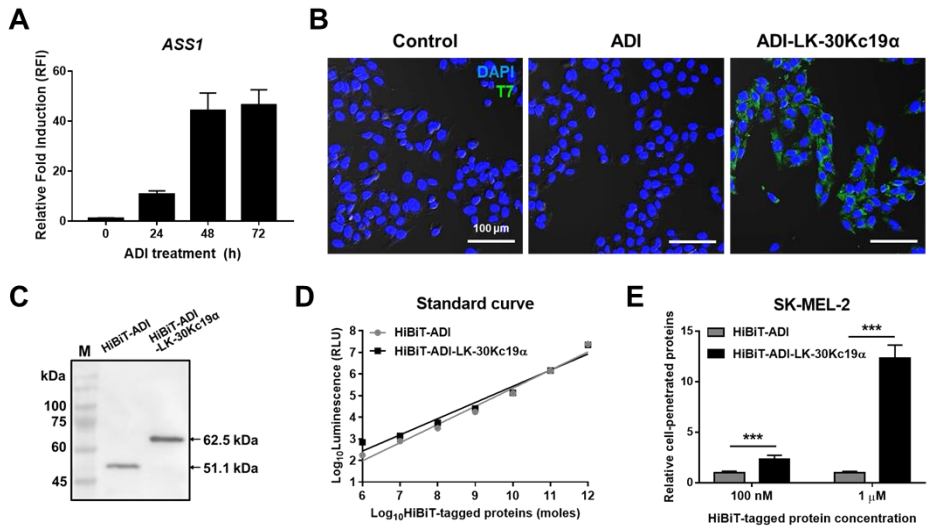

Figure 4.5. Intracellular delivery of ADI by fusion with 30Kc19α. (A) *ASS1* mRNA expression level measured by real-time RT-PCR. SK-MEL-2 was treated with 1 mU/ml of recombinant ADI for up to 72 hours. *ASS1* mRNA expression was normalized to *GAPDH,* and relative fold induction (RFI) was calculated relative to the control group. (B) Confocal image of SK-MEL-2 showing the cell-penetration of ADI-LK-30Kc19α. Anti-T7 tag antibody was used as primary antibody for recombinant proteins (Scale bar = 100 μm). (C) Western blot analysis of purified HiBiT-tagged ADI and ADI-LK-30Kc19α. (D) Standard curve for HiBiT-tagged protein quantification. Standard curves were obtained for HiBiT-ADI (gray) and HiBiT-ADI-LK-30Kc19α (black) by graphing the data (Log_{10}Luminescence versus Log_{10}HiBiT-tagged proteins). (E) Cell-penetrated protein quantification using HiBiT lytic detection system. SK-MEL-2 cells were treated with 100 nM or 1 μM of HiBiT-tagged proteins for 24 hours. Luminescence was measured after DPBS washing and LgBiT-containing reagent treatment. Number of cell-penetrated proteins were calculated by luminescence and stadard curves of purified HiBiT-tagged proteins. Then, data are expressed as relative cell-penetrated proteins normalized to HiBiT-ADI-treated group (***$p < 0.001$).

4.5. Overcoming ADI resistance through intracellular delivery of ADI and intracellular arginine degradation

To confirm the effect of intracellular delivery of ADI on overcoming ADI resistance, ADI^R SK-MEL-2, an ADI-resistant melanoma cell line, was established. As described in Figure 4.6A, SK-MEL-2 cells were continuously exposed to ADI for 2 months. *ASS1* mRNA expression level of ADI^R SK-MEL-2 was increased 140-fold compared to SK-MEL-2, indicating development of ADI^R SK-MEL-2 (Figure 4.6B). ADI^R SK-MEL-2 cells were treated with ADI or ADI-LK-30Kc19α for 72 hours, then cell viability was measured using CELLOMAX™ cell viability assay. ADI^R SK-MEL-2 cells showed about 70% cell viability despite high concentration of ADI treatment. On the other hand, when ADI^R SK-MEL-2 cells were treated with ADI-LK-30Kc19α, cell viability was significantly reduced to about 35% (Figure 4.6C). It suggests that ADI-LK-30Kc19α overcomes the ADI resistance in ADI^R SK-MEL-2.

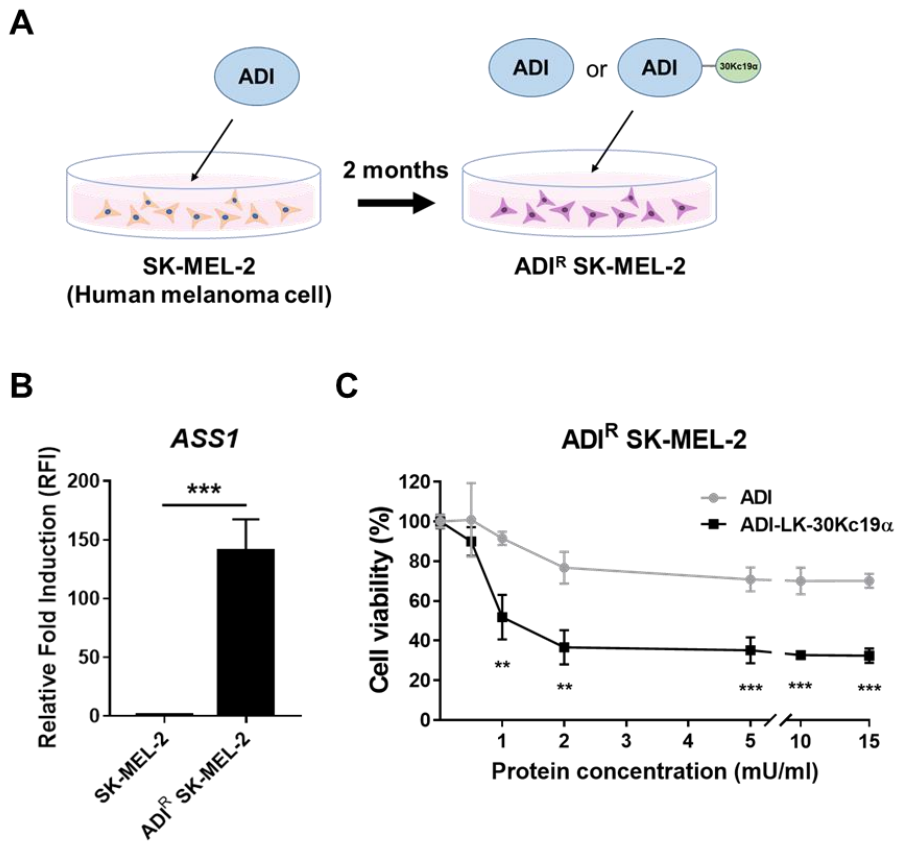

Figure 4.6. Development of ADI-resistant melanoma cell and overcoming ADI resistance. (A) Establishment of ADI^R SK-MEL-2 with increasing concentrations of ADI. SK-MEL-2 cells were continuously exposed to ADI for 2 months. (B) *ASS1* mRNA expression level of SK-MEL-2 and ADI^R SK-MEL-2 measured by real-time RT-PCR. *ASS1* mRNA expression was normalized to *GAPDH*, and RFI was calculated relative to SK-MEL-2. (C) Dose-dependent cytotoxicity of ADI and ADI-LK-30Kc19α on ADIR SK-MEL-2. Cell viability was measured by CELLOMAX^{TM} viability assay at 72 hours after treatment with recombinant proteins. Data are expressed as relative cell viability (%) normalized to the control group (without protein treatment) (**$p < 0.01$, ***$p < 0.001$).

4.6. Conclusions

In this study, I fused 30Kc19α and *Mycoplasma* arginine deiminase (ADI) to overcome some drawbacks of recombinant ADI. The results show that the soluble expression and yield of ADI were enhanced through fusion with 30Kc19α in *E. coli* expression system. ADI-LK-30Kc19α was more stable and resistant to proteolysis than ADI. It was able to penetrate melanoma cells, thus overcoming ADI-resistance in melanoma cells. Overall, the fusion of ADI with multifunctional CPPs, 30Kc19α, could solve the limitations of recombinant ADI, and thus could be applied to improve the efficacy of ADI in melanoma treatment.

Chapter 5

Intracellular delivery of recombinant RUNX2 facilitated by 30Kc19α for osteogenic differentiation of hMSCs and bone regeneration

Chapter 5. Intracellular delivery of recombinant RUNX2 facilitated by 30Kc19α for osteogenic differentiation of hMSCs and bone regeneration

5.1. Introduction

Patient-derived cell therapy has been studied as a potential solution for bone-related diseases. Human mesenchymal stem cells (hMSCs) serve as an excellent and abundant autologous cell source that can be differentiated into multiple lineages *in vitro* and *in vivo* [93, 94]. One of the advantages of using hMSCs is that they can be programmed to commit to a specified cell-type in a highly efficient manner with defined factors. Conventional methods of stem cell differentiation involve growth factor-induced intracellular signaling activation [95]. Furthermore, small molecules binding to intracellular signal transduction molecules can also modulate downstream signaling. Even though growth factor- or small molecule-dependent stem cell differentiation is effective, it may activate diverse signaling pathways, resulting in non-specific results [96]. For example, bone morphogenetic protein 2 (BMP-2), a member of transforming growth factor-β (TGF-β) superfamily, is well-known for its effects on bone formation. However, BMP-2 has been found to play important roles in almost all organ systems, including bone, which makes it more likely to cause side effects [96]. Therefore, biological factors that are more specific to stem cell differentiation are needed for the replacement of the above methods.

In recent studies, activation or upregulation of a single transcription factor is sufficient to elicit stem cell commitment [97-102]. Out of many osteogenic-specific transcription factors, runt-related transcription factor 2 (RUNX2) is a master regulator of osteogenesis, which makes it an excellent candidate for a downstream

target [103]. RUNX2 has high binding affinity to the promoter regions of osteogenic marker genes (i.e. osterix, collagen type 1, and bone sialoprotein), and upregulates their gene expressions [104-107]. Previously, osteogenic differentiation of hMSCs was accomplished by stimulation of RUNX2 gene expression or direct RUNX2 gene delivery [108, 109]. In comparison with genetic manipulation, protein delivery is an attractive strategy, in that it minimizes the risk of oncogenic mutation or undesired genome alteration, and bypasses the challenges related to transcription and translation [16, 110]. However, intracellular delivery of recombinant transcription factors that include RUNX2 may be hindered by its large molecular size. Therefore, a 'delivery assistant' is needed for RUNX2 to penetrate through the cell membrane. Furthermore, recombinant RUNX2 is expressed in insoluble form in *E. coli*, which requires additional refolding steps, and may result in structurally inaccurate protein products.

CPPs have been utilized as vehicles for the intracellular delivery of various cargos, including proteins [15, 111]. 30Kc19 is a protein originating from silkworm hemolymph, famous for its anti-apoptotic effect [78-81]. In addition to the inhibition of apoptosis, 30Kc19 has shown successful protein delivery into cells [9]. Previous studies have discovered that it has cell-penetrating ability due to its intrinsic CPP, Pep-c19 [10]. Different from other CPPs, 30Kc19 has additional functions to cell-penetrating ability: protein stabilization, and enhancement of soluble expression [8, 12]. For example, fusing 30Kc19 improved the stability, and resulted in the soluble expression of transcription factors [12]. Ryu *et al*. examined the solubility of the 30Kc19α and 30Kc19β parts of 30Kc19 whole protein, and showed that 30Kc19α-only can be produced in soluble form [14]. However, whether 30Kc19α can induce solubility in insoluble cargo protein products has not been examined.

Herein, I demonstrated the fusion of 30Kc19α enhanced solubility in insoluble recombinant RUNX2. In addition, fusion of 30Kc19α and RUNX2 solved the other above-mentioned problems of recombinant RUNX2 *in vitro* [112]. Application in *in vivo* also showed bone regeneration capacity of 30Kc19α-RUNX2-treated hMSCs *via* incorporating gelatin cryogel. Recently, studies on gelatin cryogels have been increased due to its inherent peptide sequences that allow cell attachment and natural enzymatic degradation characteristics which provide favorable environment for cells [113-115]. Thus, I fabricated gelatin cryogel in *in vivo* experiments to deliver 30Kc19α-RUNX2-treated hMSCs in mice. Together, I report 30Kc19α-mediated intracellular delivery of osteogenic transcription factor is an efficient method for the osteogenic induction in hMSCs *in vitro* and *in vivo* [86].

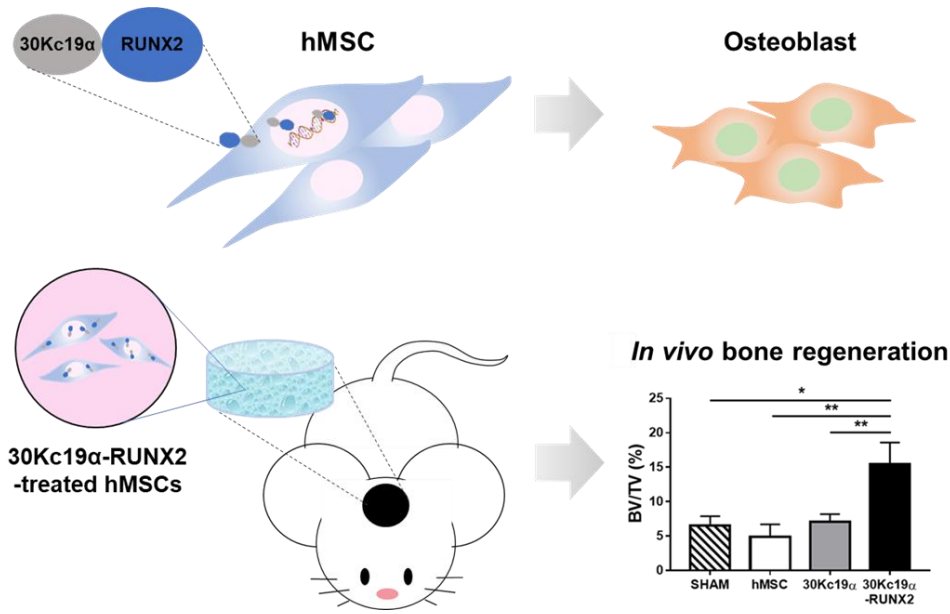

Figure 5.1. A schematic illustration of chapter 5.

5.2. Enhanced soluble expression and cell-penetration ability of recombinant RUNX2 *via* fusion with 30Kc19α

To produce recombinant RUNX2 protein, recombinant plasmid pET-23a/*RUNX2* was constructed. Then, *30Kc19α* gene was cloned into pET-23a/*RUNX2* to produce recombinant RUNX2 protein with a cell-penetrating ability (Figure 5.2). Recombinant RUNX2 and 30Kc19α-RUNX2 were expressed in *E. coli*, and purified using FPLC. Recombinant RUNX2 was expressed in insoluble form, so additional solubilization and refolding steps were performed. Coomassie blue staining and western blot analysis showed bands, which are expected to be recombinant RUNX2 and 30Kc19α-RUNX2 (Figure 5.3A). After expressing the recombinant proteins in *E. coli*, the supernatants (soluble fraction) and the pellets (insoluble fraction) of cell lysates were analyzed by western blot, to compare the solubility of RUNX2 and 30Kc19α-RUNX2. Figure 5.3B shows that the solubility of 30Kc19α-RUNX2 was 14.99%, whereas that of RUNX2 was only 1.31%. It was confirmed that recombinant RUNX2 fused with 30Kc19α can increase the solubility.

As recombinant RUNX2 was expressed as an inclusion body in *E. coli*, protein stability enhancement effect of 30Kc19α could not be confirmed in recombinant RUNX2. Therefore, only the *in vitro* stability of 30Kc19α-RUNX2 was analyzed by western blot analysis. 30Kc19α-RUNX2 was incubated with serum-containing medium at 37°C for up to 48 hours. The western blot analysis data showed that some fusion proteins were stable even after 48 hours of incubation (Figure 5.3C).

Furthermore, intracellular and nuclear delivery of recombinant proteins were investigated by ICC staining (Figure 5.3D). Initially, intracellular delivery of 30Kc19α alone was observed. Since the recombinant 30Kc19α has T7 tag sequence,

anti-T7 tag antibody was used for ICC staining of 30Kc19α. Evenly distributed 30Kc19α protein were observed in the cytosol. Next, intracellular delivery of unfused RUNX2 and 30Kc19α-RUNX2 was observed. Recombinant RUNX2 was not observed in the cell as expected. 30Kc19α-RUNX2 was observed not only in the cytosol, but also in the nucleus of hMSCs (Figure 5.3D). This demonstrates the intracellular translocation ability of 30Kc19α and suggests that unlike treatment of 30Kc19α, 30Kc19α-RUNX2 has been delivered into the nucleus. It also confirms that His tag does not have impact on 30Kc19α-RUNX2 penetrating the cell membrane.

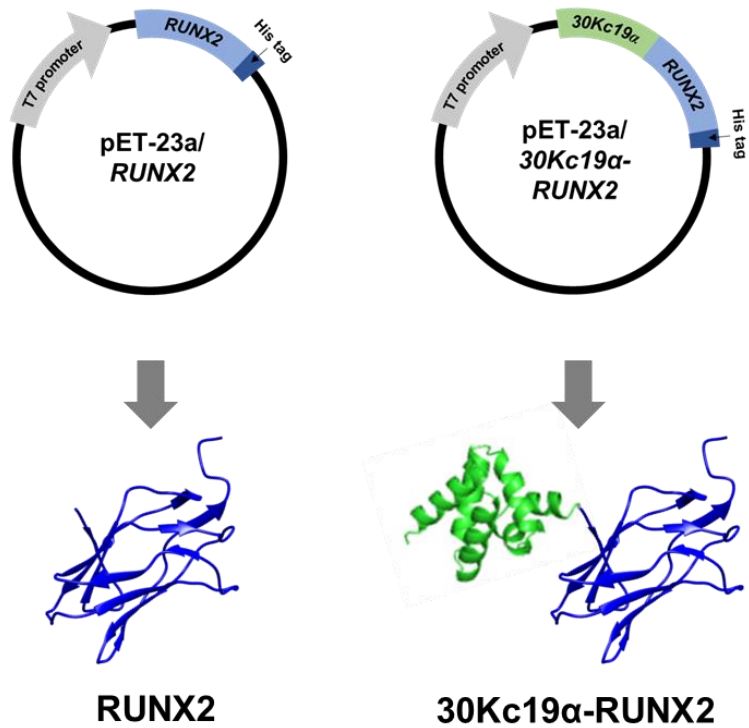

Figure 5.2. Fusion of 30Kc19α to RUNX2. Plasmid construction of pET-23a/*RUNX2* and pET-23a/*30Kc19α-RUNX2* and protein structures of RUNX2 and 30Kc19α-RUNX2. Protein structure was visualized by Chimera software.

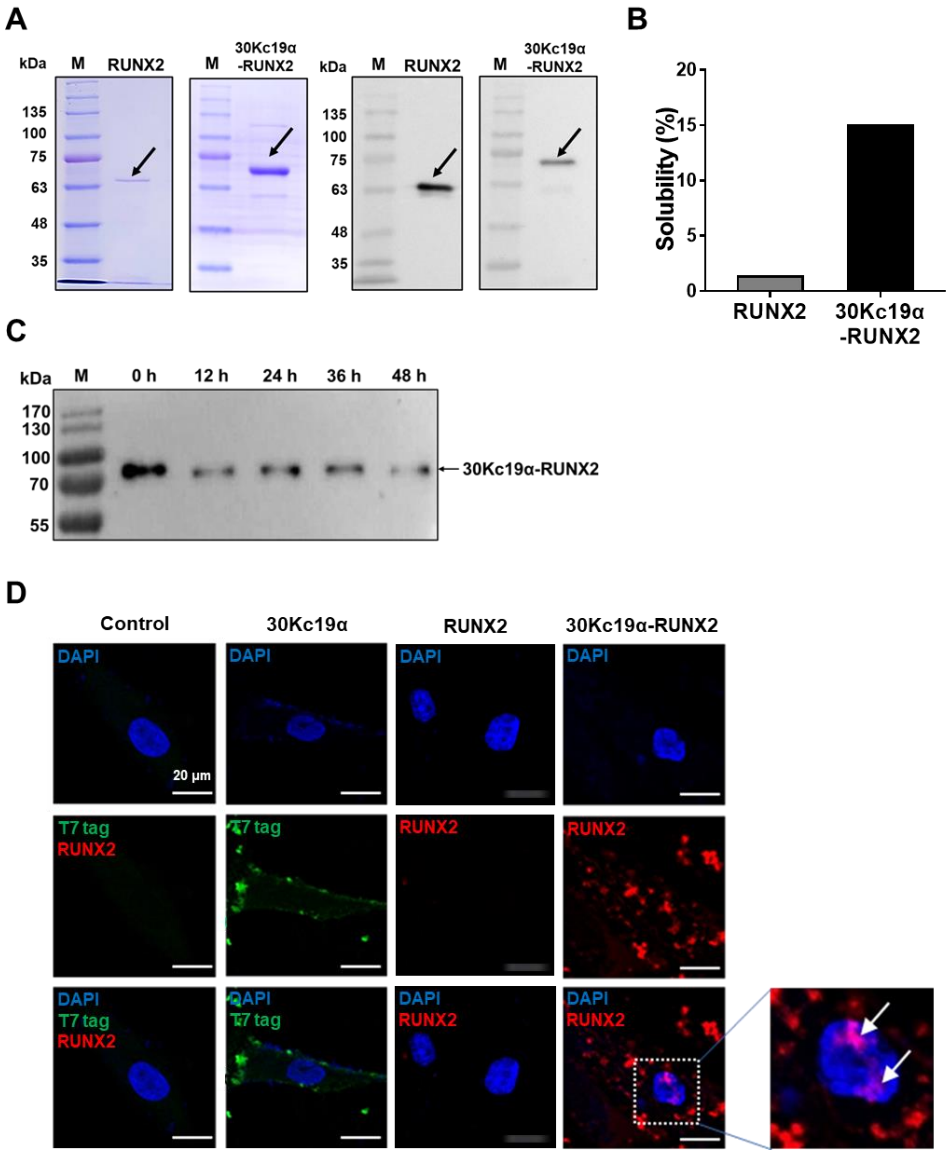
A
kDa
M
RUNX2
30Kc19α
-RUNX2
135
100
75
63
48
35
B
Solubility (%)
20
15
10
5
0
RUNX2
30Kc19α
-RUNX2
C
0 h
12 h
24 h
36 h
48 h
170
130
100
70
55
30Kc19α-RUNX2
D
Control
30Kc19α
RUNX2
30Kc19α-RUNX2
DAPI
20 μm
T7 tag
RUNX2

Figure 5.3. Soluble expression and intracellular and nuclear delivery of 30Kc19α-RUNX2. (A) Coomassie blue staining and western blot analysis of recombinant RUNX2 and 30Kc19α-RUNX2. Anti-His tag antibody was used as primary antibody for purified recombinant proteins. M, marker. (B) Quantification of solubility (%) of RUNX2 and 30Kc19α-RUNX2. (C) *In vitro* stability of 30Kc19α-RUNX2. 30Kc19α-RUNX2 was incubated in serum containing media at 37°C and was analyzed after 0, 12, 24, 36, 48 hours. Anti-His tag antibody was used as primary antibody. (D) Confocal image of protein-treated hMSCs showing the cell-penetration of 30Kc19α and 30Kc19α-RUNX2. Anti-T7 tag antibody was used as primary antibody for 30Kc19α, and anti-RUNX2 antibody for recombinant RUNX2 and 30Kc19α-RUNX2. Blue, green, and red fluorescence represent nucleus (DAPI), 30Kc19α (Alexa Fluro® 488), and recombinant proteins containing RUNX2 (Alexa Fluro® 594), respectively. White arrows indicate 30Kc19α-RUNX2 located in nucleus (Scale bar = 50 μm).

5.3. Efficient osteogenic differentiation of hMSCs treated with recombinant 30Kc19α-RUNX2

Since recombinant RUNX2 protein without 30Kc19α cannot be delivered into hMSCs and function as transcription factor, recombinant RUNX2 was excluded from experimental groups for *in vitro* and *in vivo* osteogenic analysis. Instead of recombinant RUNX2, 30Kc19α was included as an experimental group. The ability of 30Kc19α and 30Kc19α-RUNX2 to induce and promote osteogenesis of hMSCs was examined by adding recombinant proteins to osteogenic medium for the first two days of the osteogenic culture. Changes in gene regulation due to added recombinant proteins were observed *via* real-time qRT-PCR analysis. *Collagen type 1* (*COL1*), *osteopontin* (*OPN*), and *osteocalcin* (*OCN*) are three osteoblast-specific genes activated in different stages of osteogenic differentiation [116-118]. On day 14, a statistically significant difference was found between the control and 30Kc19α-RUNX2 groups in *COL1*, *OPN*, and *OCN*, whereas 30Kc19α group showed similar gene expression levels to the control group (Figure 5.4A). In particular, the mRNA expression level of *OPN* was 15.3-fold higher in the 30Kc19α-RUNX2 group, compared to that of the control group. On day 21, statistically significant difference existed between the control and 30Kc19α-RUNX2 group in *OCN* expression only. The mRNA expression level of *OCN* was 19.5-fold higher in the 30Kc19α-RUNX2 group, compared to the control (Figure 5.4C).

In addition to real-time PCR data, ICC staining of cells further verified the osteogenic inducing capacity of 30Kc19α-RUNX2. The protein expression level of OPN confirmed the enhanced osteogenic induction in the 30Kc19α-RUNX2 group at day 14 (Figure 5.4B). The difference in OPN expression was about twice higher

in hMSCs treated with 30Kc19α-RUNX2 than in other groups. On day 21, the fluorescence intensities of all three groups increased, and as the osteogenesis of hMSCs progressed, the difference among groups decreased. However, the increase in OPN expression of other groups did not exceed that of the 30Kc19α-RUNX2 group (Figure 5.4D).

The effect of 30Kc19α-RUNX2 on ALP expression and mineral deposition of hMSCs was verified *via* ALP staining and ARS staining (Figure 5.4E). ALP staining uses p-nitrophenyl phosphate (pNPP) as phosphatase substrate which turns color when dephosphorylated by ALP. ARS has the tendency to bind to calcium which allows visualization of calcium deposition of cells. ALP expression after 7 days of osteogenic culture of 30Kc19α-RUNX2-treated hMSCs was highest, compared to that of the control and 30Kc19α groups. In addition, 14 days of osteogenic culture of 30Kc19α-RUNX2-treated hMSCs showed both prominent ALP activity and calcium deposition (shown in red), compared to the other two groups. On day 21 of the osteogenic culture, some calcium deposition was observed in the control group. However, the 30Kc19α-RUNX2 group showed the strongest staining. Calcium deposition in the 30Kc19α-RUNX2 group increased 1.09 times at day 21 compared to day 14. Altogether, both ALP and ARS staining suggest the successful enhancement of early and late osteogenesis in cells treated with 30Kc19α-RUNX2.

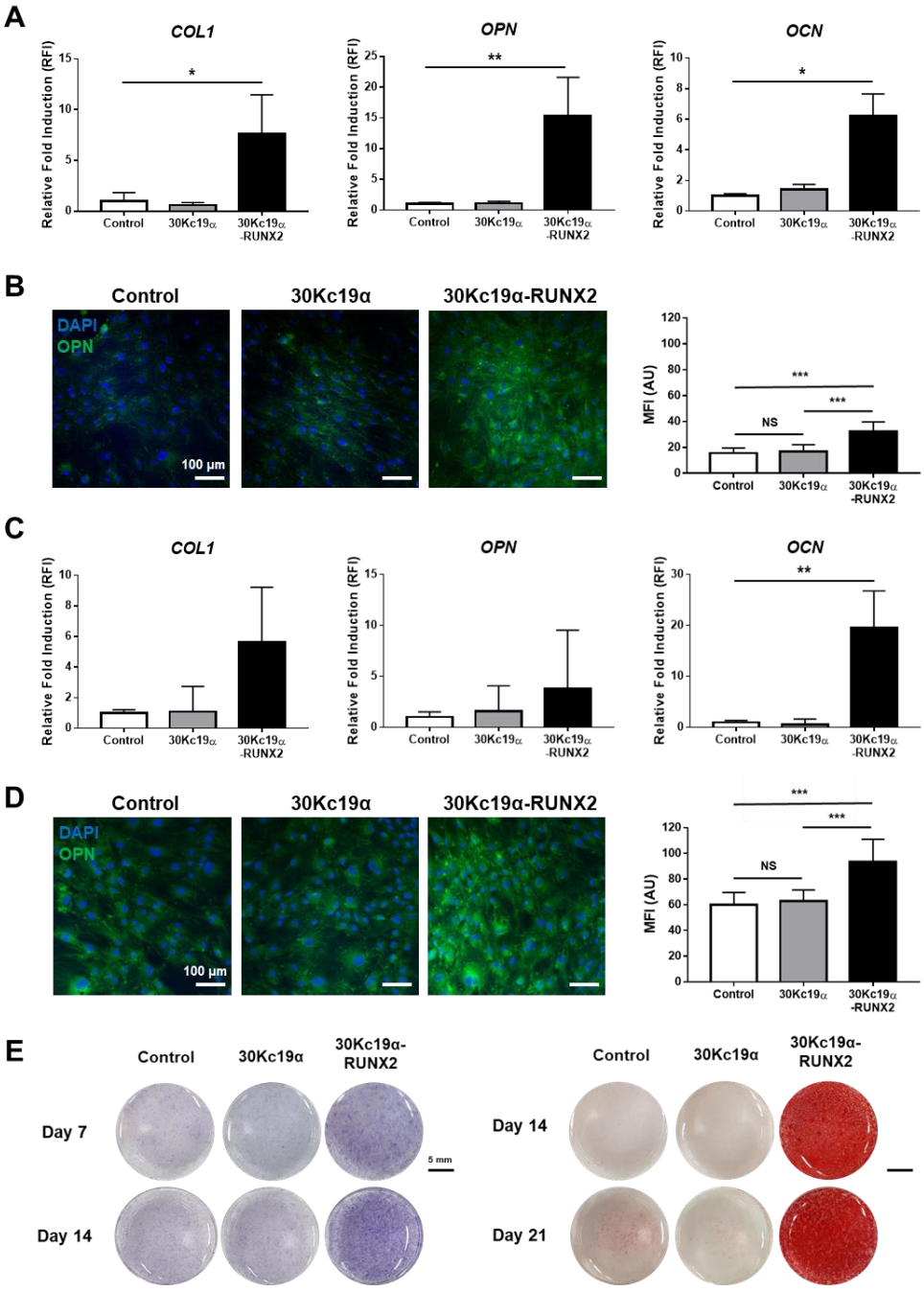
A
COL1
OPN
OCN
Relative Fold Induction (RFI)
Control
30Kc19α
30Kc19α -RUNX2
B
Control
30Kc19α
30Kc19α-RUNX2
DAPI
OPN
100 μm
MFI (AU)
NS
C
D
E
Day 7
Day 14
Day 21
5 mm

Figure 5.4. *In vitro* osteogenic induction capability of 30Kc19α-RUNX2. (A) Assessment of osteogenic marker gene expression profile (*COL1*, *OPN*, and *OCN*) *via* real-time PCR in day 14. hMSCs cultured in OM for 14 days were examined. Gene expression levels of osteogenic marker genes were normalized to *GAPDH*. Then, the normalized values were expressed as relative fold induction (RFI) over control group (*$p < 0.05$, **$p < 0.01$). (B) ICC analysis of OPN, and quantification of OPN expression in day 14. ICC staining was performed on hMSCs cultured for 14 days in OM. Anti-OPN antibody was used as primary antibody. Blue and green fluorescence represent nucleus and OPN, respectively. Mean fluorescence intensity of each group was measured by ImageJ software (Scale bar = 100 μm,. ***$p < 0.001$, NS, not significant). (C) Assessment of osteogenic marker gene expression profile (*COL1*, *OPN*, and *OCN*) *via* real-time PCR at day 21 (**$p < 0.01$). (D) ICC analysis of OPN, and quantification of OPN expression at day 21 (Scale bar = 100 μm. ***$p < 0.001$, NS, not significant). (E) ALP staining and ARS staining data showing ALP expression and calcium deposition in hMSCs. ALP staining was performed on hMSCs cultured for (7 and 14) days in OM, and ARS staining was performed on hMSCs cultured for (14 and 21) days in OM (Scale bar = 5 mm).

5.4. Effective osteogenic commitment *via* 30Kc19α-RUNX2 without osteo-induction factor, dexamethasone

Dexamethasone is a strong osteo-inductive steroid that has been shown to activate *RUNX2* gene expression. In order to assess whether 30Kc19α-RUNX2 can elicit osteogenic commitment in hMSCs without osteo-induction factor, differentiation without dexamethasone was performed. Unlike the osteogenesis above, 30Kc19α-RUNX2 was delivered twice (each treatment was 48 hours apart) during the first 4 days of osteogenic culture. Since delayed osteogenic differentiation was expected compared to osteogenesis with dexamethasone, real-time PCR analysis was performed only on day 21, and staining was performed on day 14 and day 21. Real-time PCR analysis on day 21 showed the highest RFI values in 30Kc19α-RUNX2-treated groups in *COL1, OPN,* and *OCN* of (9.4, 1.4, and 11.2)-fold, respectively) (Figure 5.5). However, a statistically significant difference existed between the control and 30Kc19α-RUNX2 group only in *COL1* expression. The data show that 30Kc19α-RUNX2 induced osteogenic differentiation in hMSCs, while 30Kc19α does not have osteogenic inducing ability.

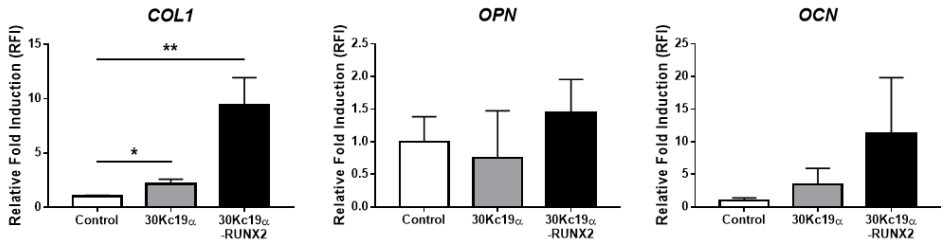

Figure 5.5. *In vitro* osteogenic induction capability of 30Kc19α-RUNX2 without dexamethasone. Assessment of osteogenic marker gene expression profile (*COL1*, *OPN*, and *OCN*) *via* real-time PCR. hMSCs cultured in OM without dexamethasone for 21 days were examined. Gene expression levels of osteogenic marker genes were normalized to *GAPDH*. Then, the normalized values were expressed as relative fold induction (RFI) over control group. *$p < 0.05$, **$p < 0.01$ compared with control group.

5.5. Fabrication of cryogel-based cell delivery platform for *in vivo* implantation

To observe bone regeneration *in vivo*, cells were seeded on macroporous gelatin cryogels, and delivered into the cranial defect sites of mice. Macroporosity allows cells and other nutrients to flow and interact with host cells *in vivo*. The macroporous gelatin cryogels were fabricated by self-crosslinking type A gelatin *via* EDC/NHS. Reaction mixture formed ice crystals as gelation occurred in -20 ℃ condition, and macropores were formed after freeze-drying the product (Figures 3.9.1, 5.6A). The average pore size was (93.53 ± 19.94) μm. Before seeding cells onto the scaffold, the swelling and mechanical property of the scaffold were assessed. The swelling ratio and Young's modulus of cryogel was (721.55 ± 60.18)% and (6.933 ± 0.544) kPa, respectively (Figure 5.6B). To test for cell viability, cells from all three groups were each seeded onto gelatin cryogel. After 24 h of culture on cryogels, Live/Dead assay was carried out, and confirmed that there was no cytotoxicity resulting from scaffolds (Figure 5.6C). Thus, the fabricated cryogel was macroporous and non-cytotoxic for cells to be seeded and delivered into the defect area.

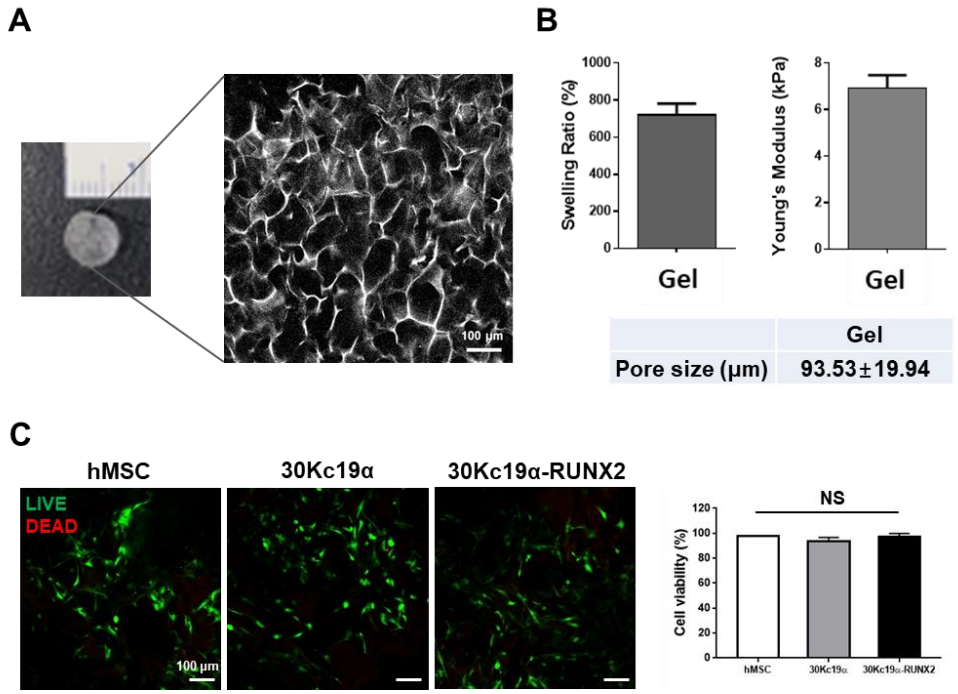

Figure 5.6. Characterization of gelatin cryogel and cytotoxicity measurement on hMSC-seeded cryogels. (A) Images showing cryogel at swollen state and macroporous network of cryogel. (B) Bar graphs for swelling ratio (%) and Young's modulus (kPa), as well as a table for the average pore size of cryogel. (C) Live and dead confocal images taken 24 h after seeding cells from each group, showing the low cytotoxicity of the material. Quantification is also shown in bar graph. NS, non-significant (Scale bar = 100 μm).

5.6. *In vivo* osteogenic differentiation in mouse subcutaneous model

To observe osteogenesis in *in vivo* condition, 2×10^6 cells were seeded onto gelatin cryogel, and the cryogels were implanted into mouse subcutaneous tissue. Four weeks after implantation, mice were sacrificed, and cryogels were collected for H&E and MTC histological stainings (Figure 5.7). MTC staining showed the highest collagen accumulation in cryogel seeded with 30Kc19α-RUNX2 treated cells (Figure 5.7B). While other cellular groups, hMSC and 30Kc19α, demonstrated a faint amount of blue stain (collagen), the acellular group, SHAM, did not show any sign of collagen staining. Thus, the elevated collagen content from 30Kc19α-RUNX2 group suggests that efficient osteogenic differentiation is induced *in vivo*.

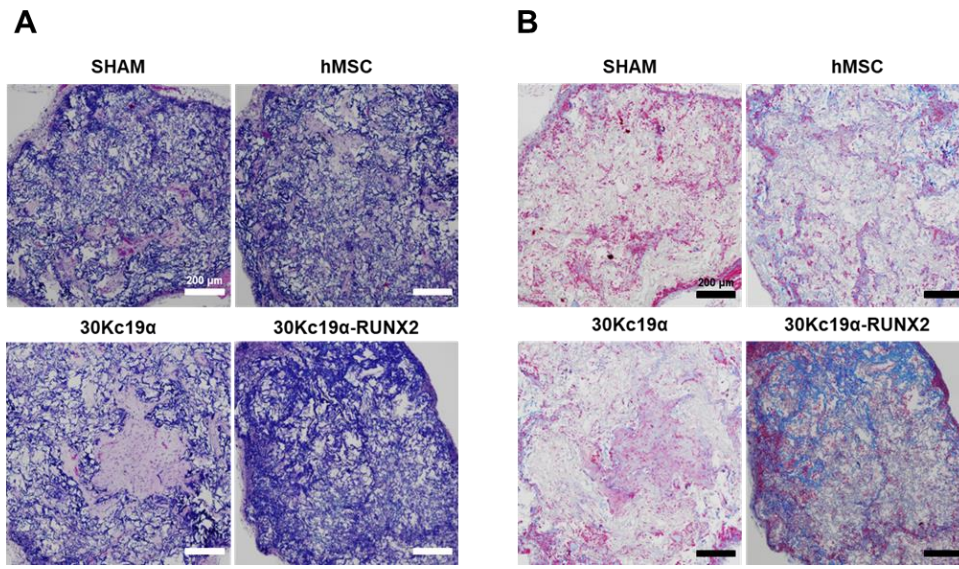

Figure 5.7. Enhanced *in vivo* osteogenesis in mouse subcutaneous tissue *via* 30Kc19α-RUNX2-treated hMSC-seeded gelatin cryogel. (A) H&E staining showing nuclei, ECM, and cytoplasm of seeded cells. (B) MTC staining showing accumulation of collagen content in cell-seeded cryogels (Scale bar = 200 µm).

5.7. *In vivo* bone regeneration in mouse cranial defect model

Cranial defects were made on mice to observe bone regeneration *in vivo*. A total of 2×10^6 cells from each group were seeded onto the gelatin cryogel, and were delivered to the defect sites. After 8 weeks, mice were sacrificed, and cranial bones were collected to be analyzed *via* micro-CT and histological staining. Micro-CT analysis images and quantification showed prominent new bone formation in 30Kc19α-RUNX2-treated cells, compared to other groups (Figures 5.8A, B). MTC histological staining of cranial bone with 30Kc19α-RUNX2-treated cells showed thicker formation of new bone in the defect area (Figure 5.8C). In addition, IF staining of histological samples with anti-OPN antibody confirmed the highest amount of regenerated bone in the 30Kc19α-RUNX2 group (Figure 5.8D). Enhanced new bone formation in the 30Kc19α-RUNX2-treated hMSC group suggests prominent bone regeneration potential *in vivo*.

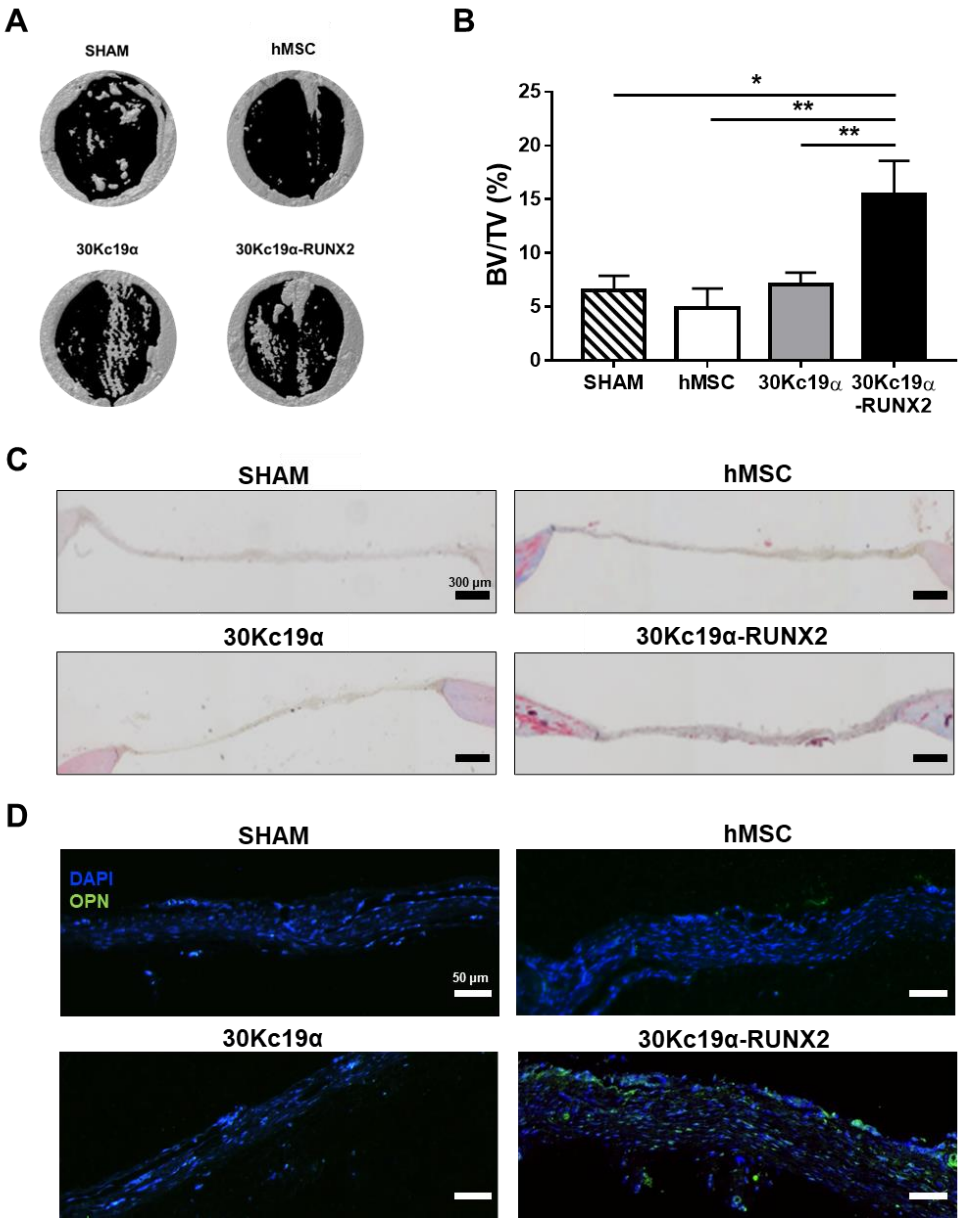

Figure 5.8. Enhanced *in vivo* bone regeneration in mouse cranial defect area *via* 30Kc19α-RUNX2-treated hMSC-seeded gelatin cryogel. (A) Micro-CT reconstruction images showing regenerated bone in defect area. (B) Percentages of regenerated bone volume quantified are shown (*$p < 0.05$, **$p < 0.01$). (C) Histological staining with MTC that demonstrates new bone formation 8 weeks after cell-seeded scaffold delivery (Scale bar = 300 μm). (D) IF images showing DAPI and OPN staining for all groups (Scale bar = 50 μm).

5.8. Conclusions

To function as an active transcription factor, recombinant RUNX2 should be delivered into cells. However, RUNX2 itself could not penetrate the cell membrane. In the present work, the fusion of RUNX2 with 30Kc19α, which contains CPP, was suggested as a solution for resolving this problem. I demonstrated that 30Kc19α enabled the intracellular delivery of RUNX2. Furthermore, RUNX2 was expressed in soluble form through the fusion with 30Kc19α. Direct delivery of RUNX2 into hMSCs permitted RUNX2 to induce osteogenic differentiation *in vitro* and *in vivo*. In conclusion, the intracellular delivery of osteogenic transcription factor by multifunctional CPP, 30Kc19α could be applied to regulate stem cell fate in bone tissue engineering.

Chapter 6

Skin-penetration of recombinant bFGF facilitated by 30Kc19α for enhancement of wound healing

Chapter 6. Skin-penetration of recombinant bFGF facilitated by 30Kc19α for enhancement of wound healing

6.1. Introduction

Basic fibroblast growth factor (bFGF), a member of the fibroblast growth factor (FGF) family, is known for its versatile involvement in tissue growth and regeneration, including wound healing. Activation of FGF receptor by bFGF stimulates intracellular signaling pathways such as phosphoinositide 3-kinase (PI3K)/protein kinase B (Akt) and mitogen-activated protein kinase (MAPK)/extracellular signal-regulated kinase (ERK) signaling pathways which are related to the mitogenic response of cells [119]. As bFGF acts on various target cells involved in wound healing, its effects on wound healing have been extensively studied [120, 121]. bFGF promotes the migration of dermal fibroblasts, keratinocytes, and endothelial cells, into wound sites and facilitates their proliferation [122-126]. As a result, bFGF accelerates granulation tissue formation and angiogenesis, which results in matrix formation and remodeling [127-129].

In recent years, a number of clinical uses of recombinant bFGF have been reported, and these include treatment of chronic wounds, second-degree burns, pressure ulcers, and diabetic foot ulcers [130-132]. However, its inherent instability and rapid degradation often require frequent treatments in tandem with higher concentrations [133-135]. The reported half-life of recombinant bFGF is less than 10 hours under normal cell culture conditions and even shorter in the living organisms, which significantly limits its bioavailability in both *in vitro* and *in vivo* applications [136, 137]. Therefore, molecular biotechnological methods to enhance the stability of the bFGF would improve its clinical use. In earlier studies,

stabilization of bFGF was attempted by introducing mutations or structural modifications to the molecule or by utilizing heparin for bFGF protection [138, 139].

Here I have attempted to solve the problem of recombinant bFGF instability by using the 30Kc19α protein, which is an α-helix domain of 30Kc19. Since silkworm hemolymph exhibited anti-apoptotic effects in various cell systems, 30K protein family members, were isolated from silkworm hemolymph and studied intensively [5, 79-81, 140, 141]. Among them, 30Kc19 received attention for its anti-apoptotic and protein stabilizing effects [6-8]. It was also discovered that 30Kc19 possessed cell- and tissue- penetrating properties by virtue of containing a type of CPP named Pep-c19 [9-11, 142]. In the previous work, it was confirmed that the 30Kc19α retains important functions exhibited by 30Kc19 [85]. 30Kc19α enhanced stability of proteins and provided functional moieties for cell-penetration when it was fused to GFP [14]. Based on these unique properties, Kim investigated whether the fusion of 30Kc19α to bFGF could enhance the stability of bFGF by protecting it from degradation [143]. In addition, it was assessed whether the fusion of 30Kc19α would enable transdermal delivery and/or improve the dermal tissue permeability of bFGF. Finally, it was investigated the tissue-regenerative ability of the fusion protein by applying it to an *in vivo* skin wound model in mice [87]. Data in chapter 7 highlights the potential of using 30Kc19α in tissue regeneration through improving both the stability and tissue penetration of biomolecules.

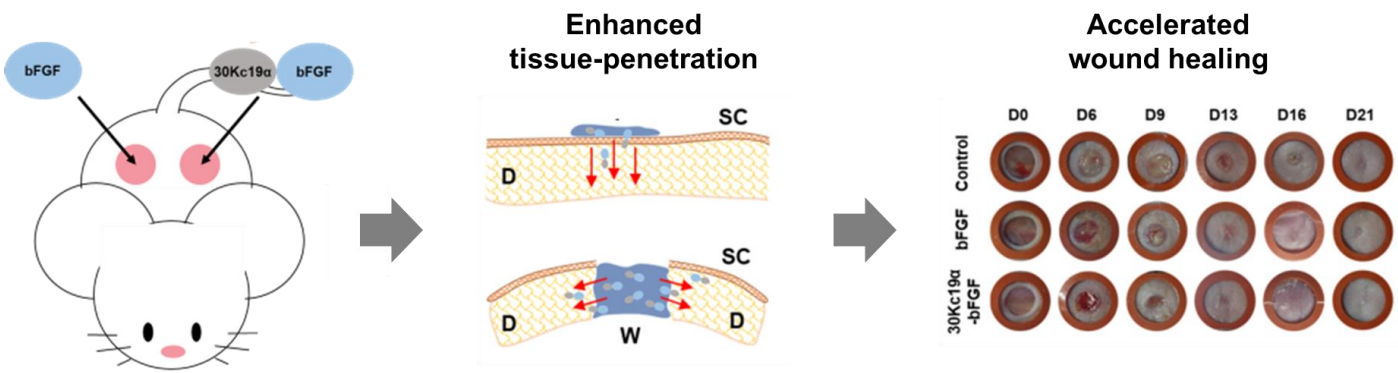

Figure 6.1. A schematic illustration of chapter 6.

6.2. Enhanced protein yield, cell surface deposition, and cell-penetration of recombinant bFGF *via* fusion with 30Kc19α

N-terminal amino acids of bFGF are flexible and not involved in the interaction with FGFR. Therefore, 30Kc19α was fused to the N-terminus of bFGF [144]. To produce recombinant bFGF and 30Kc19α-bFGF, pET-23a/*bFGF* and pET-23a/*30Kc19α-bFGF* were constructed (Figures 6.2A). Recombinant proteins were expressed in *E. coli* and purified by FPLC. Coomassie blue staining and western blot analysis showed that the sizes of purified proteins corresponded to the predicted sizes of bFGF and 30Kc19α-bFGF, which are 17.2 and 27.4 kDa, respectively (Figure 6.2B). Protein yield of bFGF and 30Kc19α-bFGF were 817 and 3394 μg/L culture, respectively. When calculated by moles, the protein yield of bFGF increased by 2.61 times when 30Kc19α was fused.

Prior to treating cells with recombinant proteins, LIVE/DEAD viability assay and cytotoxicity assay were performed to test their cytotoxicity. A similar number of red fluorescence (ethidium homodimer-1; EthD-1) was observed in the three groups and the cell viability of both bFGF- and 30Kc19α-bFGF-treated HDFs were nearly 100% compared to the control group, indicating non-cytotoxic features of the recombinant proteins (Figures 6.3A, B).

Since the 30Kc19α has been previously reported to exhibit cell-penetrating abilities, intracellular translocation of 30Kc19α-bFGF was visualized *via* CLSM after IF staining and compared to that seen with bFGF (Figure 6.3C). Equimolar recombinant bFGF and 30Kc19α-bFGF proteins were applied to HDFs for 4 hours, followed by fixation and ICC staining with anti-T7 tag antibody. The green-fluorescent T7 tag was observed in bFGF and 30Kc19α-bFGF-treated groups;

however, the 30Kc19α-bFGF-treated group showed higher fluorescence on both the cell surface and in the cytosol of HDFs than the bFGF-treated group. This suggests that the fusion of 30Kc19α to bFGF enhanced cellular uptake of bFGF.

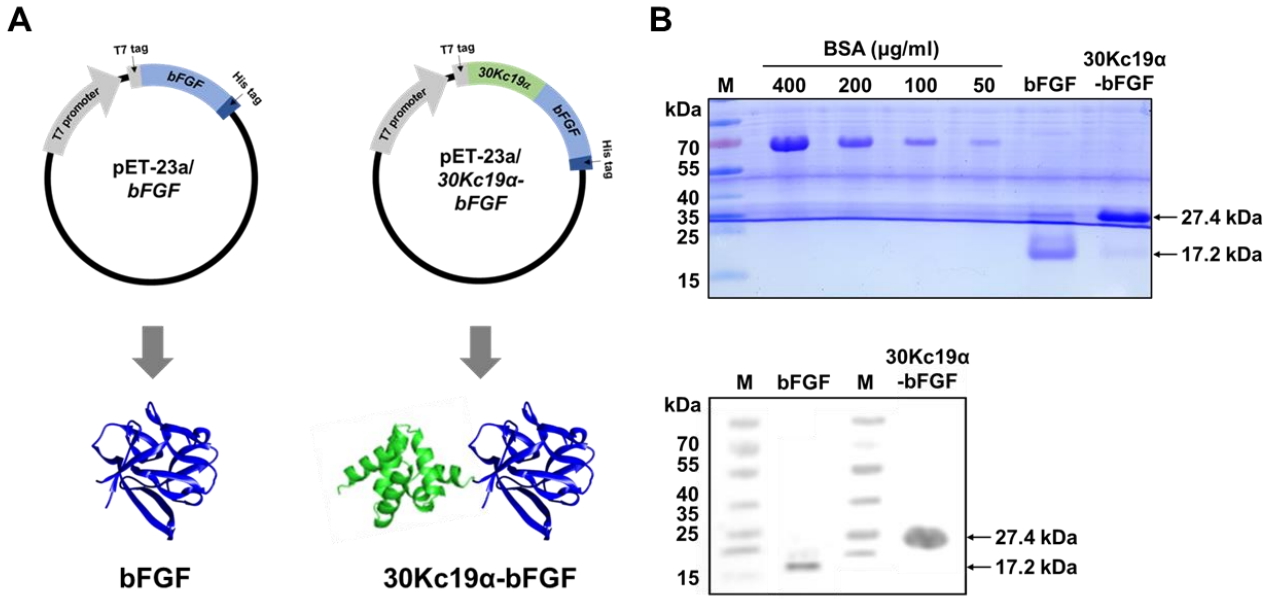

Figure 6.2. Fusion of 30Kc19α to bFGF. (A) Plasmid construction of pET-23a/*bFGF* and pET-23a/*30Kc19α-bFGF* and protein structure of bFGF and 30Kc19α-bFGF. Protein structure was visualized by Chimera software. (B) Coomassie blue staining and western blot analysis of recombinant bFGF and 30Kc19α-bFGF. Anti-T7 tag antibody was used as primary antibody for purified recombinant proteins. M, marker.

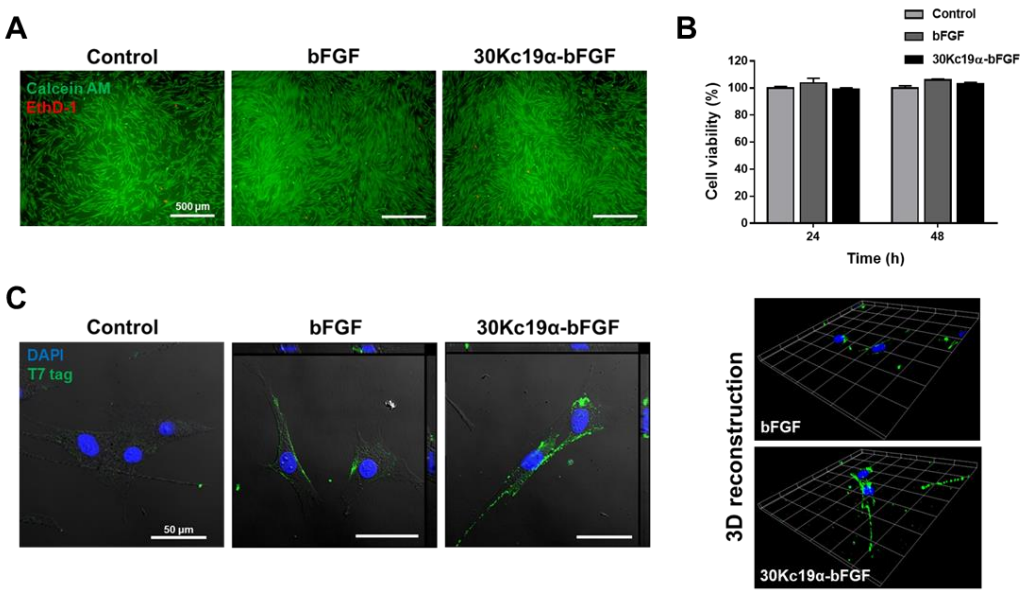

Figure 6.3. Low cytotoxicity and cell-penetration ability of 30Kc19α-bFGF. (A) LIVE/DEAD viability assay and (B) cytotoxicity assay. Human dermal fibroblasts (HDFs) were treated with 4 μM of the proteins for 24 and 48 hours. Live and dead cells from 48 hour treated samples were stained with green and red fluorescence respectively (Scale bar = 500 μm). Cytotoxicity assay was done for both 24 and 48 hour treated samples. Data are expressed as relative cell viability normalized to the control group (n = 4). (E) Confocal image with orthogonal projection (left) and 3D recostruction of z-stack images (right) of bFGF- and 30Kc19α-bFGF-treated HDFs. HDFs were treated with 4 μM of the proteins for 1 hour. The proteins were labeled with Alexa Fluro® 488, and the nucleus with DAPI (Scale bar = 50 μm).

6.3. Improved angiogenic ability of HUVECs through 30Kc19α-bFGF treatment

Exogenous delivery of bFGF has proven to enhance the angiogenesis during wound repair despite its low accumulation at wound sites [145, 146]. It was investigated whether the enhanced stability and cellular interaction of 30Kc19α-bFGF could improve the angiogenic ability *in vitro* using HUVECs. The HUVECs treated with 30Kc19α-bFGF showed improved angiogenic performance, which exhibited both higher tube formation and branching points (Figure 6.4A). The quantitative analysis represented that 30Kc19α-bFGF significantly supported the tube formation ability of HUVECs than bFGF, and the cells treated with 30Kc19α-bFGF displayed larger numbers of branching points than bFGF (Figures 6.4B, C). This indicates that 30Kc19α protein can improve the angiogenic functionality of bFGF *in vitro* and 30Kc19α-bFGF has the potential to improve the neovascularization during the wound healing process.

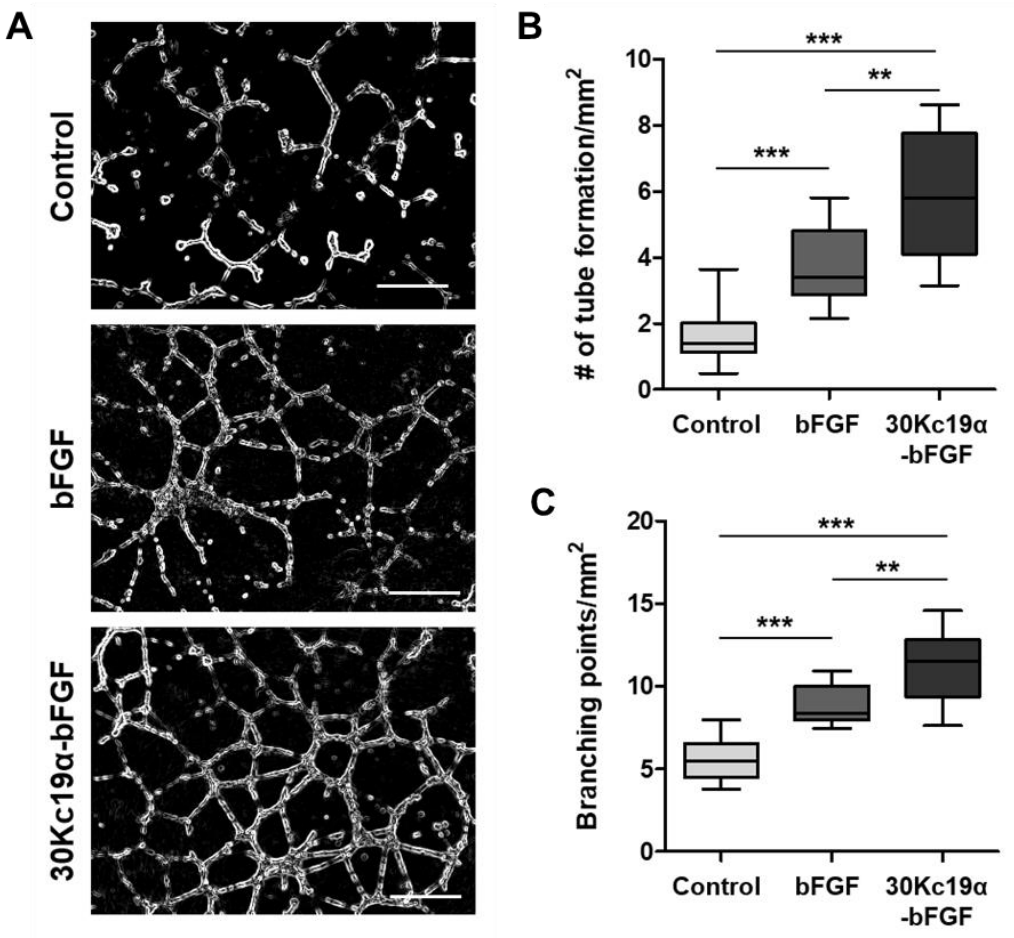

Figure 6.4. *In vitro* angiogenic effects of 30Kc19α-bFGF on HUVECs. (A) Human umbilical vein endothelial cells (HUVECs) formed vasculatures on Matrigel when treated with 4 μM of the proteins for 12 hours (Scale bar = 500 μm). Angiogenic effects of 30Kc19α-bFGF were analyzed by measuring (B) the number of tube formation and (C) the count of branching points per unit area based on the microscopic images (**$p < 0.01$ and ***$p < 0.001$).

6.4. *In vivo* transdermal transport of NIR fluorophore through conjugation with 30Kc19α

Among cell membrane-penetrating peptides, some kinds display effective skin-penetrating ability by destabilizing the stratum corneum (SC) and/or by micropinocytosis [147]. Given that 30Kc19α contains a cell-penetrating moiety named Pep-c19, it was assessed whether the 30Kc19α can penetrate the SC by modifying it with near-infrared (NIR) dye, ZW800-1C, for direct visualization when applied on hairless mouse skin [10, 148]. Initially, NHS-ester-containing ZW800-1C was conjugated to the amine group in 30Kc19α, followed by formulating with carbomer gel that could be observed under NIR fluorescent microscopy (Figure 6.5A). The samples were applied into the silicone adhesive isolators, washed off and imaged after 4 hours. In the magnified images, ZW800-1C alone exhibited much weaker fluorescent signals than the 30Kc19α conjugated form (Figure 6.5B). Image quantification showed that ZW800-1C-30Kc19α had a 3.7-fold higher fluorescent intensity compared to ZW800-1C (Figure 6.5C). This result shows that 30Kc19α enhanced the skin permeability of small molecules and exhibited potency as a skin-penetrating protein.

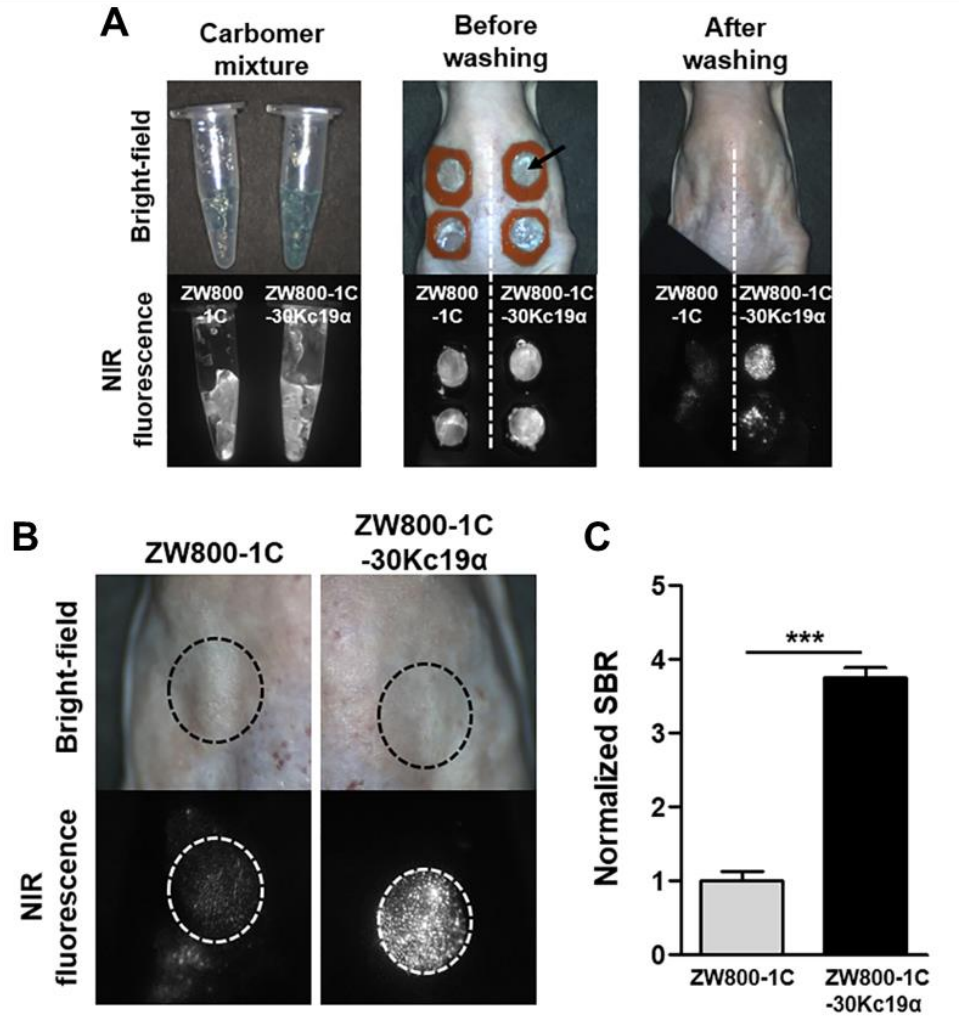

Figure 6.5. *In vivo* skin-penetration ability of 30Kc19α using NIR Fluorophore. (A) ZW800-1C-30Kc19α conjugate was prepared and applied to the dorsal skin of hairless mice. Images were obtained with FLARE imaging system. (B) Magnified images after washing showed that the ZW800-1C-30Kc19α could penetrate the SC effectively. (C) The fluorescent signal was quantified based on the magnified images, and the normalized signal-to-background ratio (SBR) in ZW800-1C-30Kc19α was significantly higher than that of ZW800-1C, suggesting that 30Kc19α improves the skin-penetration ability of small molecules (n = 3, ***$p < 0.001$).

6.5. Facilitated transdermal delivery and dermal tissue-penetration of bFGF *via* fusion with 30Kc19α

It is still challenging to deliver therapeutic proteins by transdermal route, but transdermal- or dermal delivery is a promising technique for facile administration and can promote the wound healing process [149]. After verifying the skin permeability of 30Kc19α using the NIR probe, it was determined whether 30Kc19α can deliver bFGF protein transdermally. When applied to hairless mouse skin *in vivo*, the proteins were observed by IF staining on both intact skin and in an open wound (Figure 6.6). 30Kc19α-bFGF indicated strong fluorescent signals at the SC, while bFGF showed slight deposition at the SC. However, any penetrant proteins into the dermis layer were not observed in neither group (Figure 6.6A). In the situation with an open wound, it was found that 30Kc19α-bFGF penetrated the dermis layers where the fluorescent signals could be observed between DAPI stains, but there was a little fluorescent signal from bFGF (Figures 6.6B, C). Since it was difficult to stain bFGF in unsectioned tissues, GFP-30Kc19α instead of 30Kc19α-bFGF was applied to the wound site to orthogonally observe tissue penetration *via* CLSM. GFP is a 26.9 kDa protein which exhibits green fluorescence when exposed to blue light. The data showed that a significantly high level of GFP was accumulated into the skin tissue when fused to 30Kc19α (Figure 6.7). It suggests that the 30Kc19α could enhance the dermal tissue penetration of bFGF, but the transdermal delivery of 30Kc19α-bFGF was restricted in hairless mice skin.

To further investigate, the tests were carried out using *ex vivo* porcine skin (Figure 6.8). In the transdermal delivery test, it was hypothesized that the existence of the hair follicles might promote the transdermal delivery of 30Kc19α-bFGF. As a

result, 30Kc19α-bFGF group was observed in the epidermis layer of the skin. On the other hand, the bFGF was shown just in the SC, which indicated 30Kc19α-bFGF could penetrate the intact skin in the existence of hair follicles. Furthermore, at the open wound, 30Kc19α-bFGF exhibited much higher tissue penetration than bFGF alone. The results showed that 30Kc19α could improve not only the transdermal delivery of bFGF through the follicular route but also by dermal tissue penetration.

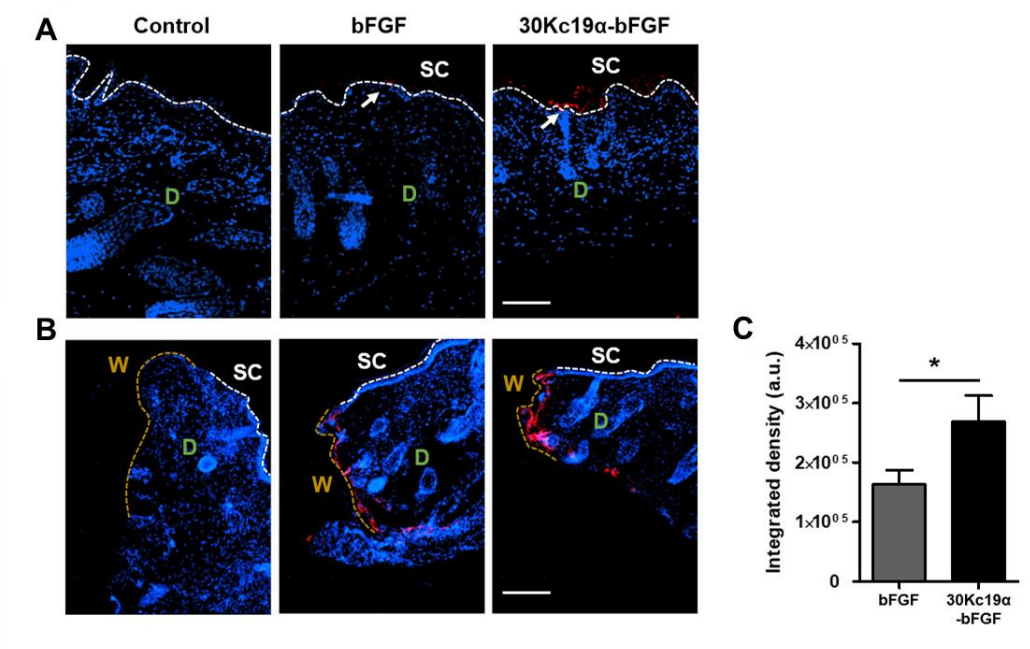

Figure 6.6. *In vivo* transdermal delivery and dermal tissue-penetration ability of 30Kc19α-bFGF. The transdermal and dermal tissue-penetration of 30Kc19α-bFGF on hairless mouse skin was visualized by IF staining at 4 hours after application. (A) intact skin and (B) open wound cases. 30Kc19α-bFGF exhibited more significant accumulation in the skin tissue than bFGF. (C) The integrated density was measured based on the fluorescent signal in the open wound (Scale bar = 100 μm, *$p < 0.01$).

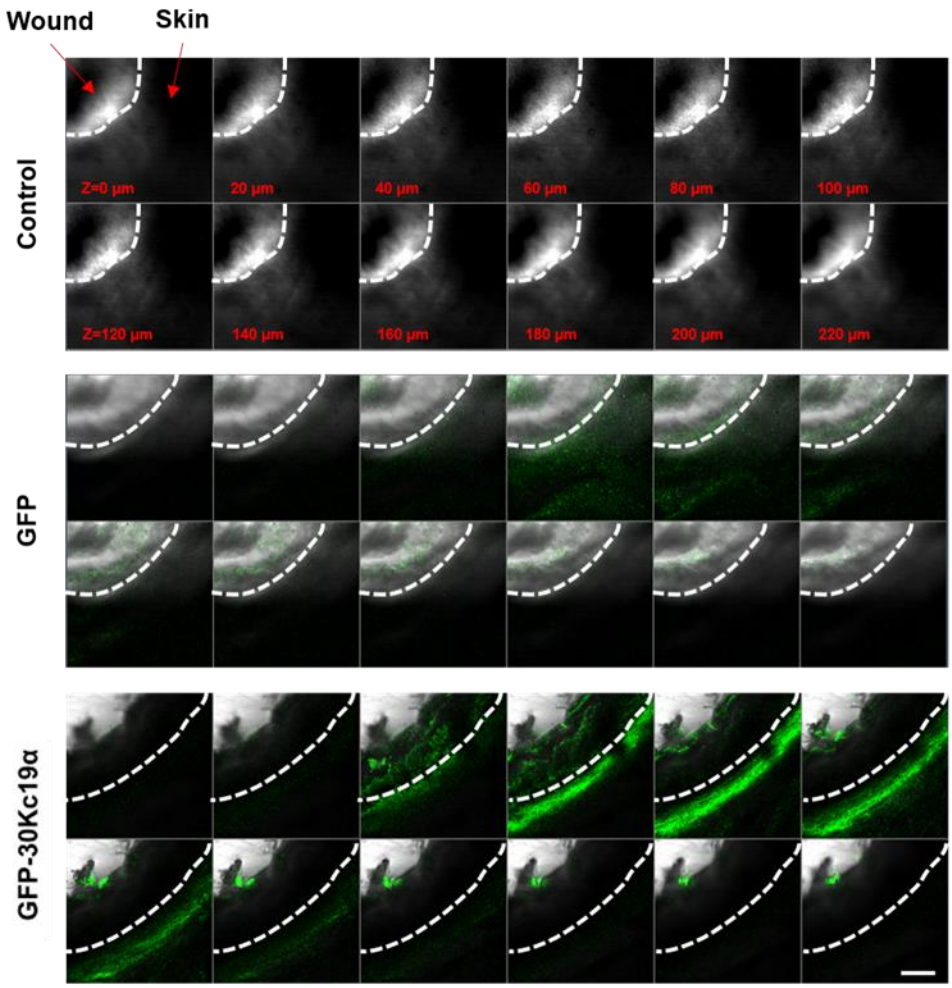

Figure 6.7. *In vivo* skin-penetration of GFP-30Kc19α. The *in vivo* skin tissue penetration ability of 30Kc19α was assessed by fusing it with a green-fluorescent protein (GFP). CLSM images showed that GFP-30Kc19α was highly accumulated into the skin tissue, while only GFP showed a low penetration (white dotted line: a boundary between the wound and the skin, lower z-slice was toward to subcutaneous regions and higher z-slice to the epidermis) (Scale bar = 200 μm).

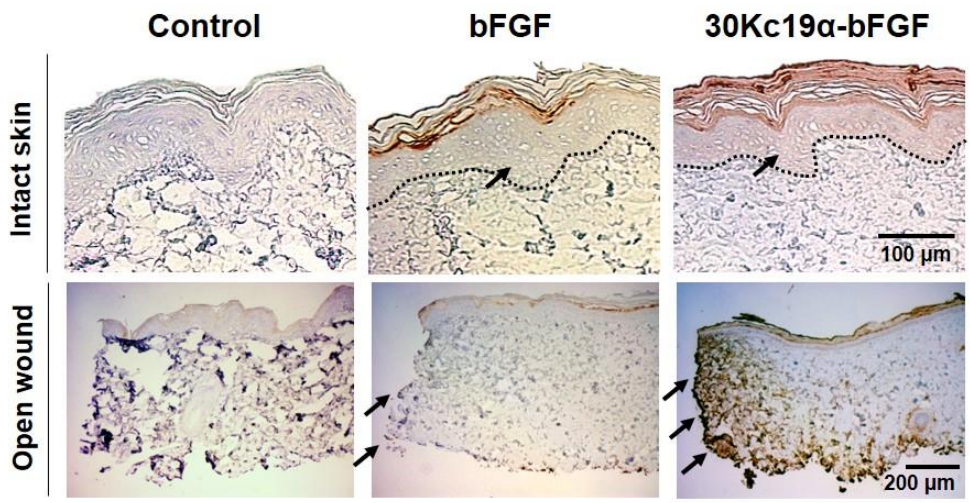

Figure 6.8. *Ex vivo* penetration ability of 30Kc19α-bFGF into the dermal layer of porcine skin. The transdermal delivery of 30Kc19α-bFGF was confirmed by T7 tag staining at 4 hours after application. 30Kc19α-bFGF was found in both the SC and epidermal layer (upper portion of black dashed line), while in the case of bFGF, less protein was accumulated in the SC, and there was no penetrance of signal into the epidermal layer. The dermal tissue penetration ability of 30Kc19α-bFGF was also evaluated by applying protein gels to the wound. The wound tissues were stained for T7 tag (black arrow) after 2 hours, which showed 30Kc19α-bFGF could effectively penetrate into the dermal layer.

6.6. Accelerated wound healing effect of 30Kc19α-bFGF by stimulating cell proliferation

The wound healing effect of 30Kc19α-bFGF was evaluated in the mouse wound model. Carbomer gel was used to retain the samples at the wound site, and PBS-loaded carbomer gel was used as a control group. In the macroscopic analysis, 30Kc19α-bFGF effectively promoted wound regeneration from day 6, and the wound size was significantly reduced on day 8 (Figures 6.9A, B). These regenerative profiles were supported by IF image of Ki67 on day 6. The highest number of proliferative cells were seen with 30Kc19α-bFGF (Figures 6.9C, D). In particular, strong Ki67 signals could be observed in epidermal regions. As a result, it was confirmed that the 30Kc19α-bFGF effectively enhanced the wound healing rate at the macroscopic scale.

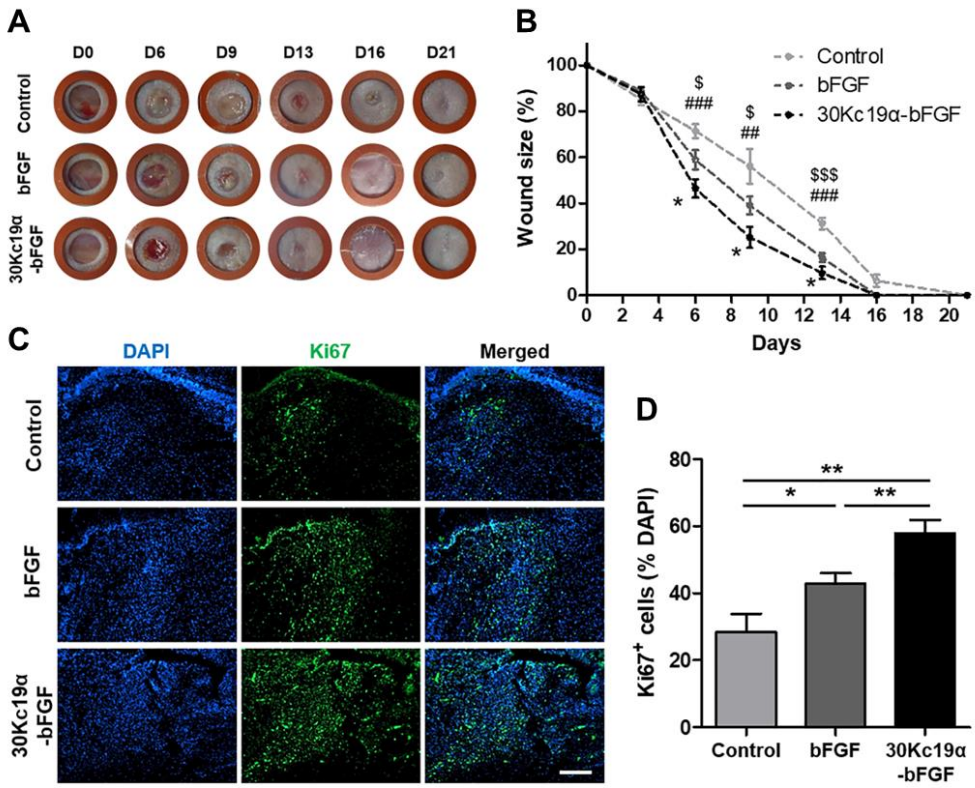

Figure 6.9. *In vivo* wound healing application of 30Kc19α-bFGF. (A) Photographs of the wound up to 21 days. (B) The wound size-reduction profile was calculated based on the photographs. 30Kc19α-bFGF significantly promoted wound healing compared to bFGF (Statistical significance: * represents 30Kc19α-bFGF to bFGF; # represents 30Kc19α-bFGF to control; and $ represents bFGF to control. $^{*,\$}p<0.05$, $^{\#\#}p<0.01$, and $^{\#\#\#,\$\$\$}p<0.001$). (C, D) Proliferative cells in the wound bed were estimated by IF image of Ki67 (green) on day 6, and quantitatively analyzed based on the fluorescent signals. (Scale bar = 200 μm, $*p < 0.05$ and $**p < 0.01$).

6.7. Promoting *in vivo* wound regeneration, collagen deposition, and angiogenesis effect of 30Kc19α-bFGF

The tissue formation and remodeling processes are a critical phase during wound healing, which can determine the quality of the rehabilitated skin, and bFGF is involved in several biological responses, such as collagen deposition and angiogenesis [150]. Thus, the regenerative capability of 30Kc19α-bFGF was qualitatively assessed from the histological analysis. H&E-stained images of the cross-sectioned tissues were observed, and the panniculus gap, which is the distance between newly formed panniculus adiposus at wound edges, was measured. On day 14, both the bFGF and 30Kc19α-bFGF groups showed greater wound healing ability compared to control, but 30Kc19α-bFGF had the narrowest panniculus gap (Figure 6.10A). On day 21, with 30Kc19α-bFGF treatment, the tissue was being regenerated in the form of a native tissue-resembling structure with a significantly decreased panniculus gap and newly formed appendages (Figure 6.10B). Specifically, the panniculus gap was further decreased below 100 μm in 30Kc19α-bFGF, whose value was substantially lower than that of both control and bFGF.

Next, collagen deposition was analyzed from MTC-stained images. The granulation tissue area of bFGF and 30Kc19α-bFGF were 1.8- and 2.3-fold more substantial than the control group; that is, 30Kc19α-bFGF effectively promoted tissue granulation during wound healing better than bFGF (Figure 6.11A). From day 14, the skin appendages were being formed and regenerated from the epidermal layer, and there were more as well as better matured appendages observed in 30Kc19α-bFGF than bFGF. On day 21, the magnified MTC images showed that 30Kc19α-bFGF accelerated much higher collagen deposition and the formation of the skin

appendages, such as hair follicles, compared to control and unconjugated bFGF (Figure 6.11B). In addition, the organization of ECM fiber alignment was measured at the dermal layer. The lower coherence of 30Kc19α-bFGF indicated that the wound was being regenerated toward something more resembling healthy skin tissue. This will be discussed in the following section.

Finally, the angiogenic ability of 30Kc19α-bFGF was evaluated. The skin tissues were stained for α-SMA on day 14. Based on the HPF images in the regenerated regions, the highest number of newly formed blood vessels were observed in 30Kc19α-bFGF (Figure 6.12). More specifically, 30Kc19α-bFGF had a 2.6- and a 1.4-fold higher number of vessels than that of control and bFGF, respectively. Furthermore, it was shown that the vessels in 30Kc19α-bFGF increased not only in number but they were also more stretched and had an enlarged shape compared to bFGF.

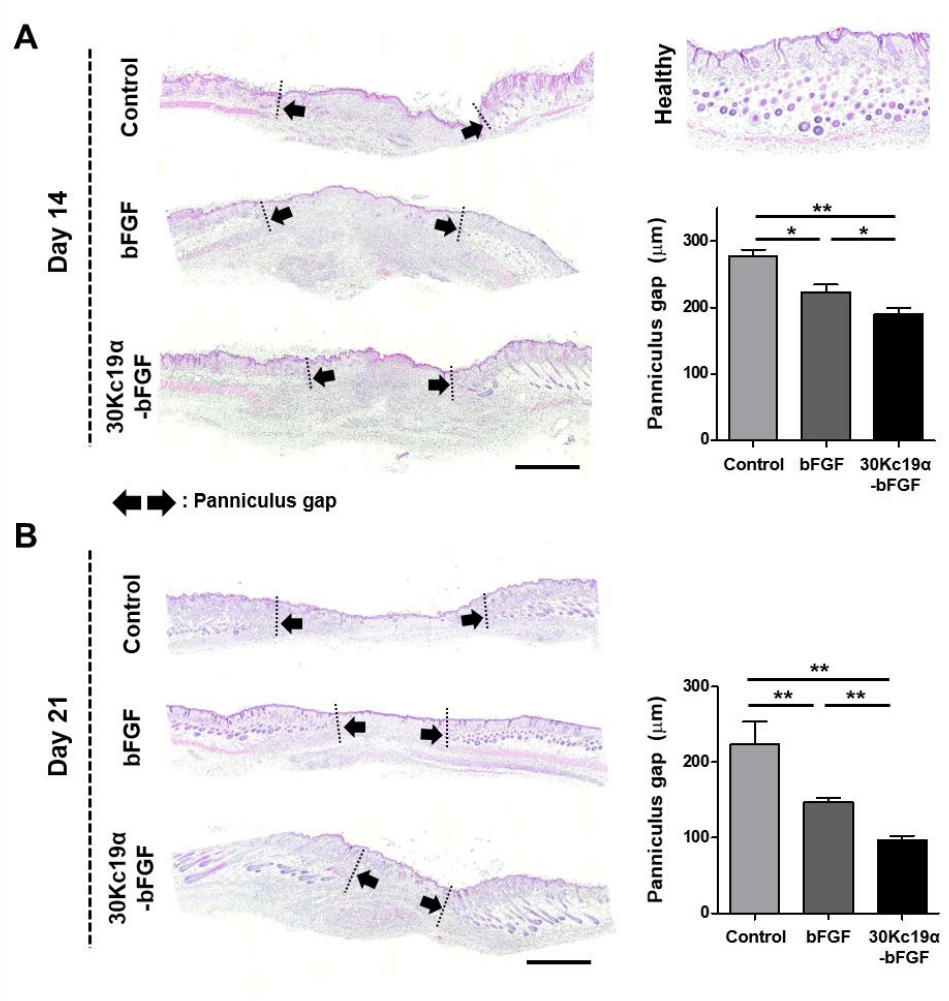

Figure 6.10. Histological and qualitative analysis based on H&E staining. Panniculus gap was quantified on day 14 (A) and day 21 (B). It was revealed that 30Kc19α-bFGF accelerated wound regeneration *via* tissue granulation process. Although the panniculus gap of all groups continuously decreased, it was notably reduced with 30Kc19α-bFGF, whose tissue was being recovered at the fastest rate with a structure similar to healthy tissue (Scale bar = 1 mm, *$p < 0.05$ and **$p < 0.01$).

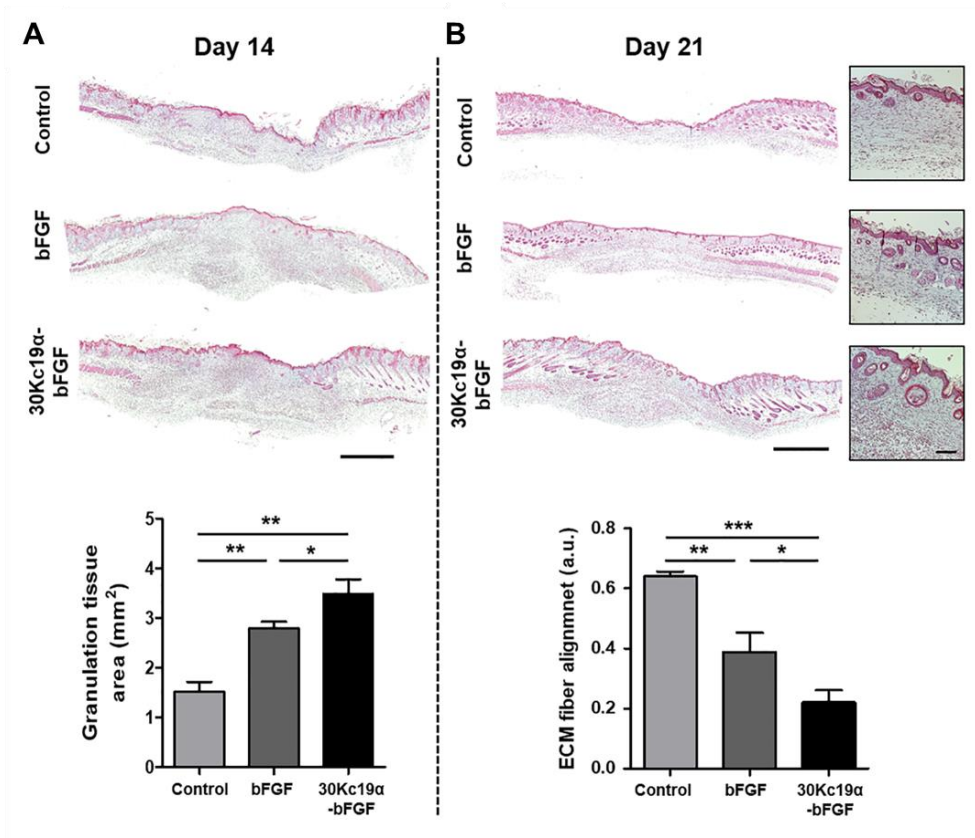

Figure 6.11. Histological and qualitative analysis based on MTC staining. Tissue granulation and the degree of ECM fiber alignment were analyzed by MTC staining of the skin tissue on day 14 (A) and day 21 (B), respectively. It was confirmed that 30Kc19α-bFGF supported tissue granulation during the proliferative phase of the wound healing process. Also, both collagen deposition and the formation of skin appendages were enhanced in 30Kc19α-bFGF on day 21. The organization of ECM fiber alignment was quantified at the dermis layer, where the value represents its coherence. 30Kc19α-bFGF exhibited better results all round (Scale bar = 1 mm and 100 μm in low and high magnified images, respectively, *$p < 0.05$, **$p < 0.01$, and ***$p < 0.001$).

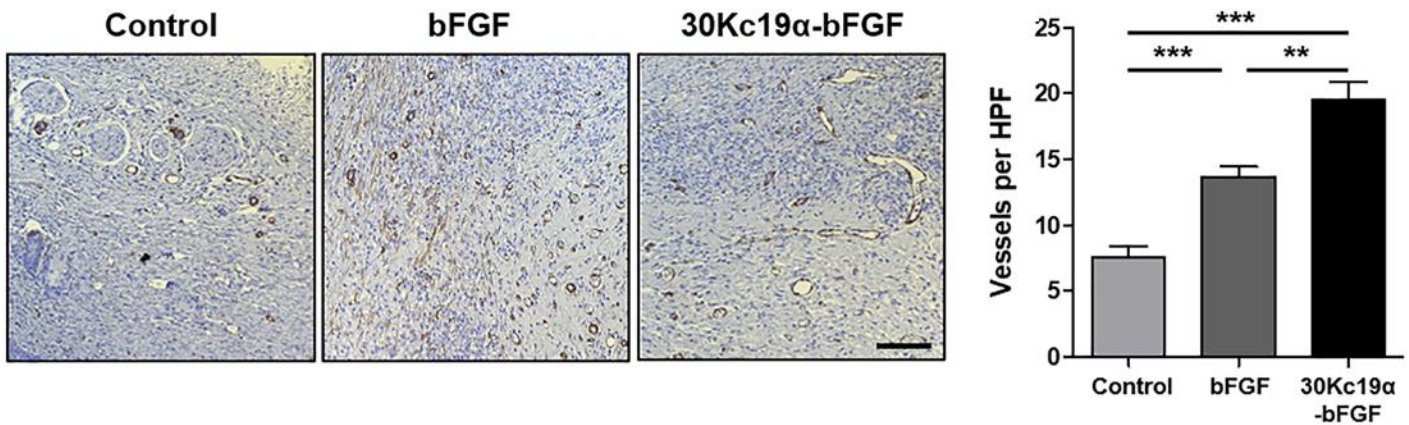

Figure 6.12. *In vivo* angiogenic ability of 30Kc19α-bFGF. (A) Immunohistochemistry staining of alpha-smooth muscle actin (α-SMA) on day 14 and (B) its quantitative analysis. 30Kc19α-bFGF improved angiogenesis during wound healing compared to control and bFGF and newly formed vessels had enlarged and stretched structures (Scale bar = 100 μm, $^{**}p<0.01$ and $^{***}p<0.001$).

6.8. Conclusions

30Kc19α was fused to bFGF to overcome the instability problem of recombinant bFGF. The results indicate that 30Kc19α-bFGF has more stable characteristics than bFGF. Prolonging the biological activities of bFGF resulted in improved wound healing effects in HDFs and HUVECs. The skin-penetration ability of 30Kc19α was verified using an NIR fluorophore *in vivo*, and the 30Kc19α-bFGF also showed improved accumulation on the skin and exhibited higher transdermal translocation through follicular routes than bFGF. When applied to an *in vivo* wound model, 30Kc19α-bFGF showed excellent skin tissue regeneration, which could be achieved *via* enhanced stability and facilitated dermal tissue penetration. Therefore, 30Kc19α-bFGF would be a useful wound healing material in therapeutic applications.

Chapter 7

Linking two 30Kc19α monomers using a flexible linker for efficient dimerization and cell-penetration of 30Kc19α

Chapter 7. Linking two 30Kc19α monomers using a flexible linker for efficient dimerization and cell-penetration of 30Kc19α

7.1. Introduction

When a non-cell-permeable biomolecule is effectively delivered into cells, it is possible to develop new drugs for intracellular disease targets. Particularly, antibodies have high target specificity and low immunogenicity so that they are utilized as drugs by themselves or conjugated to drugs in pharmaceutical fields. However, most antibodies could only target extracellular targets due to their inability to penetrate the cell membrane. Therefore, the methods for intracellular delivery of antibodies have been developed [151]. Shin *et al*. have developed antibody which has target cell–specific penetrating ability. It targets intracellular RAS protein, which is an important cell growth and differentiation regulator and one of the most frequently mutated oncogenes in humans [152]. In other research groups, CPPs have been utilized for intracellular delivery of antibodies. CPP or CPP-multimers were conjugated to antibody for intracellular delivery of IgG antibodies [153-155].

30Kc19 is a protein originating from silkworm hemolymph, with a cell-penetrating property. It has been utilized for intracellular delivery of various cargo proteins including transcription factors. The underlying mechanism of cell-penetration of 30Kc19 has been suggested as endocytosis, especially macropinocytosis and caveolin-mediated endocytosis [142]. It also has been discovered that 30Kc19 tends to dimerize on the cell membrane surface and that the dimerization is essential for cell-penetration. When the 57th cysteine of 30Kc19 was replaced with an alanine residue, 30Kc19 lost its cell permeability. This suggests that

the dimerization is important in cell-penetration ability of 30Kc19. 30Kc19α, the α-helix domain of 30Kc19, is smaller in size and has higher cell-penetrating efficiency than 30Kc19. From now on, 30Kc19 or 30Kc19α have been utilized to intracellular cargo delivery of biomolecules much smaller than IgG antibodies (~150 kDa). In addition, these proteins have been applied to *in vitro* environments or *in vivo* local areas. For large cargo biomolecule delivery or *in vivo* system delivery, the likelihood of dimer formation could be greatly reduced.

Herein, I developed 30Kc19α-Linker-30Kc19α cell-penetrating protein by linking two 30Kc19α monomers with a peptide linker to increase dimerization efficiency, thereby improving cell-penetration. First, it was confirmed whether 30Kc19α also showed similar dimerization properties as 30Kc19. Optimization of the peptide linker was preceded. After that, it was confirmed that 30Kc19α-Linker-30Kc19α delivered the cargo protein, GFP into cells with higher efficiency than the conventional 30Kc19α. Therefore, I propose that 30Kc19α-Linker-30Kc19α would be applied to intracellular drug delivery in pharmaceutical fields.

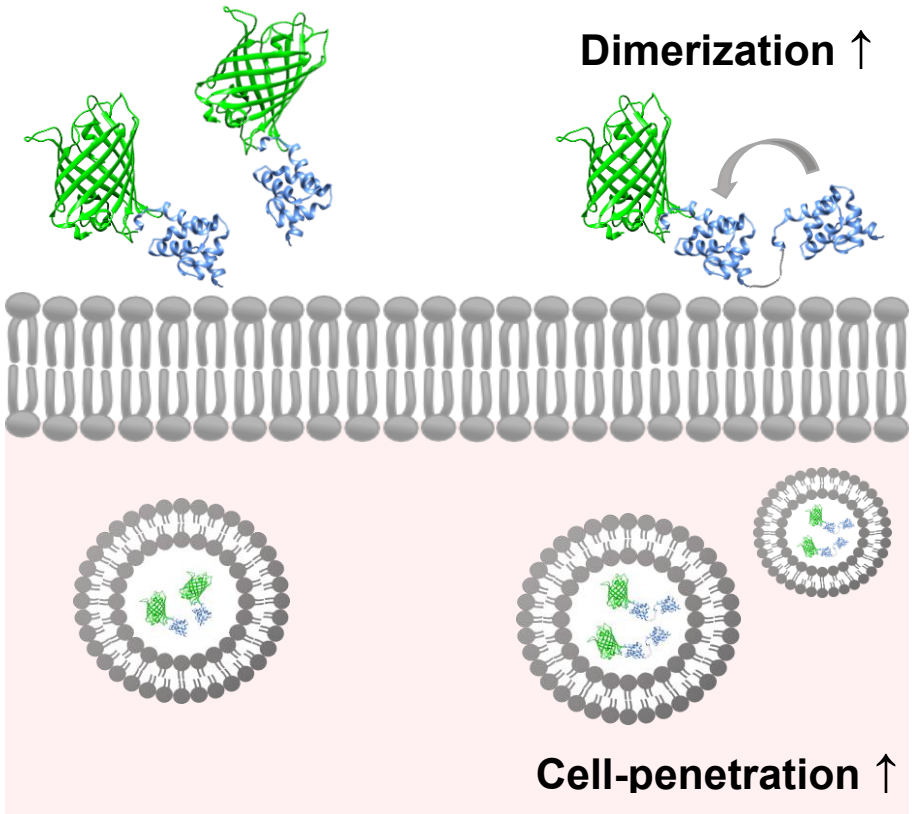

Figure 7.1. A schematic illustration of chapter 7.

7.2. Dimerization of 30Kc19α and its importance on cell-penetration

In a previous study, it was confirmed through native PAGE that 30Kc19 forms a dimer when SDS with a structure similar to phospholipid, a cell membrane component, exists. To figure out whether 30Kc19α also forms dimer in the presence of SDS, 30Kc19α was mixed with SDS. Then, the mixture was loaded onto native gels. The gel data showed that 30Kc19α existed as a monomer in the absence of SDS and gradually formed dimers in the presence of SDS (Figure 7.2A). Although some monomers without dimerization remained, the dimer bands tended to thicken as the concentration of SDS increased from 0% to 2%. Next, it was confirmed whether dimerization was important for the cell-penetration ability of 30Kc19α. In the previous study, the 57th cysteine was found to be involved in the dimerization of 30Kc19. 30Kc19α consists of 1-88 aa of 30Kc19, so it also contains the 57th cysteine. To prevent dimerization, the 57th cysteine was substituted with alanine through point mutation. Then, 30Kc19α and 30Kc19α C57A were produced in *E. coli*. The recombinant proteins were identified by Coomassie blue staining and western blot. 30Kc19α C57A was located in the slightly below the gel compared to 30Kc19α (Figure 7.2B). When HeLa cells were treated with recombinant proteins, there was little cytotoxicity even at a concentration of 10 μM (Figure 7.2C). After cytotoxicity assay, HeLa cells were treated with 10 μM of proteins for 1 hour and ICC staining was performed. Green fluorescence was not observed for the mutant 30Kc19α compared to the existing protein. When 57th cysteine, which is responsible for dimerization of 30Kc19α, was substituted alanine, the cell-penetrating ability was dramatically diminished (Figure 7.2D). Similar results to 30Kc19 suggests that

30Kc19α also forms a dimer in the cell membrane, and dimerization is important in cell permeation.

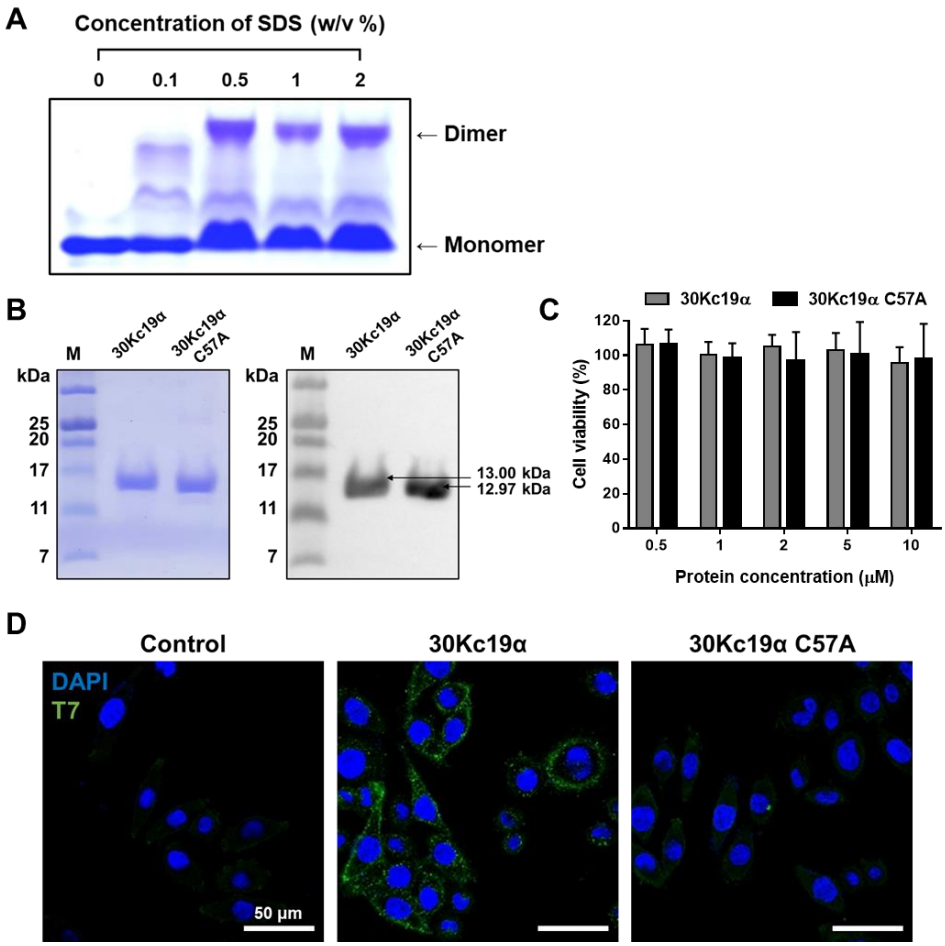

Figure 7.2. Dimerization tendency of 30Kc19α in the presence of SDS and the importance of Cys57 in the cell-penetrating ability of 30Kc19α. (A) Native PAGE gel showing dimerization tendency of 30Kc19α in the presence of SDS. (B) Coomassie blue staining and western blot data of 30Kc19α and 30Kc19α C57A. Anti-T7 tag antibody was used as a primary antibody. (C) Cytotoxicity assay using CELLOMAX™ cell viability assay. HeLa cells were treated with various concentrations of proteins for 24 hours. The cell viability was normalized to the control group. (D) Confocal images of 30Kc19α- or 30Kc19α C57A-treated cells. HeLa cells were treated with 10 μM of the proteins for 1 hour. T7-tagged recombinant proteins were stained with Alexa Fluro® 488, and the nucleus with DAPI (Scale bar = 50 μm).

7.3. Development of 30Kc19α-Linker-30Kc19α

Since the importance of dimerization in the cell-penetration of 30Kc19α was confirmed, 30Kc19α-Linker-30Kc19α was designed in which two 30Kc19α monomers were linked together using a peptide linker. Before design, the homo-dimeric structure of 30Kc19α was predicted by protein-protein docking calculations. Briefly, seven thousands of dimer shapes were predicted and the clusters based on the structural shapes were generated. Among the generated clusters, ten with stable energy were selected for final candidates. Structural optimization and energy measurement were then performed using the Prime module from the Schrödinger suites. Finally, four dimer structures were proposed in rank order. According to Figure 7.3, the distance between the C-terminus of the first 30Kc19α and the N-terminus of the second 30Kc19α was not that close. Therefore, the need for connecting them with a flexible and long linker was identified. Through this, the probability of dimerization would be increased.

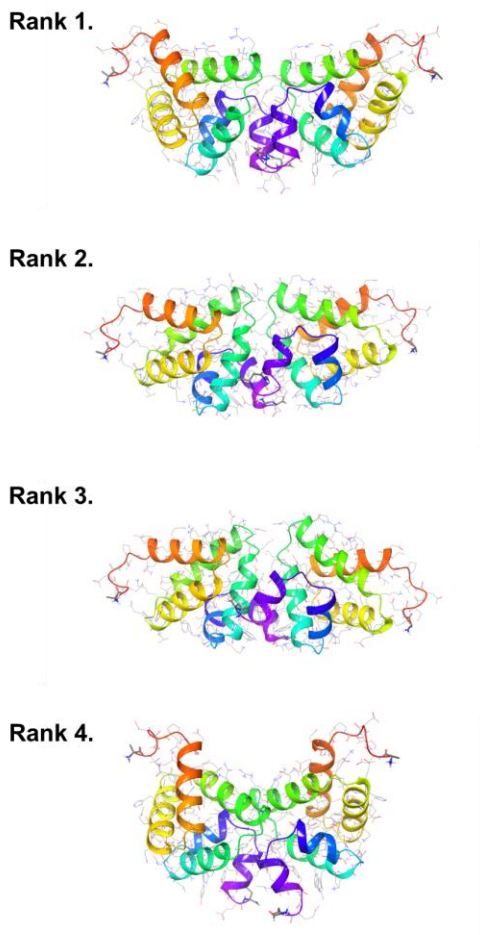

Figure 7.3. Homo-dimeric structure prediction of 30Kc19α. Among 7000 homodimer samplings, four dimer structures were proposed in rank order. Dimer optimization and energy evaluation was performed using Prime structure optimization tool from Schrödinger suite modules.

7.4. Linker optimization for 30Kc19α-Linker-30Kc19α

Optimization of the peptide linker was performed to determine the optimal linker for effective dimerization and cell-penetration. Various lengths of flexible linkers (G2S3 linkers of varying lengths from 5 to 50 aa) and 20 aa rigid linker ((EAAAK)4) were selected as candidates for linking two 30Kc19α monomers (Table 7.1). Then, turboGFP (hereinafter simply referred to as GFP) was selected as the cargo protein for quantification of cell-penetration. GFP was fused to N-terminus of the cell-penetrating proteins (Figure 7.4A). GFP alone, GFP-30Kc19α, GFP-30Kc19α-30Kc19α (linkerless group) were added for comparison with linker groups. Prior to the cell-penetration assay, ten types of proteins including GFP were produced in *E. coli*. Recombinant proteins were loaded onto the SDS-PAGE gel and identified by Coomassie blue staining (Figure 7.4B). Proteins bands appeared on the gel at positions corresponding to the expected size. After treating the cells with 1 μM of GFP-fused cell-penetrating proteins for 1 hour, the remnant proteins were removed from the medium and cell membrane through washing and TE treatment. Then, the fluorescence intensity of proteins located in the cells was measured using a microplate reader (Tecan). It was found that 20 aa flexible linker was an optimal linker for 30Kc19α-Linker-30Kc19α (Figure 7.4C). Compared with GFP-30Kc19α -treated group, the fluorescence intensity was increased in all groups except the linkerless group. Especially, it was increased 6.48-fold in GFP-30Kc19α-L20-30Kc19α, which means that 30Kc19α-L20-30Kc19α has higher intracellular delivery efficiency compared to 30Kc19α.

Table 7.1. Amino acid sequences of linkers used for linker optimization.

Linker	Amino acid sequence
L5	GGSSS
L10	GGSSSGGSSS
L20	GGSSSGGSSSGGSSSGGSSS
L30	GGSSSGGSSSGGSSSGGSSSGGSSSGGSSS
L40	GGSSSGGSSSGGSSSGGSSSGGSSSGGSSSGGSSSGGSSS
L50	GGSSSGGSSSGGSSSGGSSSGGSSSGGSSSGGSSSGGSSSGGSSSGGSSS
Rig L20	EAAAKEAAAKEAAAKEAAAKEAAAK

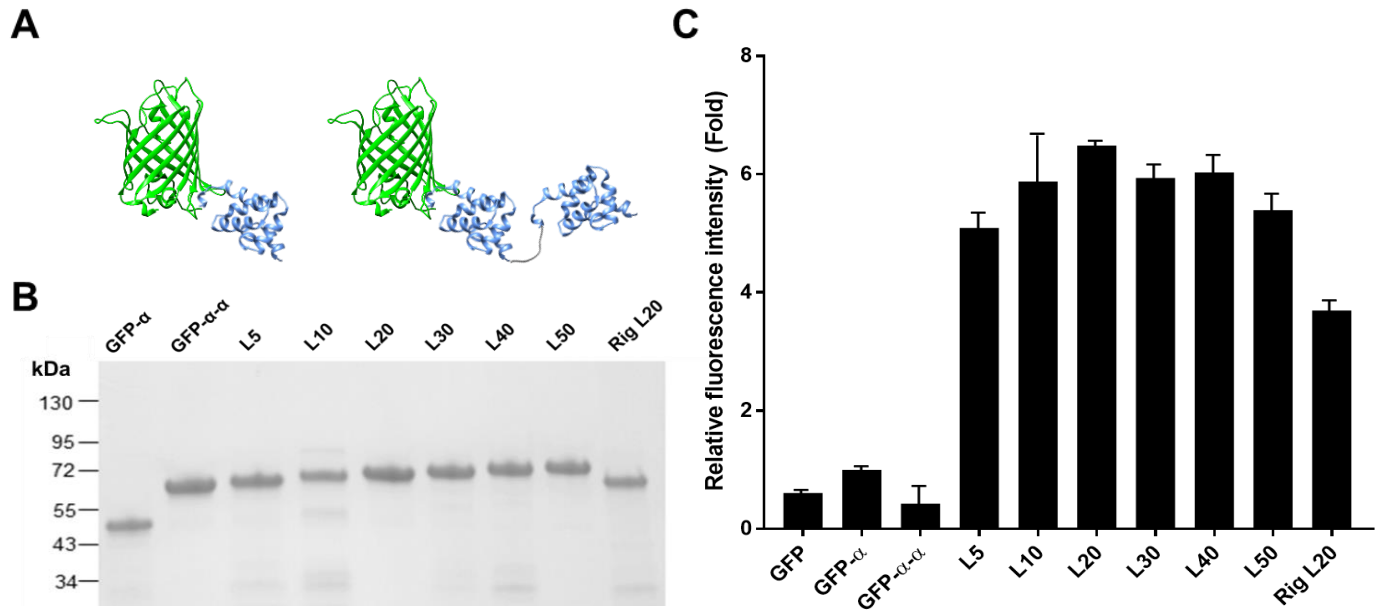

Figure 7.4. Optimization of linker for 30Kc19α-Linker-30Kc19α. (B) Production and identification of recombinant cell-penetrating proteins. Coomassie blue staining was performed for protein identification. α: 30Kc19α; LX: GFP-30Kc19α-X aa flexible linker-30Kc19α; Rigid L20: GFP-30Kc19α-20 aa rigid linker-30Kc19α. (B) Quantification of cell-penetration efficiency among experimental groups. HeLa cells were treated with 1 μM of recombinant cell-penetrating proteins for 1 hour. The relative fluorescence intensity was represented as fold change compared to GFP-treated group.

7.5. Enhanced *in vitro* cell-penetration efficiency of 30Kc19α-L20-30Kc19α compared to 30Kc19α

Linker optimization was conducted, and the flexible linker with a length of 20 aa (L20) was selected for 30Kc19α-Linker-30Kc19α in the previous section. To convince the improvement of intracellular cargo delivery of 30Kc19α-L20-30Kc19α compared to 30Kc19α, other cell-penetration assays were performed. Firstly, ICC staining was conducted. Before treating cells with recombinant proteins, GFP, GFP-30Kc19α, GFP-30Kc19α-L20-30Kc19α were produced in *E. coli*. After the purification steps, single band with the same molecular mass with each protein was observed in the SDS-PAGE gel indicating that high-purity recombinant proteins were obtained (Figure 7.5A). Then, their cytotoxicity was measured by CELLOMAX^{TM} viability assay. No significant cytotoxicity was observed even when HeLa cells were treated with 10 μM (Figure 7.5B). When ICC staining was conducted on recombinant protein-treated HeLa cells, green fluorescence in confocal images showed a tendency to increase in the order of GFP, GFP-30Kc19α, and GFP-30Kc19α-L20-30Kc19α-treated groups (Figure 7.5C). Next, HeLa cells treated with recombinant proteins were analyzed by fluorescence-activated cell sorting (FACS) Aria II (BD Biosciences, USA) for a shift in FITC. Compared to PBS-treated group, the peak shifted to the right, and the shift of the peak increased in the order of GFP, GFP-30Kc19α, and GFP-30Kc19α-L20-30Kc19α-treated group as in ICC analysis (Figure 7.6). P3 (%) values of each group were 0.510, 2.18, 4.52, and 20.7, respectively. To quantify the intracellular delivery efficiency of 30Kc19α and 30Kc19α-L20-30Kc19α, HiBiT lytic detection system was performed. HiBiT tag was inserted into the N-terminus of 30Kc19α and 30Kc19α-L20-30Kc19α. Then,

HiBiT-tagged proteins were produced in *E. coli* and analyzed by Coomassie blue staining and western blot analysis (Figure 7.7A). The band appeared in the expected location on the gel. Standard curves were obtained by mixing LgBiT and substrate with known concentrations of HiBiT-tagged proteins (Figure 7.7B) [156]. HeLa cells were treated with 100 nM or 1 μM of HiBiT-tagged proteins for various times, and then the cell-membrane-bound proteins were washed away. LgBiT protein and substrate were added to plate and the luminescence was measured by microplate reader (Tecan). Luminescence was detected higher in the 1 μM condition than in the 100 nM condition. In 1 μM HiBiT-30Kc19α-L20-30Kc19α-treated group, luminescence was almost maintained over time, while in other groups, the luminescence tended to decrease over time. Number of cell-penetrated proteins were calculated from stadard curves of purified HiBiT-tagged proteins and luminescence (Figure 7.7C). In Figure 7.7D, it could observe that HiBiT-30Kc19α-L20-30Kc19α showed higher luminescence than HiBiT-30Kc19α-L20-30Kc19α. In particular, the luminescence increased by 7.16-fold at 1 uM and 24-hour incubation condition.

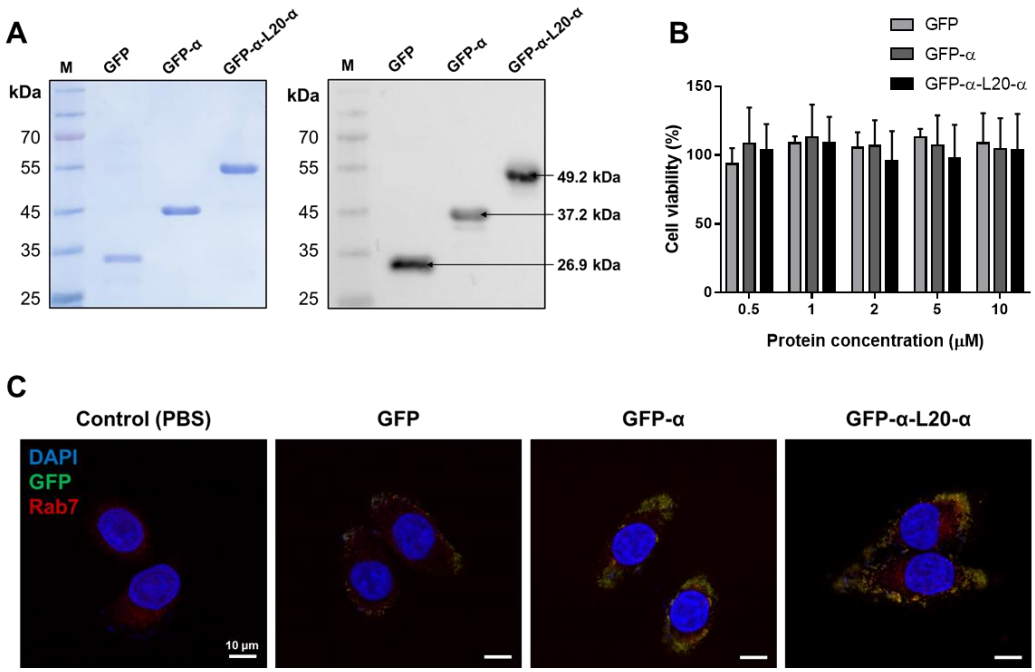

Figure 7.5. Comparison of intracellular cargo delivery efficiency of 30Kc19α and 30Kc19α-L20-30Kc19α by confocal images. (A) Coomassie blue staining and western blot data of recombinant proteins. Anti-His tag antibody was used as primary antibody for purified recombinant proteins. M, marker. (B) CELLOMAX™ cell viability assay data. HeLa cells were treated with various recombinant protein concentrations for 72 hours. (C) Confocal images of GFP-fused protein-treated HeLa cells. Nuclei were stained with DAPI, recombinant proteins with Alexa Fluro® 488, and endosomes with Alexa Fluro® 594 (Scale bar = 10 μm).

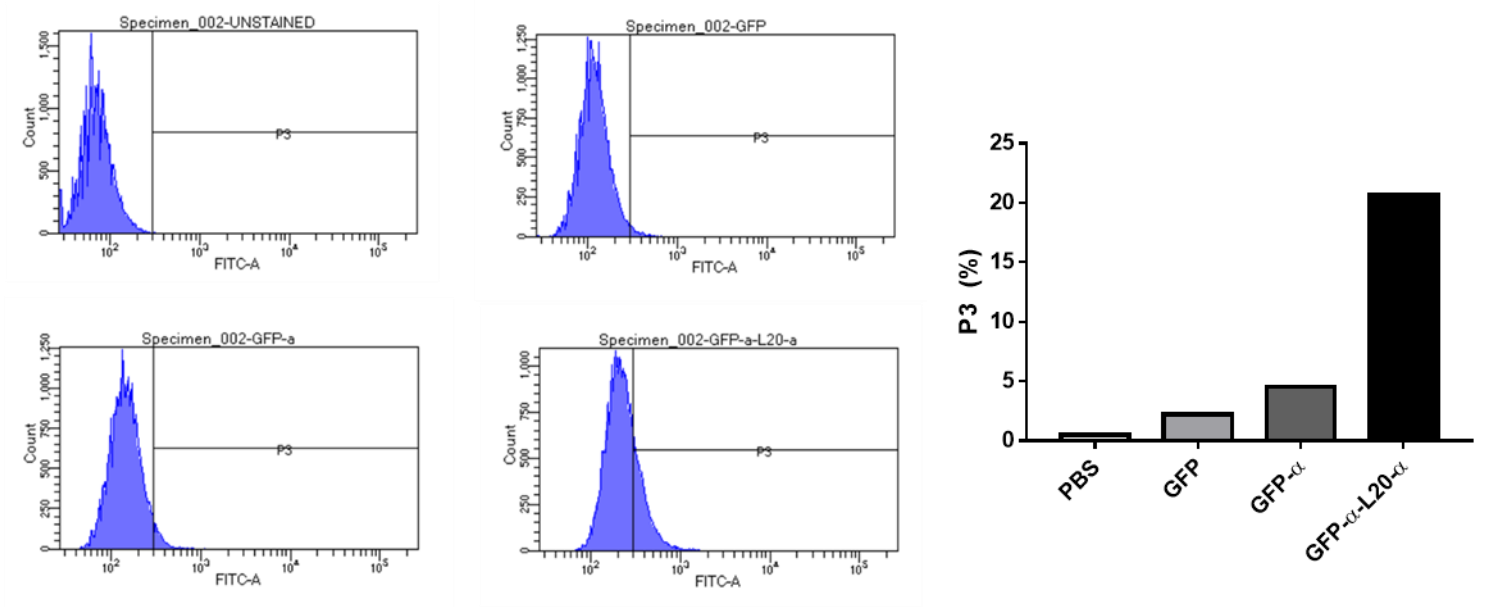

Figure 7.6. Comparison of intracellular cargo delivery efficiency of 30Kc19α and 30Kc19α-L20-30Kc19α by FACS analysis. HeLa cells were treated with 10 μM of recombinant proteins. The proportion of cells belonging to the P3 region among the total cells was indicated by P3 (%) in the graph (right).

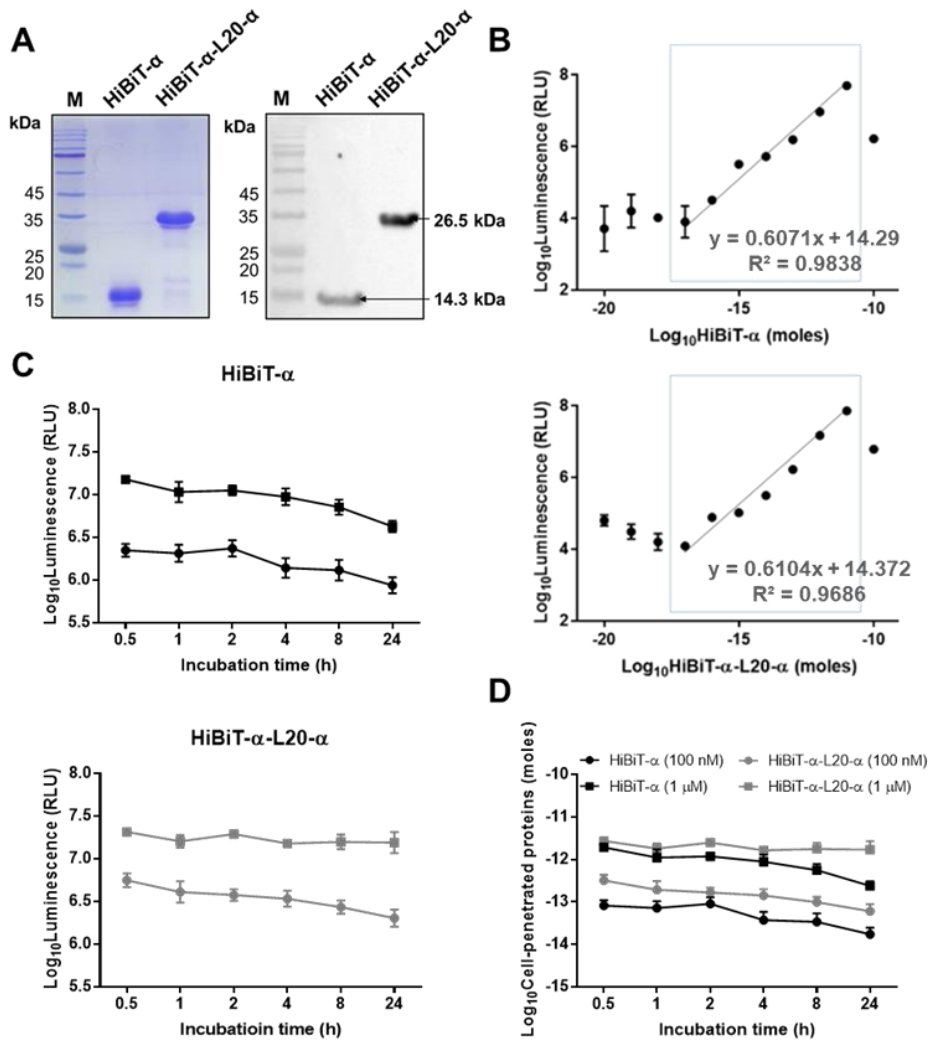

Figure 7.7. Quantification of cell-penetration efficiency using NanoLuc binary technology. (A) Coomassie blue staining and western blot analysis data of HiBiT-tagged 30Kc19α (HiBiT-α) and HiBiT-tagged 30Kc19α-L20-30Kc19α (HiBiT-α-L20-α). Anti-His tag antibody was used as primary antibody. M, marker. (B) Standard curve for Standard curves were obtained for HiBiT-α and HiBiT-α-L20-α by graphing the data (Log_{10}Luminescence versus Log_{10}HiBiT-tagged proteins). (C-D) Cell-penetrated protein quantification using HiBiT lytic detection system. HeLa cells were treated with 100 nM or 1 μM of HiBiT-tagged proteins for 24 hours. Number of cell-penetrated proteins (D) were calculated from luminescence (C) and stadard curves of purified HiBiT-tagged proteins.

7.6. Conclusions

30Kc19α, like 30Kc19, formed dimer in the presence of amphiphilic molecules. When cysteine to alanine mutation was conducted to inhibit dimerization, cell-penetrating ability was dramatically diminished, which means that dimerization of 30Kc19α is important on cell-penetration of 30Kc19α. To increase dimerization thereby increasing cell-penetration, various peptide linkers were tested. 30Kc19α-Linker-30Kc19α showed enhanced cell-penetration than 30Kc19α and among them, 30Kc19α-L20-30Kc19α showed highest cell-penetration efficiency. After that, it was confirmed that 30Kc19α-Linker-30Kc19α delivered the cargo protein into cells with higher efficiency than the conventional 30Kc19α. Therefore, 30Kc19α-Linker-30Kc19α would be a potential vehicle applicable to various fields depending on the properties of the cargo protein.

Chapter 8

Overall discussion and further suggestions

Chapter 8. Overall discussion and further suggestions

In chapter 4, the soluble expression and yield of ADI were enhanced through fusion with 30Kc19α in *E. coli* expression system. The property of 30Kc19α as solubility enhancer was confirmed. According to the previous study, recombinant *Mycoplasma hominis* ADI tends to be expressed as inclusion bodies in *E. coli* [157]. Thus, solubilization and refolding steps are required for the recovery of the enzyme activity [74]. However, recovery of the enzyme activity was not fully achieved even after refolding. In the case of ADI-LK-30Kc19α, about 30% of it was expressed as a soluble form, which means that loss of activity due to refolding could be excluded.

In addition, ADI-LK-30Kc19α was more stable and resistant to proteolysis than ADI. Previous findings demonstrated that 30Kc19α has protein-stabilizing effect, but the underlying mechanism is not well known [14, 87]. One hypothesis is that there is a shielding effect, which could protect cargo proteins from *in vitro* proteolysis [158]. To confirm the hypothesis, *in vitro* proteolysis assay was performed. The results showed that fusion protein was more resistant to proteolysis compared to ADI alone. Indeed, the shielding effect is a factor contributing to the stabilizing property of 30Kc19α.

Currently, mycoplasma-derived PEGylated ADI (ADI-PEG20) is undergoing clinical trials either alone or in combination with other drugs for curing solid tumors such as hepatocellular carcinoma (phase III), melanomas (phase II), and mesothelioma (phase II) [159]. However, ADI-PEG20 has shown efficacy only in treating patients with ASS1-deficient cancers [160-164]. The sensitivity of melanoma cells to ADI treatment is related to arginine auxotrophy [63]. ADI-resistant melanoma cells synthesize arginine on their own by expressing ASS1.

Native ADI which only depletes extracellular arginine. On the other hand, ADI-LK-30Kc19α not only depletes extracellular arginine but also intracellularly regenerated arginine from citrulline. This difference led to overcoming ADI resistance. If both ADI-PEG20 and ADI-LK-30Kc19α are applied to ASS1-positive tumors as a combination therapy, the anti-tumor efficacy could be improved by targeting both extracellular and intracellular arginine.

In chapter 5, the fusion of 30Kc19α with RUNX2 resulted in the soluble expression of recombinant RUNX2 in *E. coli*. Some recombinant proteins, like RUNX2, are obtained as inclusion bodies in *E. coli* due to aggregation. For soluble protein production in *E. coli*, solubility enhancing tags, which can be peptides or proteins (i.e. solubility-enhancer peptide sequences (SET), Fh8, maltose-binding protein (MBP), and N utilization substance A (NusA)), have been used during the protein production process [165, 166]. These tags help the expression of target proteins in soluble forms by preventing association of aggregation-prone intermediates of the proteins [167]. Similar to these tags, 30Kc19 has enhanced the solubility of cargo proteins. In previous studies, when 30Kc19 was fused to transcription factors, the amount of transcription factors expressed in soluble form increased. Since 30Kc19α is a part of the 30Kc19 domain that is expressed in soluble form, we assumed that 30Kc19α can also express cargo protein in a soluble form. By comparing the solubility of RUNX2 and 30Kc19α-RUNX2 proteins, we confirmed that, as expected, 30Kc19α enhances soluble expression of RUNX2.

Another benefit of fusing RUNX2 with 30Kc19α is acquiring cell-penetrating ability. In Figure 5.3C, the confocal image shows 30Kc19α-RUNX2 proteins are spread out in the cytosols and nuclei of hMSCs. However, the treatment of 30Kc19α-only did not show any nuclear localization in hMSCs. GFP, ADI, and bFGF fused

with 30Kc19α were not observed in the nuclei of target cells [14]. Unlike these cargo proteins, RUNX2 has a nuclear localization sequence (NLS) within itself that enables transportation of 30Kc19α-RUNX2 into the nucleus, after penetrating the cell membrane *via* 30Kc19α [168].

In vitro osteogenic differentiation analysis showed osteogenic differentiation in hMSCs treated with 30Kc19α-RUNX2. Treatment of 30Kc19α-RUNX2 to hMSCs up-regulated osteogenic gene expression levels, activated ALP expression, and promoted mineralization. Conventional OM contains dexamethasone, a type of glucocorticoid that regulates the lineage specification of hMSCs to osteoblasts [169-171]. Previous studies have shown that dexamethasone and RUNX2 synergistically induces *bone sialoprotein* and *OCN* gene expression, ALP activity, and mineral deposition [172]. In this study, I also investigated whether 30Kc19α-RUNX2 treatment can induce osteogenesis when hMSCs are cultured in OM without dexamethasone. Real-time PCR analysis and ALP and ARS staining showed enhanced osteogenesis without dexamethasone in cells treated with 30Kc19α-RUNX2, compared to other groups. Successful osteogenic induction of hMSCs in the absence of dexamethasone demonstrates that 30Kc19α-RUNX2 is a potent osteogenic inducing protein.

RUNX2 is an early expression marker for osteoblastic lineage cells [173]. Increased expression of RUNX2 is essential in hMSCs in their initial commitment stage into an osteoblastic lineage. However, maintaining a high expression level of RUNX2 rather inhibits the maturation of osteoblasts [174]. Previous studies confirm that increased expression of *RUNX2* gene or RUNX2 protein in the initial commitment stage successfully induces osteogenic differentiation in hMSCs [108, 175, 176]. Therefore, it was predicted that the intracellular delivery of 30Kc19α-

RUNX2 protein once during the first two days of the osteogenic commitment stage is enough to induce long-lasting cellular phenotype, and would show enhanced osteogenesis in hMSCs (Figure 5.4). However, in the absence of dexamethasone, no red stains were observable in ARS staining [112]. hMSCs that were treated with 30Kc19α-RUNX2 protein twice for the first 4 days showed enhanced osteogenic differentiation (Figure 5.5). This suggests that enhanced osteogenesis requires RUNX2 accumulation to occur in the early stage of osteogenic differentiation.

Due to the accessibility to the defect site of the host cells provided by the macroporous scaffold, host cell migration can occur in the acellular environment, and result in regeneration. Although the BV/TV percentages of the SHAM, hMSC, and 30Kc19α groups did not show significant differences, hMSCs and 30Kc19α-treated hMSCs may differentiate within the macroporous environment, and facilitate the regeneration of bone tissue. For the SHAM group, the initial status of the defect site was acellular, but the porous surrounding of gelatin cryogel allows original host cells to migrate in, and attach to the gelatin network, to form tissue regeneration in the SHAM group. Overall, bone regeneration occurred in all groups. However, MTC and OPN histological staining data demonstrate the highest regeneration capacity in 30Kc19α-RUNX2-treated hMSCs *in vivo*. Unlike cranial defect sites, subcutaneous tissue has lower accessibility of host cells. This enables delivered cells to differentiation and accumulate collagen without the interference of host cells. Thus, results show clear difference in differentiation capacity. hMSCs treated with 30Kc19α-RUNX2 demonstrate highest collagen uptake when delivered to subcutaneous tissue.

In chapter 6, HDFs treated with 30Kc19α-bFGF showed more on the cell surface as well as in the cytosol, than bFGF (Figure 6.3C). Surface deposition occurs

prior to cell-penetration. Since bFGF is a kind of receptor-binding protein, bFGF-deposition to the cell surface can increase the localization of proteins to receptors, which means that there is a higher chance of interactions between bFGF and FGFR. In previous studies, the CPP, TAT was applied to the intracellular delivery of bFGF [177]. The deposition of bFGF on cell membranes by TAT increased the localization of proteins to receptors, increasing the effect of bFGF on hypertrophic scars. Although the effects of 30Kc19α on the receptor binding of cargo protein has not been studied, 30Kc19α is thought to increase the efficiency of interactions between bFGF and FGFR. Cell-penetration of bFGF leads to tissue penetration of bFGF. Facilitated dermal tissue penetration can promote the wound healing process since bFGF can act on cells in deeper dermal tissue. Thus, both surface deposition and cell-penetration are significant in the aspect of drug efficacy on wound healing.

Although 30Kc19α has been known as a CPP, the potential of its skin permeability has not been investigated. In general, proteins have limited skin-penetration ability due to its intrinsic hydrophilic and macromolecular features [149, 178]. A lot of enhancement strategies have been developed for delivering proteins into the skin, such as chemical penetration enhancers, cell- or skin-penetrating peptides, nanocarriers, physical penetration enhancers, and microneedle [179-182]. For delivering bFGF into the skin, Zeng *et al*. used TAT to enable transdermal delivery of aFGF and bFGF, and expand the wound area where aFGF and bFGF can act [177, 183]. More recently, Xu *et al*. reported that a permeation enhancer-inserted liposome improved stability and skin-permeability of bFGF [184]. Here, these findings verified that 30Kc19α improved the skin-penetration of bFGF and expanded its potential for use as a skin-penetrating protein for delivering small molecules and/or macromolecules transdermally. Despite the relatively large molecular weight

of 30Kc19α (12.4 kDa), it was encouraging results that the skin permeability of an NIR fluorophore was increased through the conjugation with 30Kc19α.

The skin-penetration mechanisms of other chemical penetration enhancers have been generally explained according to several modes of action, however, the transport mechanism of CPPs have not been fully explained yet [177, 185]. A surface charge mediated transporting mechanism has been suggested for arginine-rich CPPs (positively charged) that interact with skin cells whose surface is negatively charged, followed by skin-penetration through transcellular, appendage, and intracellular routes [186]. Hou *et al*. reported that micropinocytosis and actin rearrangement were involved in transdermal delivery of proteins [147]. It was investigated that the lipid structure of SC treated with bFGF or 30Kc19α-bFGF *via* X-ray scattering, but there were no distinct peak changes in small-angle or wide-angle regions, demonstrating that 30Kc19α-bFGF may penetrate the skin without altering the lipid organization [87, 187]. In case of dermal tissue-penetration, Shi *et al*. investigated the possible mechanism of tissue-penetration of CPPs [188]. They confirmed CPP's permeability from the top cell monolayer to the bottom using the Transwell model. This suggested that some of the internalized CPPs could exit from cells through exocytosis. It is possible that the penetration of 30Kc19α might follow the aforementioned mechanisms of CPPs; nevertheless, further work will be needed to identify how 30Kc19α acts at the molecular level to make cargo protein permeable to the skin.

The applicability of 30Kc19α-bFGF to wound healing has been confirmed in several aspects. The protein stability, cell-membrane deposition and cell-penetration were enhanced through the fusion with 30Kc19α, followed by improving functions such as cell proliferation and migration rate of HDFs. Based on the wound healing potential of 30Kc19α-bFGF seen with HDFs and HUVECs, it was applied to mouse

wound model. In particular, the regenerative behavior of 30Kc19α-bFGF on cell proliferation and tissue remodeling was investigated [150]. Through Ki67-staining, it was confirmed that 30Kc19α-bFGF facilitated proliferation during wound healing to a greater extent than native bFGF. Moreover, a large granulation tissue area provided evidence that 30Kc19α-bFGF continuously influenced the proliferation and infiltration of cells within the surrounding tissue. If the proliferative phase persists, the wound subsequently becomes scar tissue [189]. Therefore, the tissue remodeling process, which includes ECM rearrangement, angiogenesis, and reformation of skin appendages, is essential for wound repair and recovery of skin tissue functionality. ECM fiber organization is one of the criteria used to determine whether regenerated skin resembles native skin tissue. In general, healthy skin has a basketweave orientation [190, 191]. 30Kc19α-bFGF regenerated the dermal layer with low coherence in ECM fiber alignment (Figure 6.11B), suggesting that it promoted wound repair as well as wound closure. Furthermore, angiogenesis is another critical element of wound healing since it controls the quality of skin tissue after regeneration, and bFGF is deeply involved in angiogenesis [192]. During the proliferative phase (day 14), I observed that vessel formation in the wound bed occurred most actively in the 30Kc19α-bFGF group, followed by maturation during remodeling (day 21). As a result, based on wound size reduction profile and other microscopic analyses, it was confirmed that 30Kc19α enhanced and boosted the ability of bFGF to facilitate wound regeneration both quantitatively and qualitatively. In chapter 5, it was confirmed that 30Kc19α itself did not affect osteogenic differentiation of hMSCs. However, in chapter 6, it was not confirmed whether 30Kc19α itself has any effect on wound healing. As 30Kc19α may have a potential wound healing effect, 30Kc19α should be included in the experimental group to

differentiate the wound healing effect of 30Kc19α from that of bFGF in further studies.

In chapter 7, intracellular cargo delivery efficiency was increased in all groups when two 30Kc19α monomers were connected with linkers. Regardless of the type and length of linker, relative fluorescence intensity increased more than 3.69 times compared to 30Kc19α in all linker groups. Only the linkerless group showed reduced fluorescence compared to 30Kc19α, which was 0.42 times that of 30Kc19α. This indicates that direct connection of two 30Kc19α monomers without linker could interfere with internal dimerization as well as with external dimerization with other 30Kc19α-30Kc19α. In the case of linker type, relative fluorescence intensity was higher with the flexible linker than with the rigid linker. Even 5 aa flexible linker showed higher fluorescence than 20 aa rigid linker. This suggests that the flexibility of linker is important in certain movements or interactions between protein domains [193]. In the case of linker length, it was confirmed that the fluorescence intensity was lowered when the linker length was too short or too long. Short linker length may be insufficient to form a dimer structure between the two protein domains. Van Rosmalen reported that FRET efficiency, ie, intramolecular domain interactions, decreased with increasing length of the glycine-serine linker [194]. This supports the decrease in relative fluorescence intensity when using 50 aa flexible linkers. Taken together, it could be inferred that 20 aa flexible linker was suitable for dimer formation at 30Kc19α in terms of linker type and length.

In Figure 7.5C, endosomes were stained in red fluorescence with anti-Rab7 antibody to observe co-localization of the intracellular recombinant proteins and endosome markers in cells. Most green fluorescence spots were colocalized with red fluorescence spots, which means that some recombinant proteins were located in the

endosome. This is consistent with the results of studies showing that the 30Kc19 penetrates cells by endocytosis, especially macropinocytosis and caveolin-mediated endocytosis [142]. Some of the green fluorescence spots did not overlap with the red fluorescence spots, and these are expected to be proteins delivered into cytosol by endosomal escape [195].

To summarize, in my research during Ph.D., I have identified the properties of 30Kc19α as a solubility enhancer and protein stabilizer for cargo proteins. 30Kc19α could improve the efficacy of therapeutic proteins by simultaneously increasing solubility and stability of cargo proteins during intracellular delivery of therapeutic cargo proteins. Then, I have developed 30Kc19α-based intracellular and transdermal cargo protein delivery system and applied it to therapeutic cargo protein delivery. I could confirm that the therapeutic efficacy of cargo proteins was improved in various disease models. Furthermore, I have designed a cell-penetrating protein, 30Kc19α-Linker-30Kc19α with enhanced cell-penetrating ability of 30Kc19α. It could be applicable to the pharmaceutical fields if used as a intracellular delivery vehicles for drugs that act on unmet intracellular targets.

In some cases, targeted delivery is important for enhancing efficacy and reducing side effects of drugs. In case of *in vivo* systematic delivery, it is important to avoid major accumulation in liver and spleen and target specific tissues and cells [196]. Therefore, specific tissue- or cell-targeting strategies have been developed. For instance, bone-targeted drug delivery has been achieved by targeting hydroxyapatite, a main component of bone minerals, through conjugation with bisphosphonate and hydroxyapatite binding peptide [197-200]. In case of cancer, tumor cell-specific delivery is necessary. Tumor microenvironment (TME) has unique properties such as acidic pH, hypoxia, tumor-specific enzyme and membrane

protein expression. These features are used to develop tumor-targeting CPPs that penetrate only tumor cells. For example, pH-activatable CPP could be designed by using pH-responsive PEG shielding platform [201]. TAT-oxygen-dependent degradation domain-caspase 3 fusion protein stabilizes in the hypoxic conditions of the TME [202]. CPP could be designed to modulate cargo enzyme activity depending on the expression of MMPs within the TME. Tumor-homing peptides could efficiently and specifically penetrate only tumor cells by binding to tumor-specific membrane proteins [203].

Nowadays, the level of targeting is shifting from tissues and cells to organelles in that many diseases result from dysfunction at the organelle level [204]. Usually, signal peptides are peptides which directs the transport of cargo to a specific organelle including nucleus, lysosome, mitochondria, golgi and endoplasmic reticulum [205]. However, the signal peptides do not have free access to intracellular organelles [206]. Thus, 30Kc19α-based intracellular cargo delivery system could be applied to organelle-targeted delivery *via* combination with targeting sequences.

Bibliography

[1] D.C. Andersen, L. Krummen, Recombinant protein expression for therapeutic applications, *Current Opinion in Biotechnology* 13(2) (2002) 117-123.

[2] D.V. Goeddel, D.G. Kleid, F. Bolivar, H.L. Heyneker, D.G. Yansura, R. Crea, T. Hirose, A. Kraszewski, K. Itakura, A.D. Riggs, Expression in *Escherichia coli* of chemically synthesized genes for human insulin, *Proceedings of the National Academy of Sciences* 76(1) (1979) 106-110.

[3] A. Dinca, W.-M. Chien, M.T. Chin, Intracellular delivery of proteins with cell-penetrating peptides for therapeutic uses in human disease, *International Journal of Molecular Sciences* 17(2) (2016) 263.

[4] G.L. Rosano, E.A. Ceccarelli, Recombinant protein expression in *Escherichia coli*: Advances and challenges, *Frontiers in Microbiology* 5 (2014) 172.

[5] H.J. Park, E.J. Kim, T.Y. Koo, T.H. Park, Purification of recombinant 30K protein produced in *Escherichia coli* and its anti-apoptotic effect in mammalian and insect cell systems, *Enzyme and Microbial Technology* 33(4) (2003) 466-471.

[6] W.J. Rhee, E.H. Lee, T.H. Park, Expression of *Bombyx mori* 30Kc19 protein in *Escherichia coli* and its anti-apoptotic effect in Sf9 cell, *Biotechnology and Bioprocess Engineering* 14(5) (2009) 645-650.

[7] J.H. Park, Z. Wang, H.-J. Jeong, H.H. Park, B.-G. Kim, W.-S. Tan, S.S. Choi, T.H. Park, Enhancement of recombinant human EPO production and glycosylation in serum-free suspension culture of CHO cells through expression and supplementation of 30Kc19, *Applied Microbiology and Biotechnology* 96(3) (2012) 671-683.

[8] J.H. Park, H.H. Park, S.S. Choi, T.H. Park, Stabilization of enzymes by the recombinant 30Kc19 protein, *Process Biochemistry* 47(1) (2012) 164-169.

[9] J.H. Park, J.H. Lee, H.H. Park, W.J. Rhee, S.S. Choi, T.H. Park, A protein delivery system using 30Kc19 cell-penetrating protein originating from silkworm, *Biomaterials* 33(35) (2012) 9127-9134.

[10] H.H. Park, Y. Sohn, J.W. Yeo, J.H. Park, H.J. Lee, J. Ryu, W.J. Rhee, T.H. Park, Identification and characterization of a novel cell-penetrating peptide of 30Kc19 protein derived from *Bombyx mori*, *Process Biochemistry* 49(9) (2014) 1516-1526.

[11] H.J. Lee, H.H. Park, J.A. Kim, J.H. Park, J. Ryu, J. Choi, J. Lee, W.J. Rhee, T.H. Park, Enzyme delivery using the 30Kc19 protein and human serum albumin nanoparticles, *Biomaterials* 35(5) (2014) 1696-1704.

[12] J. Ryu, H.H. Park, J.H. Park, H.J. Lee, W.J. Rhee, T.H. Park, Soluble expression and stability enhancement of transcription factors using 30Kc19 cell-penetrating protein, *Applied Microbiology and Biotechnology* 100(8) (2016) 3523-3532.

[13] J. Ryu, N.S. Hwang, H.H. Park, T.H. Park, Protein-based direct reprogramming of fibroblasts to neuronal cells using 30Kc19 protein and transcription factor Ascl1, *The International Journal of Biochemistry & Cell Biology* 121 (2020) 105717.

[14] J. Ryu, H. Kim, H.H. Park, H.J. Lee, J.H. Park, W.J. Rhee, T.H. Park, Protein-stabilizing and cell-penetrating properties of α-helix domain of 30Kc19 protein, *Biotechnology Journal* 11(11) (2016) 1443-1451.

[15] M. Lindgren, M. Hällbrink, A. Prochiantz, Ü. Langel, Cell-penetrating peptides, *Trends in Pharmacological Sciences* 21(3) (2000) 99-103.

[16] W.L. Munyendo, H. Lv, H. Benza-Ingoula, L.D. Baraza, J. Zhou, Cell penetrating peptides in the delivery of biopharmaceuticals, *Biomolecules* 2(2) (2012) 187-202.

[17] A.D. Frankel, C.O. Pabo, Cellular uptake of the tat protein from human immunodeficiency virus, *Cell* 55(6) (1988) 1189-1193.

[18] M. Pooga, Ü. Langel, Classes of cell-penetrating peptides, *Cell-Penetrating Peptides*, Springer 2015, pp. 3-28.

[19] E. Eiríksdóttir, K. Konate, Ü. Langel, G. Divita, S. Deshayes, Secondary structure of

cell-penetrating peptides controls membrane interaction and insertion, *Biochimica et Biophysica Acta (BBA)-Biomembranes* 1798(6) (2010) 1119-1128.
[20] P.E. Thorén, D. Persson, M. Karlsson, B. Nordén, The antennapedia peptide penetratin translocates across lipid bilayers–the first direct observation, *FEBS Letters* 482(3) (2000) 265-268.
[21] S. Futaki, T. Suzuki, W. Ohashi, T. Yagami, S. Tanaka, K. Ueda, Y. Sugiura, Arginine-rich peptides: An abundant source of membrane-permeable peptides having potential as carriers for intracellular protein delivery, *Journal of Biological Chemistry* 276(8) (2001) 5836-5840.
[22] S. Deshayes, A. Heitz, M.C. Morris, P. Charnet, G. Divita, F. Heitz, Insight into the mechanism of internalization of the cell-penetrating carrier peptide Pep-1 through conformational analysis, *Biochemistry* 43(6) (2004) 1449-1457.
[23] F. Milletti, Cell-penetrating peptides: Classes, origin, and current landscape, *Drug Discovery Today* 17(15-16) (2012) 850-860.
[24] T. Singh, A.S. Murthy, H.-J. Yang, J. Im, Versatility of cell-penetrating peptides for intracellular delivery of siRNA, *Drug Delivery* 25(1) (2018) 1996-2006.
[25] S.E. Park, M.I. Sajid, K. Parang, R.K. Tiwari, Cyclic cell-penetrating peptides as efficient intracellular drug delivery tools, *Molecular Pharmaceutics* 16(9) (2019) 3727-3743.
[26] C.-Y. Jiao, D. Delaroche, F. Burlina, I.D. Alves, G. Chassaing, S. Sagan, Translocation and endocytosis for cell-penetrating peptide internalization, *Journal of Biological Chemistry* 284(49) (2009) 33957-33965.
[27] D. Dutta, J.G. Donaldson, Search for inhibitors of endocytosis: Intended specificity and unintended consequences, *Cellular Logistics* 2(4) (2012) 203-208.
[28] C.K. Payne, S.A. Jones, C. Chen, X. Zhuang, Internalization and trafficking of cell surface proteoglycans and proteoglycan-binding ligands, *Traffic* 8(4) (2007) 389-401.
[29] M. Ashrafuzzaman, M. Ashrafuzzaman, Cell surface diffusion and adsorption, *Nanoscale Biophysics of the Cell*, Springer 2018, pp. 75-133.
[30] P.E. Thorén, D. Persson, P. Isakson, M. Goksör, A. Önfelt, B. Nordén, Uptake of analogs of penetratin, Tat (48–60) and oligoarginine in live cells, *Biochemical and Biophysical Research Communications* 307(1) (2003) 100-107.
[31] P.E. Thorén, D. Persson, P. Lincoln, B. Nordén, Membrane destabilizing properties of cell-penetrating peptides, *Biophysical Chemistry* 114(2-3) (2005) 169-179.
[32] J.P. Richard, K. Melikov, E. Vives, C. Ramos, B. Verbeure, M.J. Gait, L.V. Chernomordik, B. Lebleu, Cell-penetrating peptides: A reevaluation of the mechanism of cellular uptake, *Journal of Biological Chemistry* 278(1) (2003) 585-590.
[33] S. Patel, J. Kim, M. Herrera, A. Mukherjee, A.V. Kabanov, G. Sahay, Brief update on endocytosis of nanomedicines, *Advanced Drug Delivery Reviews* 144 (2019) 90-111.
[34] S.D. Conner, S.L. Schmid, Regulated portals of entry into the cell, *Nature* 422(6927) (2003) 37-44.
[35] J.P. Lim, P.A. Gleeson, Macropinocytosis: An endocytic pathway for internalising large gulps, *Immunology and Cell Biology* 89(8) (2011) 836-843.
[36] M. Gestin, M. Dowaidar, Ü. Langel, Uptake mechanism of cell-penetrating peptides, *Peptides and Peptide-Based Biomaterials and their Biomedical Applications*, Springer 2017, pp. 255-264.
[37] A.D. Riggs, Making, cloning, and the expression of human insulin genes in bacteria: The path to Humulin, *Endocrine Reviews* 42(3) (2021) 374-380.
[38] G. Walsh, E. Walsh, Biopharmaceutical benchmarks 2022, *Nature Biotechnology* (2022) 1-39.
[39] L. McElwain, K. Phair, C. Kealey, D. Brady, Current trends in biopharmaceuticals production in *Escherichia coli*, *Biotechnology Letters* 44(8) (2022) 917-931.
[40] A. Sandomenico, J.P. Sivaccumar, M. Ruvo, Evolution of *Escherichia coli* expression system in producing antibody recombinant fragments, *International Journal of Molecular Sciences* 21(17) (2020) 6324.

[41] R.V. Kholodenko, D.V. Kalinovsky, I.I. Doronin, E.D. Ponomarev, I.V. Kholodenko, Antibody fragments as potential biopharmaceuticals for cancer therapy: Success and limitations. *Current Medicinal Chemistry* 26(3) (2019) 396-426.
[42] H. Hussain, T. Patel, A.M. Ozanne, D. Vito, M. Ellis, M. Hinchliffe, D.P. Humphreys, P.E. Stephens, B. Sweeney, J. White, A comparative analysis of recombinant Fab and full-length antibody production in Chinese hamster ovary cells, *Biotechnology and Bioengineering* 118(12) (2021) 4815-4828.
[43] T. Du, N. Buenbrazo, L. Kell, S. Rahmani, L. Sim, S.G. Withers, S. DeFrees, W. Wakarchuk, A bacterial expression platform for production of therapeutic proteins containing human-like O-linked glycans, *Cell Chemical Biology* 26(2) (2019) 203-212.
[44] G.L. Rosano, E.S. Morales, E.A. Ceccarelli, New tools for recombinant protein production in *Escherichia coli*: A 5-year update, *Protein Science* 28(8) (2019) 1412-1422.
[45] Z. Lipinszki, V. Vernyik, N. Farago, T. Sari, L.G. Puskas, F.R. Blattner, G. Posfai, Z. Gyorfy, Enhancing the translational capacity of *E. coli* by resolving the codon bias, *ACS Synthetic Biology* 7(11) (2018) 2656-2664.
[46] C. Elena, P. Ravasi, M.E. Castelli, S. Peirú, H.G. Menzella, Expression of codon optimized genes in microbial systems: Current industrial applications and perspectives, *Frontiers in Microbiology* 5 (2014) 21.
[47] J. Kaur, A. Kumar, J. Kaur, Strategies for optimization of heterologous protein expression in *E. coli*: Roadblocks and reinforcements, *International Journal of Biological Macromolecules* 106 (2018) 803-822.
[48] K. Fatima, F. Naqvi, H. Younas, A review: Molecular chaperone-mediated folding, unfolding and disaggregation of expressed recombinant proteins, *Cell Biochemistry and Biophysics* 79(2) (2021) 153-174.
[49] C. Köppl, N. Lingg, A. Fischer, C. Kröß, J. Loibl, W. Buchinger, R. Schneider, A. Jungbauer, G. Striedner, M. Cserjan-Puschmann, Fusion tag design influences soluble recombinant protein production in *Escherichia coli*, *International Journal of Molecular Sciences* 23(14) (2022) 7678.
[50] S.M. Hayat, N. Farahani, B. Golichenari, A. Sahebkar, Recombinant protein expression in *Escherichia coli* (*E. coli*): What we need to know, *Current Pharmaceutical Design* 24(6) (2018) 718-725.
[51] A.S. El-Sayed, A.A. Shindia, A.A. Abou Zeid, A.M. Yassin, M.Z. Sitohy, B. Sitohy, *Aspergillus nidulans* thermostable arginine deiminase-Dextran conjugates with enhanced molecular stability, proteolytic resistance, pharmacokinetic properties and anticancer activity, *Enzyme and Microbial Technology* 131 (2019) 109432.
[52] E. Gasteiger, C. Hoogland, A. Gattiker, M.R. Wilkins, R.D. Appel, A. Bairoch, Protein identification and analysis tools on the ExPASy server, *The Proteomics Protocols Handbook*, Humana press 2005, pp. 571-607.
[53] W.-B. Tsai, I. Aiba, S.-Y. Lee, L. Feun, N. Savaraj, M.T. Kuo, Resistance to arginine deiminase treatment in melanoma cells is associated with induced argininosuccinate synthetase expression involving c-Myc/HIF-1α/Sp4, *Molecular Cancer Therapeutics* 8(12) (2009) 3223-3233.
[54] S. Cho, M.J. Shon, B. Son, G.S. Eun, T.-Y. Yoon, T.H. Park, Tension exerted on cells by magnetic nanoparticles regulates differentiation of human mesenchymal stem cells, *Biomaterials Advances* 139 (2022) 213028.
[55] S.H.L. Kim, S.S. Lee, I. Kim, J. Kwon, S. Kwon, T. Bae, J. Hur, H. Lee, N.S. Hwang, Ectopic transient overexpression of OCT-4 facilitates BMP4-induced osteogenic transdifferentiation of human umbilical vein endothelial cells, *Journal of Tissue Engineering* 11 (2020) 2041731420909208.
[56] S.M. Morris Jr, Regulation of enzymes of urea and arginine synthesis, *Annual Review of Nutrition* 12(1) (1992) 81-101.
[57] B.J. Dillon, V.G. Prieto, S.A. Curley, C.M. Ensor, F.W. Holtsberg, J.S. Bomalaski, M.A. Clark, Incidence and distribution of argininosuccinate synthetase deficiency in human

cancers: A method for identifying cancers sensitive to arginine deprivation, *Cancer* 100(4) (2004) 826-833.
[58] B. Delage, D.A. Fennell, L. Nicholson, I. McNeish, N.R. Lemoine, T. Crook, P.W. Szlosarek, Arginine deprivation and argininosuccinate synthetase expression in the treatment of cancer, *International Journal of Cancer* 126(12) (2010) 2762-2772.
[59] M. Patil, J. Bhaumik, S. Babykutty, U. Banerjee, D. Fukumura, Arginine dependence of tumor cells: Targeting a chink in cancer's armor, *Oncogene* 35(38) (2016) 4957-4972.
[60] M.M. Phillips, M.T. Sheaff, P.W. Szlosarek, Targeting arginine-dependent cancers with arginine-degrading enzymes: Opportunities and challenges, *Cancer Research and Treatment: Official Journal of Korean Cancer Association* 45(4) (2013) 251.
[61] M. Zúñiga, G. Pérez, F. González-Candelas, Evolution of arginine deiminase (ADI) pathway genes, *Molecular Phylogenetics and Evolution* 25(3) (2002) 429-444.
[62] R. Marquis, G. Bender, D. Murray, A. Wong, Arginine deiminase system and bacterial adaptation to acid environments, *Applied and Environmental Microbiology* 53(1) (1987) 198-200.
[63] C. Riess, F. Shokraie, C.F. Classen, B. Kreikemeyer, T. Fiedler, C. Junghanss, C. Maletzki, Arginine-depleting enzymes–An increasingly recognized treatment strategy for therapy-refractory malignancies, *Cellular Physiology and Biochemistry* 51(2) (2018) 854-870.
[64] H. Takaku, M. Takase, S.I. Abe, H. Hayashi, K. Miyazaki, *In vivo* anti-tumor activity of arginine deiminase purified from *Mycoplasma arginini*, *International Journal of Cancer* 51(2) (1992) 244-249.
[65] Y. Ni, U. Schwaneberg, Z.-H. Sun, Arginine deiminase, a potential anti-tumor drug, *Cancer Letters* 261(1) (2008) 1-11.
[66] R.H. Kim, J.M. Coates, T.L. Bowles, G.P. McNerney, J. Sutcliffe, J.U. Jung, R. Gandour-Edwards, F.Y. Chuang, R.J. Bold, H.-J. Kung, Arginine deiminase as a novel therapy for prostate cancer induces autophagy and caspase-independent apoptosis, *Cancer Research* 69(2) (2009) 700-708.
[67] C.A. Changou, Y.-R. Chen, L. Xing, Y. Yen, F.Y. Chuang, R.H. Cheng, R.J. Bold, D.K. Ann, H.-J. Kung, Arginine starvation-associated atypical cellular death involves mitochondrial dysfunction, nuclear DNA leakage, and chromatin autophagy, *Proceedings of the National Academy of Sciences* 111(39) (2014) 14147-14152.
[68] F.M. Veronese, G. Pasut, PEGylation, successful approach to drug delivery, *Drug Discovery Today* 10(21) (2005) 1451-1458.
[69] G. Molineux, Pegylation: Engineering improved biopharmaceuticals for oncology, *Pharmacotherapy: The Journal of Human Pharmacology and Drug Therapy* 23(8P2) (2003) 3S-8S.
[70] F. Zhang, M.-r. Liu, H.-t. Wan, Discussion about several potential drawbacks of PEGylated therapeutic proteins, *Biological and Pharmaceutical Bulletin* 37(3) (2014) 335-339.
[71] Y. Long, W.-B. Tsai, M. Wangpaichitr, T. Tsukamoto, N. Savaraj, L.G. Feun, M.T. Kuo, Arginine deiminase resistance in melanoma cells is associated with metabolic reprogramming, glucose dependence, and glutamine addiction, *Molecular Cancer Therapeutics* 12(11) (2013) 2581-2590.
[72] F.-L.L. Wu, T.-H. Yeh, Y.-L. Chen, Y.-C. Chiu, J.-C. Cheng, M.-F. Wei, L.-J. Shen, Intracellular delivery of recombinant arginine deiminase (rADI) by heparin-binding hemagglutinin adhesion peptide restores sensitivity in rADI-resistant cancer cells, *Molecular Pharmaceutics* 11(8) (2014) 2777-2786.
[73] T.-H. Yeh, Y.-R. Chen, S.-Y. Chen, W.-C. Shen, D.K. Ann, J.L. Zaro, L.-J. Shen, Selective intracellular delivery of recombinant arginine deiminase (ADI) using pH-sensitive cell penetrating peptides to overcome ADI resistance in hypoxic breast cancer cells, *Molecular Pharmaceutics* 13(1) (2016) 262-271.
[74] S.M. Singh, A.K. Panda, Solubilization and refolding of bacterial inclusion body proteins, *Journal of Bioscience and Bioengineering* 99(4) (2005) 303-310.

[75] J.-A. Song, D.-S. Lee, J.-S. Park, K.-Y. Han, J. Lee, A novel *Escherichia coli* solubility enhancer protein for fusion expression of aggregation-prone heterologous proteins, *Enzyme and Microbial Technology* 49(2) (2011) 124-130.
[76] K.-Y. Ahn, B. Lee, K.-Y. Han, J.-A. Song, D.S. Lee, J. Lee, Synthesis of *Mycoplasma* arginine deiminase in *E. coli* using stress-responsive proteins, *Enzyme and Microbial Technology* 63 (2014) 46-49.
[77] Y.-S. Kang, J.-A. Song, K.-Y. Han, J. Lee, *Escherichia coli* EDA is a novel fusion expression partner to improve solubility of aggregation-prone heterologous proteins, *Journal of Biotechnology* 194 (2015) 39-47.
[78] W.J. Rhee, E.J. Kim, T.H. Park, Kinetic effect of silkworm hemolymph on the delayed host cell death in an insect cell-baculovirus system, *Biotechnology Progress* 15(6) (1999) 1028-1032.
[79] E.J. Kim, T.H. Park, Anti-apoptosis engineering, *Biotechnology and Bioprocess Engineering* 8(2) (2003) 76-82.
[80] E.J. Kim, W.J. Rhee, T.H. Park, Inhibition of apoptosis by a *Bombyx mori* gene, *Biotechnology Progress* 20(1) (2004) 324-329.
[81] S.S. Choi, W.J. Rhee, T.H. Park, Beneficial effect of silkworm hemolymph on a CHO cell system: Inhibition of apoptosis and increase of EPO production, *Biotechnology and Bioengineering* 91(7) (2005) 793-800.
[82] J.E. Kim, E.J. Kim, W.J. Rhee, T.H. Park, Enhanced production of recombinant protein in *Escherichia coli* using silkworm hemolymph, *Biotechnology and Bioprocess Engineering* 10(4) (2005) 353-356.
[83] J.-P. Yang, X.-X. Ma, Y.-X. He, W.-F. Li, Y. Kang, R. Bao, Y. Chen, C.-Z. Zhou, Crystal structure of the 30 K protein from the silkworm *Bombyx mori* reveals a new member of the β-trefoil superfamily, *Journal of Structural Biology* 175(1) (2011) 97-103.
[84] Z. Wang, J.H. Park, H.H. Park, W. Tan, T.H. Park, Enhancement of recombinant human EPO production and sialylation in Chinese Hamster Ovary cells through *Bombyx mori 30Kc19* gene expression, *Biotechnology and Bioengineering* 108(7) (2011) 1634-1642.
[85] H.H. Park, Y.H. Woo, J. Ryu, H.J. Lee, J.H. Park, T.H. Park, Enzyme delivery using protein-stabilizing and cell-penetrating 30Kc19α protein nanoparticles, *Process Biochemistry* 63 (2017) 76-83.
[86] H. Lee, S.H.L. Kim, H. Yoon, J. Ryu, H.H. Park, N.S. Hwang, T.H. Park, Intracellular delivery of recombinant RUNX2 facilitated by cell-penetrating protein for the osteogenic differentiation of hMSCs, *ACS Biomaterials Science & Engineering* 6(9) (2020) 5202-5214.
[87] H. Lee, Y.H. An, T.K. Kim, J. Ryu, G.K. Park, M.J. Park, J. Ko, H. Kim, H.S. Choi, N.S. Hwang, Enhancement of wound healing efficacy by increasing the stability and skin-penetrating property of bFGF using 30Kc19α-based fusion protein, *Advanced Biology* 5(1) (2021) 2000176.
[88] Q. Yao, L. Kou, Y. Tu, L. Zhu, MMP-responsive 'smart' drug delivery and tumor targeting, *Trends in Pharmacological Sciences* 39(8) (2018) 766-781.
[89] 박근화, Enhancement of solubility, cell penetration, and stability of arginine deiminase using 30Kc19α for effective melanoma treatment, 서울대학교 대학원, 2022.
[90] H. Lee, G. Park, S. Kim, B. Son, J. Joo, H.H. Park, T.H. Park, Enhancement of anti-tumor activity in melanoma using arginine deiminase fused with 30Kc19α protein, *Applied Microbiology and Biotechnology* 106(22) (2022) 7531–7545.
[91] C.M. Ensor, F.W. Holtsberg, J.S. Bomalaski, M.A. Clark, Pegylated arginine deiminase (ADI-SS-PEG20,000 MW) inhibits human melanomas and hepatocellular carcinomas *in vitro* and *in vivo*, *Cancer Research* 62(19) (2002) 5443-5450.
[92] K. Oh-Hashi, E. Furuta, K. Fujimura, Y. Hirata, Application of a novel HiBiT peptide tag for monitoring ATF4 protein expression in Neuro2a cells, *Biochemistry and Biophysics Reports* 12 (2017) 40-45.
[93] M. Wu, G. Chen, Y.-P. Li, TGF-β and BMP signaling in osteoblast, skeletal development, and bone formation, homeostasis and disease, *Bone Research* 4(1) (2016) 1-21.

[94] L. Xian, X. Wu, L. Pang, M. Lou, C.J. Rosen, T. Qiu, J. Crane, F. Frassica, L. Zhang, J.P. Rodriguez, Matrix IGF-1 maintains bone mass by activation of mTOR in mesenchymal stem cells, *Nature Medicine* 18(7) (2012) 1095-1101.
[95] T. Gaur, C.J. Lengner, H. Hovhannisyan, R.A. Bhat, P.V. Bodine, B.S. Komm, A. Javed, A.J. Van Wijnen, J.L. Stein, G.S. Stein, Canonical WNT signaling promotes osteogenesis by directly stimulating *Runx2* gene expression, *Journal of Biological Chemistry* 280(39) (2005) 33132-33140.
[96] A.W. James, G. LaChaud, J. Shen, G. Asatrian, V. Nguyen, X. Zhang, K. Ting, C. Soo, A review of the clinical side effects of bone morphogenetic protein-2, *Tissue Engineering Part B: Reviews* 22(4) (2016) 284-297.
[97] C. Rouaux, P. Arlotta, Fezf2 directs the differentiation of corticofugal neurons from striatal progenitors *in vivo*, *Nature Neuroscience* 13(11) (2010) 1345-1347.
[98] S. Lee, C. Park, J.W. Han, J.Y. Kim, K. Cho, E.J. Kim, S. Kim, S.-J. Lee, S.Y. Oh, Y. Tanaka, Direct reprogramming of human dermal fibroblasts into endothelial cells using ER71/ETV2, *Circulation Research* 120(5) (2017) 848-861.
[99] C. Wang, W. Liu, Y. Nie, M. Qaher, H.E. Horton, F. Yue, A. Asakura, S. Kuang, Loss of MyoD promotes fate transdifferentiation of myoblasts into brown adipocytes, *EBioMedicine* 16 (2017) 212-223.
[100] Y.-P. Yang, F. Thorel, D.F. Boyer, P.L. Herrera, C.V. Wright, Context-specific α-to-β-cell reprogramming by forced Pdx1 expression, *Genes & Development* 25(16) (2011) 1680-1685.
[101] C. Zhao, W. Jiang, N. Zhou, J. Liao, M. Yang, N. Hu, X. Liang, W. Xu, H. Chen, W. Liu, Sox9 augments BMP2-induced chondrogenic differentiation by downregulating Smad7 in mesenchymal stem cells (MSCs), *Genes & Diseases* 4(4) (2017) 229-239.
[102] P. Tontonoz, E. Hu, B.M. Spiegelman, Stimulation of adipogenesis in fibroblasts by PPARγ2, a lipid-activated transcription factor, *Cell* 79(7) (1994) 1147-1156.
[103] S.J. Park, S.-H. Jung, G. Jogeswar, H.-M. Ryoo, J.I. Yook, H.S. Choi, Y. Rhee, C.-H. Kim, S.-K. Lim, The transcription factor snail regulates osteogenic differentiation by repressing Runx2 expression, *Bone* 46(6) (2010) 1498-1507.
[104] A. Hayrapetyan, J.A. Jansen, J.J. van den Beucken, Signaling pathways involved in osteogenesis and their application for bone regenerative medicine, *Tissue Engineering Part B: Reviews* 21(1) (2015) 75-87.
[105] E. Birmingham, G. Niebur, P.E. McHugh, Osteogenic differentiation of mesenchymal stem cells is regulated by osteocyte and osteoblast cells in a simplified bone niche, *European Cells and Materials* 23 (2012) 13-27.
[106] M.S. Rahman, N. Akhtar, H.M. Jamil, R.S. Banik, S.M. Asaduzzaman, TGF-β/BMP signaling and other molecular events: Regulation of osteoblastogenesis and bone formation, *Bone Research* 3(1) (2015) 1-20.
[107] L. Song, N.E. Webb, Y. Song, R.S. Tuan, Identification and functional analysis of candidate genes regulating mesenchymal stem cell self-renewal and multipotency, *Stem Cells* 24(7) (2006) 1707-1718.
[108] Z. Zhao, M. Zhao, G. Xiao, R.T. Franceschi, Gene transfer of the Runx2 transcription factor enhances osteogenic activity of bone marrow stromal cells *in vitro* and *in vivo*, *Molecular Therapy* 12(2) (2005) 247-253.
[109] L. Dalle Carbonare, G. Innamorati, M.T. Valenti, Transcription factor Runx2 and its application to bone tissue engineering, *Stem Cell Reviews and Reports* 8(3) (2012) 891-897.
[110] K.L. Douglas, Toward development of artificial viruses for gene therapy: A comparative evaluation of viral and non-viral transfection, *Biotechnology Progress* 24(4) (2008) 871-883.
[111] M. Mäe, Ü. Langel, Cell-penetrating peptides as vectors for peptide, protein and oligonucleotide delivery, *Current Opinion in Pharmacology* 6(5) (2006) 509-514.
[112] 이해인, Inducing osteogenic differentiation of human mesenchymal stem cell using 30Kc19α-Runx2 protein, 서울대학교 대학원, 2019.

[113] S.T. Koshy, T.C. Ferrante, S.A. Lewin, D.J. Mooney, Injectable, porous, and cell-responsive gelatin cryogels, *Biomaterials* 35(8) (2014) 2477-2487.
[114] M. Rezaeeyazdi, T. Colombani, A. Memic, S.A. Bencherif, Injectable hyaluronic acid-co-gelatin cryogels for tissue-engineering applications, *Materials* 11(8) (2018) 1374.
[115] J. Tao, Y. Hu, S. Wang, J. Zhang, X. Liu, Z. Gou, H. Cheng, Q. Liu, Q. Zhang, S. You, A 3D-engineered porous conduit for peripheral nerve repair, *Scientific Reports* 7(1) (2017) 1-13.
[116] P. Ducy, M. Starbuck, M. Priemel, J. Shen, G. Pinero, V. Geoffroy, M. Amling, G. Karsenty, A Cbfa1-dependent genetic pathway controls bone formation beyond embryonic development, *Genes & Development* 13(8) (1999) 1025-1036.
[117] P. Ducy, R. Zhang, V. Geoffroy, A.L. Ridall, G. Karsenty, Osf2/Cbfa1: A transcriptional activator of osteoblast differentiation, *Cell* 89(5) (1997) 747-754.
[118] A. Javed, G.L. Barnes, B. Jasanya, J.L. Stein, L. Gerstenfeld, J.B. Lian, G.S. Stein, runt homology domain transcription factors (Runx, Cbfa, and AML) mediate repression of the bone sialoprotein promoter: Evidence for promoter context-dependent activity of Cbfa proteins, *Molecular and Cellular Biology* 21(8) (2001) 2891-2905.
[119] D.M. Ornitz, N. Itoh, The fibroblast growth factor signaling pathway, *Wiley Interdisciplinary Reviews: Developmental Biology* 4(3) (2015) 215-266.
[120] B. Behm, P. Babilas, M. Landthaler, S. Schreml, Cytokines, chemokines and growth factors in wound healing, *Journal of the European Academy of Dermatology and Venereology* 26(7) (2012) 812-820.
[121] S. Barrientos, O. Stojadinovic, M.S. Golinko, H. Brem, M. Tomic-Canic, Growth factors and cytokines in wound healing, *Wound Repair and Regeneration* 16(5) (2008) 585-601.
[122] S. Kanazawa, T. Fujiwara, S. Matsuzaki, K. Shingaki, M. Taniguchi, S. Miyata, M. Tohyama, Y. Sakai, K. Yano, K. Hosokawa, bFGF regulates PI3-kinase-Rac1-JNK pathway and promotes fibroblast migration in wound healing, *PLoS One* 5(8) (2010) e12228.
[123] Y.H. Song, Y.T. Zhu, J. Ding, F.Y. Zhou, J.X. Xue, J.H. Jung, Z.J. Li, W.Y. Gao, Distribution of fibroblast growth factors and their roles in skin fibroblast cell migration, *Molecular Medicine Reports* 14(4) (2016) 3336-3342.
[124] E.J. O'keefe, M.L. Chiu, R.E. Payne Jr, Stimulation of growth of keratinocytes by basic fibroblast growth factor, *Journal of Investigative Dermatology* 90(5) (1988).
[125] Y. Sogabe, M. Abe, Y. Yokoyama, O. Ishikawa, Basic fibroblast growth factor stimulates human keratinocyte motility by Rac activation, *Wound Repair and Regeneration* 14(4) (2006) 457-462.
[126] M. Przybylski, A review of the current research on the role of bFGF and VEGF in angiogenesis, *Journal of Wound Care* 18(12) (2009) 516-519.
[127] R. Montesano, J.-D. Vassalli, A. Baird, R. Guillemin, L. Orci, Basic fibroblast growth factor induces angiogenesis *in vitro*, *Proceedings of the National Academy of Sciences* 83(19) (1986) 7297-7301.
[128] S. Akita, K. Akino, A. Hirano, Basic fibroblast growth factor in scarless wound healing, *Advances in Wound Care* 2(2) (2013) 44-49.
[129] T. Sasaki, The effects of basic fibroblast growth factor and doxorubicin on cultured human skin fibroblasts: Relevance to wound healing, *The Journal of Dermatology* 19(11) (1992) 664-666.
[130] H. Uchi, A. Igarashi, K. Urabe, T. Koga, J. Nakayama, R. Kawamori, K. Tamaki, H. Hirakata, T. Ohura, M. Furue, Clinical efficacy of basic fibroblast growth factor (bFGF) for diabetic ulcer, *European Journal of Dermatology* 19(5) (2009) 461-468.
[131] Q.M. Nunes, Y. Li, C. Sun, T.K. Kinnunen, D.G. Fernig, Fibroblast growth factors as tissue repair and regeneration therapeutics, *PeerJ* 4 (2016) e1535.
[132] S. Akita, K. Akino, T. Imaizumi, A. Hirano, Basic fibroblast growth factor accelerates and improves second-degree burn wound healing, *Wound Repair and Regeneration* 16(5) (2008) 635-641.

[133] G.S. McGee, J.M. Davidson, A. Buckley, A. Sommer, S.C. Woodward, A.M. Aquino, R. Barbour, A.A. Demetriou, Recombinant basic fibroblast growth factor accelerates wound healing, *Journal of Surgical Research* 45(1) (1988) 145-153.
[134] Y.J. Wang, Z. Shahrokh, S. Vemuri, G. Eberlein, I. Beylin, M. Busch, Characterization, stability, and formulations of basic fibroblast growth factor, *Formulation, Characterization, and Stability of Protein Drugs: Case Histories*, Springer 2002, pp. 141-180.
[135] A.C. Mitchell, P.S. Briquez, J.A. Hubbell, J.R. Cochran, Engineering growth factors for regenerative medicine applications, *Acta Biomaterialia* 30 (2016) 1-12.
[136] P. Dvorak, D. Bednar, P. Vanacek, L. Balek, L. Eiselleova, V. Stepankova, E. Sebestova, M. Kunova Bosakova, Z. Konecna, S. Mazurenko, Computer-assisted engineering of hyperstable fibroblast growth factor 2, *Biotechnology and Bioengineering* 115(4) (2018) 850-862.
[137] A. Beenken, M. Mohammadi, The FGF family: Biology, pathophysiology and therapy, *Nature Reviews Drug Discovery* 8(3) (2009) 235-253.
[138] S.M. Choi, K.-M. Lee, H.J. Kim, I.K. Park, H.J. Kang, H.-C. Shin, D. Baek, Y. Choi, K.H. Park, J.W. Lee, Effects of structurally stabilized EGF and bFGF on wound healing in type I and type II diabetic mice, *Acta Biomaterialia* 66 (2018) 325-334.
[139] T.H. Nguyen, S.-H. Kim, C.G. Decker, D.Y. Wong, J.A. Loo, H.D. Maynard, A heparin-mimicking polymer conjugate stabilizes basic fibroblast growth factor, *Nature Chemistry* 5(3) (2013) 221-227.
[140] S.H. Ha, T.H. Park, S.-E. Kim, Silkworm hemolymph as a substitute for fetal bovine serum in insect cell culture, *Biotechnology Techniques* 10(6) (1996) 401-406.
[141] S. Ha, T. Park, Efficient production of recombinant protein in *Spodoptera frugiperda*/AcNPV system utilizing silkworm hemolymph, *Biotechnology Letters* 19(11) (1997) 1087-1091.
[142] H.H. Park, Y. Sohn, J.W. Yeo, J.H. Park, H.J. Lee, J. Ryu, W.J. Rhee, T.H. Park, Dimerization of 30Kc19 protein in the presence of amphiphilic moiety and importance of Cys-57 during cell penetration, *Biotechnology Journal* 9(12) (2014) 1582-1593.
[143] 김태근, Conjugation of 30Kc19α to basic fibroblast growth factor for the enhancement of stability and its application to wound healing, 서울대학교 대학원, 2017.
[144] A.N. Plotnikov, S.R. Hubbard, J. Schlessinger, M. Mohammadi, Crystal structures of two FGF-FGFR complexes reveal the determinants of ligand-receptor specificity, *Cell* 101(4) (2000) 413-424.
[145] K. Hirose, M. Fujita, A. Marui, Y. Arai, H. Sakaguchi, Y. Huang, S. Chandra, Y. Tabata, M. Komeda, Combined treatment of sustained-release basic fibroblast growth factor and sarpogrelate enhances collateral blood flow effectively in rabbit hindlimb ischemia, *Circulation Journal* 70(9) (2006) 1190-1194.
[146] R.J. Aviles, B.H. Annex, R.J. Lederman, Testing clinical therapeutic angiogenesis using basic fibroblast growth factor (FGF-2), *British Journal of Pharmacology* 140(4) (2003) 637-646.
[147] Y.W. Hou, M.H. Chan, H.R. Hsu, B.R. Liu, C.P. Chen, H.H. Chen, H.J. Lee, Transdermal delivery of proteins mediated by non-covalently associated arginine-rich intracellular delivery peptides, *Experimental Dermatology* 16(12) (2007) 999-1006.
[148] H.S. Choi, S.L. Gibbs, J.H. Lee, S.H. Kim, Y. Ashitate, F. Liu, H. Hyun, G. Park, Y. Xie, S. Bae, Targeted zwitterionic near-infrared fluorophores for improved optical imaging, *Nature Biotechnology* 31(2) (2013) 148-153.
[149] Y.H. An, M.J. Park, J. Lee, J. Ko, S.H. Kim, D.H. Kang, N.S. Hwang, Recent advances in the transdermal delivery of protein therapeutics with a combinatorial system of chemical adjuvants and physical penetration enhancements, *Advanced Therapeutics* 3(2) (2020) 1900116.
[150] G.C. Gurtner, S. Werner, Y. Barrandon, M.T. Longaker, Wound repair and regeneration, *Nature* 453(7193) (2008) 314-321.
[151] K. Singh, W. Ejaz, K. Dutta, S. Thayumanavan, Antibody delivery for intracellular

targets: Emergent therapeutic potential, *Bioconjugate Chemistry* 30(4) (2019) 1028-1041.
[152] S.-M. Shin, J.-S. Kim, S.-W. Park, S.-Y. Jun, H.-J. Kweon, D.-K. Choi, D. Lee, Y.B. Cho, Y.-S. Kim, Direct targeting of oncogenic RAS mutants with a tumor-specific cytosol-penetrating antibody inhibits RAS mutant–driven tumor growth, *Science Advances* 6(3) (2020) eaay2174.
[153] M. Sauter, M. Strieker, C. Kleist, A. Wischnjow, V. Daniel, A. Altmann, U. Haberkorn, W. Mier, Improving antibody-based therapies by chemical engineering of antibodies with multimeric cell-penetrating peptides for elevated intracellular delivery, *Journal of Controlled Release* 322 (2020) 200-208.
[154] O. Tietz, F. Cortezon-Tamarit, R. Chalk, S. Able, K.A. Vallis, Tricyclic cell-penetrating peptides for efficient delivery of functional antibodies into cancer cells, *Nature Chemistry* 14(3) (2022) 284-293.
[155] A.F. Schneider, M. Kithil, M.C. Cardoso, M. Lehmann, C.P. Hackenberger, Cellular uptake of large biomolecules enabled by cell-surface-reactive cell-penetrating peptide additives, *Nature Chemistry* 13(6) (2021) 530-539.
[156] M.K. Schwinn, T. Machleidt, K. Zimmerman, C.T. Eggers, A.S. Dixon, R. Hurst, M.P. Hall, L.P. Encell, B.F. Binkowski, K.V. Wood, CRISPR-mediated tagging of endogenous proteins with a luminescent peptide, *ACS Chemical Biology* 13(2) (2018) 467-474.
[157] L.R. Fayura, Y.R. Boretsky, Y.V. Pynyaha, D.N. Wheatley, A.A. Sibirny, Improved method for expression and isolation of the *Mycoplasma hominis* arginine deiminase from the recombinant strain of *Escherichia coli*, *Journal of Biotechnology* 167(4) (2013) 420-426.
[158] K. Yu, C. Liu, B.-G. Kim, D.-Y. Lee, Synthetic fusion protein design and applications, *Biotechnology Advances* 33(1) (2015) 155-164.
[159] A. Kawatra, R. Dhankhar, P. Gulati, Microbial arginine deiminase: A multifaceted green catalyst in biomedical sciences, *International Journal of Biological Macromolecules* (2021).
[160] P.W. Szlosarek, J.P. Steele, L. Nolan, D. Gilligan, P. Taylor, J. Spicer, M. Lind, S. Mitra, J. Shamash, M.M. Phillips, Arginine deprivation with pegylated arginine deiminase in patients with argininosuccinate synthetase 1–deficient malignant pleural mesothelioma: A randomized clinical trial, *JAMA Oncology* 3(1) (2017) 58-66.
[161] E. Beddowes, J. Spicer, P.Y. Chan, R. Khadeir, J.G. Corbacho, D. Repana, J.P. Steele, P. Schmid, T. Szyszko, G. Cook, Phase 1 dose-escalation study of pegylated arginine deiminase, cisplatin, and pemetrexed in patients with argininosuccinate synthetase 1–deficient thoracic cancers, *Journal of Clinical Oncology* 35(16) (2017) 1778.
[162] P.E. Hall, R. Lewis, N. Syed, R. Shaffer, J. Evanson, S. Ellis, M. Williams, X. Feng, A. Johnston, J.A. Thomson, A phase I study of pegylated arginine deiminase (pegargiminase), cisplatin, and pemetrexed in argininosuccinate synthetase 1-deficient recurrent high-grade gliomaArginine deprivation therapy in recurrent high-grade gliomas, *Clinical Cancer Research* 25(9) (2019) 2708-2716.
[163] J.X. Ji, D.R. Cochrane, B. Tessier-Cloutier, S.Y. Chen, G. Ho, K.V. Pathak, I.N. Alcazar, D. Farnell, S. Leung, A. Cheng, Arginine depletion therapy with ADI-PEG20 limits tumor growth in argininosuccinate synthase–deficient ovarian cancer, including small-cell carcinoma of the ovary, hypercalcemic type, *Clinical Cancer Research* 26(16) (2020) 4402-4413.
[164] K.-Y. Chang, N.-J. Chiang, S.-Y. Wu, C.-J. Yen, S.-H. Chen, Y.-M. Yeh, C.-F. Li, X. Feng, K. Wu, A. Johnston, Phase 1b study of pegylated arginine deiminase (ADI-PEG20) plus Pembrolizumab in advanced solid cancers, *Oncoimmunology* 10(1) (2021) 1943253.
[165] S. Costa, A. Almeida, A. Castro, L. Domingues, Fusion tags for protein solubility, purification and immunogenicity in *Escherichia coli*: The novel Fh8 system, *Frontiers in Microbiology* 5 (2014) 63.

[166] S. Nallamsetty, D.S. Waugh, Solubility-enhancing proteins MBP and NusA play a passive role in the folding of their fusion partners, *Protein Expression and Purification* 45(1) (2006) 175-182.
[167] J.D. Fox, D.S. Waugh, Maltose-binding protein as a solubility enhancer, *E. coli Gene Expression Protocols*, Springer 2003, pp. 99-117.
[168] K. Thirunavukkarasu, M. Mahajan, K.W. McLarren, S. Stifani, G. Karsenty, Two domains unique to osteoblast-specific transcription factor Osf2/Cbfa1 contribute to its transactivation function and its inability to heterodimerize with Cbfβ, *Molecular and Cellular Biology* 18(7) (1998) 4197-4208.
[169] H. Oshina, S. Sotome, T. Yoshii, I. Torigoe, Y. Sugata, H. Maehara, E. Marukawa, K. Omura, K. Shinomiya, Effects of continuous dexamethasone treatment on differentiation capabilities of bone marrow-derived mesenchymal cells, *Bone* 41(4) (2007) 575-583.
[170] F. Langenbach, J. Handschel, Effects of dexamethasone, ascorbic acid and β-glycerophosphate on the osteogenic differentiation of stem cells *in vitro*, *Stem Cell Research & Therapy* 4(5) (2013) 1-7.
[171] M. Yuasa, T. Yamada, T. Taniyama, T. Masaoka, W. Xuetao, T. Yoshii, M. Horie, H. Yasuda, T. Uemura, A. Okawa, Dexamethasone enhances osteogenic differentiation of bone marrow-and muscle-derived stromal cells and augments ectopic bone formation induced by bone morphogenetic protein-2, *PLoS One* 10(2) (2015) e0116462.
[172] J.E. Phillips, C.A. Gersbach, A.M. Wojtowicz, A.J. García, Glucocorticoid-induced osteogenesis is negatively regulated by Runx2/Cbfa1 serine phosphorylation, *Journal of Cell Science* 119(3) (2006) 581-591.
[173] T. Komori, Regulation of osteoblast differentiation by Runx2, *Osteoimmunology*, Springer 2009, pp. 43-49.
[174] T. Komori, Regulation of bone development and extracellular matrix protein genes by RUNX2, *Cell and Tissue Research* 339(1) (2010) 189-195.
[175] J.-S. Lee, J.-M. Lee, G.-I. Im, Electroporation-mediated transfer of Runx2 and Osterix genes to enhance osteogenesis of adipose stem cells, *Biomaterials* 32(3) (2011) 760-768.
[176] L. Thiagarajan, H.A.-D.M. Abu-Awwad, J.E. Dixon, Osteogenic programming of human mesenchymal stem cells with highly efficient intracellular delivery of RUNX2, *Stem Cells Translational Medicine* 6(12) (2017) 2146-2159.
[177] X. Jia, H. Tian, L. Tang, L. Zheng, L. Zheng, T. Yang, B. Yu, Z. Wang, P. Lin, X. Li, High-efficiency expression of TAT-bFGF fusion protein in *Escherichia coli* and the effect on hypertrohic scar tissue, *PLoS One* 10(2) (2015) e0117448.
[178] F. Wu, S. Yang, W. Yuan, T. Jin, Challenges and strategies in developing microneedle patches for transdermal delivery of protein and peptide therapeutics, *Current Pharmaceutical Biotechnology* 13(7) (2012) 1292-1298.
[179] O. Pillai, V. Nair, A.K. Jain, N.S. Thomas, R. Panchagnula, Noninvasive transdermal delivery of peptides and proteins, *Drugs Future* 26(8) (2001) 779-791.
[180] H.A. Benson, S. Namjoshi, Proteins and peptides: Strategies for delivery to and across the skin, *Journal of Pharmaceutical Sciences* 97(9) (2008) 3591-3610.
[181] S. Chandrasekhar, L.K. Iyer, J.P. Panchal, E.M. Topp, J.B. Cannon, V.V. Ranade, Microarrays and microneedle arrays for delivery of peptides, proteins, vaccines and other applications, *Expert Opinion on Drug Delivery* 10(8) (2013) 1155-1170.
[182] B. Chaulagain, A. Jain, A. Tiwari, A. Verma, S.K. Jain, Passive delivery of protein drugs through transdermal route, *Artificial Cells, Nanomedicine, and Biotechnology* 46(sup1) (2018) 472-487.
[183] L. Zheng, Q. Hui, L. Tang, L. Zheng, Z. Jin, B. Yu, Z. Wang, P. Lin, W. Yu, H. Li, TAT-mediated acidic fibroblast growth factor delivery to the dermis improves wound healing of deep skin tissue in rat, *PLoS One* 10(8) (2015) e0135291.
[184] H.-L. Xu, P.-P. Chen, L.-F. Wang, M.-Q. Tong, Z.-h. Ou, Y.-Z. Zhao, J. Xiao, T.-L. Fu, Skin-permeable liposome improved stability and permeability of bFGF against skin of

mice with deep second degree scald to promote hair follicle neogenesis through inhibition of scar formation, *Colloids and Surfaces B*: *Biointerfaces* 172 (2018) 573-585.
[185] J. Wu, J. Zhu, C. He, Z. Xiao, J. Ye, Y. Li, A. Chen, H. Zhang, X. Li, L. Lin, Comparative study of heparin-poloxamer hydrogel modified bFGF and aFGF for *in vivo* wound healing efficiency, *ACS Applied Materials & Interfaces* 8(29) (2016) 18710-18721.
[186] S.A. Nasrollahi, C. Taghibiglou, E. Azizi, E.S. Farboud, Cell-penetrating peptides as a novel transdermal drug delivery system, *Chemical Biology & Drug Design* 80(5) (2012) 639-646.
[187] S.H. Moghadam, E. Saliaj, S.D. Wettig, C. Dong, M.V. Ivanova, J.T. Huzil, M. Foldvari, Effect of chemical permeation enhancers on stratum corneum barrier lipid organizational structure and interferon alpha permeability, *Molecular Pharmaceutics* 10(6) (2013) 2248-2260.
[188] M. Shi, Z. Jiang, Y. Xiao, Y. Song, R. Tang, L. Zhang, J. Huang, Y. Tian, S. Zhou, Stapling of short cell-penetrating peptides for enhanced tumor cell-and-tissue dual-penetration, *Chemical Communications* 58(14) (2022) 2299-2302.
[189] M.M. Ulrich, M. Verkerk, L. Reijnen, M. Vlig, A.J. Van Den Bogaerdt, E. Middelkoop, Expression profile of proteins involved in scar formation in the healing process of full-thickness excisional wounds in the porcine model, *Wound Repair and Regeneration* 15(4) (2007) 482-490.
[190] M.W. Ferguson, S. O'Kane, Scar–free healing: From embryonic mechanisms to adult therapeutic intervention, *Philosophical Transactions of the Royal Society of London. Series B*: *Biological Sciences* 359(1445) (2004) 839-850.
[191] C.O. Chantre, P.H. Campbell, H.M. Golecki, A.T. Buganza, A.K. Capulli, L.F. Deravi, S. Dauth, S.P. Sheehy, J.A. Paten, K. Gledhill, Production-scale fibronectin nanofibers promote wound closure and tissue repair in a dermal mouse model, *Biomaterials* 166 (2018) 96-108.
[192] M.G. Tonnesen, X. Feng, R.A. Clark, Angiogenesis in wound healing, *Journal of Investigative Dermatology Symposium Proceedings*, Elsevier 2000, pp. 40-46.
[193] X. Chen, J.L. Zaro, W.-C. Shen, Fusion protein linkers: Property, design and functionality, *Advanced Drug Delivery Reviews* 65(10) (2013) 1357-1369.
[194] M. Van Rosmalen, M. Krom, M. Merkx, Tuning the flexibility of glycine-serine linkers to allow rational design of multidomain proteins, *Biochemistry* 56(50) (2017) 6565-6574.
[195] Z. Shu, I. Tanaka, A. Ota, D. Fushihara, N. Abe, S. Kawaguchi, K. Nakamoto, F. Tomoike, S. Tada, Y. Ito, Disulfide-unit conjugation enables ultrafast cytosolic internalization of antisense DNA and siRNA, *Angewandte Chemie* 131(20) (2019) 6683-6687.
[196] E. Polo, M. Collado, B. Pelaz, P. Del Pino, Advances toward more efficient targeted delivery of nanoparticles *in vivo*: Understanding interactions between nanoparticles and cells, *ACS Nano* 11(3) (2017) 2397-2402.
[197] K.B. Farrell, A. Karpeisky, D.H. Thamm, S. Zinnen, Bisphosphonate conjugation for bone specific drug targeting, *Bone Reports* 9 (2018) 47-60.
[198] T. Jiang, X. Yu, E.J. Carbone, C. Nelson, H.M. Kan, K.W.-H. Lo, Poly aspartic acid peptide-linked PLGA based nanoscale particles: Potential for bone-targeting drug delivery applications, *International Journal of Pharmaceutics* 475(1-2) (2014) 547-557.
[199] Y. Wang, J. Yang, H. Liu, X. Wang, Z. Zhou, Q. Huang, D. Song, X. Cai, L. Li, K. Lin, Osteotropic peptide-mediated bone targeting for photothermal treatment of bone tumors, *Biomaterials* 114 (2017) 97-105.
[200] J. Bang, H. Park, J. Yoo, D. Lee, W.I. Choi, J.H. Lee, Y.-R. Lee, C. Kim, H. Koo, S. Kim, Selection and identification of a novel bone-targeting peptide for biomedical imaging of bone, *Scientific Reports* 10(1) (2020) 1-10.

[201] V. Juang, C.H. Chang, C.S. Wang, H.E. Wang, Y.L. Lo, pH-responsive PEG-shedding and targeting peptide-modified nanoparticles for dual-delivery of irinotecan and microRNA to enhance tumor-specific therapy, *Small* 15(49) (2019) 1903296.
[202] H. Harada, M. Hiraoka, S. Kizaka-Kondoh, Antitumor effect of TAT-oxygen-dependent degradation-caspase-3 fusion protein specifically stabilized and activated in hypoxic tumor cells, *Cancer Research* 62(7) (2002) 2013-2018.
[203] E. Kondo, H. Iioka, K. Saito, Tumor-homing peptide and its utility for advanced cancer medicine, *Cancer Science* 112(6) (2021) 2118-2125.
[204] C.P. Cerrato, K. Künnapuu, Ü. Langel, Cell-penetrating peptides with intracellular organelle targeting, *Expert Opinion on Drug Delivery* 14(2) (2017) 245-255.
[205] H. Owji, N. Nezafat, M. Negahdaripour, A. Hajiebrahimi, Y. Ghasemi, A comprehensive review of signal peptides: Structure, roles, and applications, *European Journal of Cell Biology* 97(6) (2018) 422-441.
[206] C.P. Cerrato, Ü. Langel, An update on cell-penetrating peptides with intracellular organelle targeting, *Expert Opinion on Drug Delivery* 19(2) (2022) 133-146.

국 문 초 록

30Kc19α 기반의 세포 내 카고 전달 시스템 개발 및 이의 치료적 응용

이 해 인
서울대학교 대학원
공과대학 화학생물공학부

생체막은 살아있는 세포의 생존과 다양한 기능에 필수적이다. 그러나 선택적 투과성을 갖는 장벽으로서의 특성은 치료 목적의 생체 분자를 세포 내로 효율적으로 전달하는 데 주요 장애물이 될 수 있다. 많은 생체 분자는 극성, 전하 또는 큰 크기 등의 특성으로 인해 세포 불투과성을 보인다. 세포 불투과성 생체 분자의 세포 내 전달이 가능하다면, 세포 내 표적에 대한 새로운 약물이 개발될 수 있다. 세포 투과 펩타이드(CPP)는 mRNA, DNA 및 단백질과 같은 다양한 치료 생체 분자의 세포 내 전달을 위한 '운송수단'으로서 활용되어 왔다. 30Kc19α는 누에 혈림프에서 유래한 단백질로 세포 투과 및 카고 전달 특성을 가지고 있다.

본 연구에서는 30Kc19α 단백질이 효소, 전사인자, 성장인자 등 다양한 카고 단백질의 세포 내 전달을 위한 '운송수단'으로서 활용되었다. 30Kc19α는 다른 CPP와 달리 세포 투과 능력에 용해도 향상제 및 단백질 안정제와 같은 추가 기능이 있다. 이러한 특성을 통해 30Kc19α와 카고 단백질의 융합은 카고 단백질의 용해도와 안정성을 향상시킬 수 있을 것으로 기대되었다. 융합 단백질은 대장균에서 생산되었다. 그런 다음 다양한 시험관 및 생체 내 실험을 통해 융합 단백질의 치료 효능을 평가했다.

먼저, L-아르기닌을 L-시트룰린으로 전환하는 반응을 촉매하는 미생물 유래 효소인 아르기닌 데이미나제(ADI)를 카고 단백질로 선정했다. ADI는 흑색종을 포함한 아르기닌 영양요구성 종양에 대한 항암 활성을 나타내는 것으로 보고되었다. 그러나 암세포가 ADI에 지속적으로 노출되면 세포 내부에서 아르기닌이 생합성되기 때문에 ADI 내성이 발생한다. 세포 내 생합성 된 아르기닌이 시트룰린으로 전환되기 위해서는 ADI의 세포 내 전달이 필요하다. 더욱이, 재조합 ADI 단백질은 주로 대장균에서 봉입체 형태로 발현되고 인간 혈청에서 불안정한 특성이 있다. 30Kc19α와 마이코플라스마 호미니스 유래 재조합 ADI를 융합하여 이러한 문제를 해결했다. ADI와 비교하여 융합단백질은 향상된 용해도, 안정성 및 세포 투과성을 보였다. 융합 단백질은 흑색종 세포에서 ADI 내성을 감소시키는 효과가 있음을 확인했다.

두번째로, 인간 중간엽 줄기 세포(hMSC)의 골 형성 관여에 있어 마스터 조절자인 런트 관련 전사 인자 2(RUNX2)를 카고 단백질로

선정했다. 기존의 재조합 RUNX2 는 용해도가 낮고 세포 투과성이 낮아 활용에 어려움이 있었다. 30Kc19α와 재조합 RUNX2 를 융합하여 이러한 문제를 해결했다. 재조합 RUNX2 와 30Kc19α의 융합은 RUNX2 의 가용성 발현을 향상시켰고, 단백질을 hMSC 내로 성공적으로 전달했다. 30Kc19α-RUNX2 융합 단백질의 세포 내 전달은 시험관 내에서 hMSC 의 골 형성 분화를 강화했다. 30Kc19α-RUNX2 처리는 ALP 축적을 증가시키고 칼슘 침착을 증가시켰습니다. 30Kc19α-RUNX2 를 처리한 hMSC 의 이식은 피하 이식 모델에서 골분화를, 두개골 결함 마우스 모델에서 뼈 재생을 통한 골형성을 보여주었다.

세번째로, 상처 치유를 포함하여 조직 성장 및 재생에 관여하는 성장 인자인 염기성 섬유아세포 성장 인자(bFGF)를 카고 단백질로 선정했다. 30Kc19α와 재조합 bFGF를 융합하여 bFGF의 진피 전달을 향상시켰다. 30Kc19 α -bFGF는 내피세포의 혈관신생을 촉진하여 bFGF의 생물학적 활성을 보였다. 30Kc19α 는 누드마우스의 피부를 통한 저분자 형광 물질의 진피 전달을 개선해 카고 단백질의 진피 전달에 대한 가능성을 보여주었고, bFGF의 피부 축적을 증가시키고 모낭 경로를 통해 피부로의 전달을 촉진할 수 있음을 확인했다. 마지막으로 마우스 피부 상처 모델에 적용했을 때, 30Kc19α-bFGF가 진피층에 효과적으로 침투하여 세포 증식, 조직 과립화, 혈관 신생 및 조직 리모델링을 촉진하는 것을 확인했다.

마지막으로 효율적인 이량체 형성 및 세포 침투를 위해 2개의 30Kc19α를 유연한 링커로 연결한 30Kc19α-Linker-30Kc19α를

개발했다. 이량체화를 위한 최적의 유연성 링커 선정이 진행됐다. 그리고 30Kc19α와 30Kc19α-Linker-30Kc19α간의 카고 전달 능력을 비교했다. 30Kc19α-Linker-30Kc19α는 30Kc19α보다 높은 효율로 GFP를 HeLa 세포에 전달함을 확인했다. 또한, 종양 스페로이드 모델에서 30Kc19α-Linker-30Kc19α는 더 깊은 종양 침투를 보임을 확인했다.

종합하자면, 30Kc19α 기반 세포내 화물 단백질 전달 시스템이 확립되었다. 이는 다양한 카고 단백질의 세포 내 및 경피 전달을 가능하게 했다. 또한, 30Kc19α와의 융합에 의해 카고 단백질의 용해도 및 안정성이 향상되었다. 이러한 요인들이 함께 작용하여 시험관 내 및 생체 내에서 카고 단백질의 치료 효능이 향상됐다. 따라서 이 시스템은 세포 침투의 문제에 직면한 다양한 치료 생체 분자의 세포 내 전달에 적용될 수 있을 것으로 전망된다.

주요어: 세포 투과 단백질, 치료용 생체분자, 융합단백질, 세포 내 전달, 용해도 향상제, 단백질 안정제

학번: 2019-37199